uOttawa

L'Université canadienne
Canada's university

FACULTÉ DES ÉTUDES SUPÉRIEURES ET POSTOCTORALES

uOttawa

L'Université canadienne
Canada's university

FACULTY OF GRADUATE AND POSDOCTORAL STUDIES

Annick D'Auteuil

AUTEUR DE LA THÈSE / AUTHOR OF THESIS

M.A.Sc. (Civil Engineering)

GRADE / DEGREE

Department of Civil Engineering

FACULTÉ, ÉCOLE, DÉPARTEMENT / FACULTY, SCHOOL, DEPARTMENT

Aerodynamic behaviour of rectangular prisms with sharp edges at high Reynolds number

TITRE DE LA THÈSE / TITLE OF THESIS

Guy Larose

DIRECTEUR (DIRECTRICE) DE LA THÈSE / THESIS SUPERVISOR

CO-DIRECTEUR (CO-DIRECTRICE) DE LA THÈSE / THESIS CO-SUPERVISOR

EXAMINATEURS (EXAMINATRICES) DE LA THÈSE / THESIS EXAMINERS

I. Nistor

P. Simms

Gary W. Slater

LE DOYEN DE LA FACULTÉ DES ÉTUDES SUPÉRIEURES ET POSTDOCTORALES /
DEAN OF THE FACULTY OF GRADUATE AND POSTDOCORAL STUDIES

Aerodynamic behaviour of rectangular prisms with sharp edges at high Reynolds number

Annick D'Auteuil

Thesis submitted to the
Faculty of Graduate and Postdoctoral Studies
In partial fulfillment of the requirements
For the M.A.Sc. Degree in Civil Engineering

Ottawa-Carleton Institute for Civil Engineering
Faculty of Engineering
University of Ottawa

Your file Votre référence
ISBN: 0-494-14895-0
Our file Notre référence
ISBN: 0-494-14895-0

THE UNIVERSITY OF OTTAWA

FACULTY OF GRADUATE AND POSTDOCTORAL STUDIES

CERTIFICATE OF EXAMINATION

Examining Board

Ioan Nistor

Paul Simms

Advisor

Guy L. Larose

The thesis by

Annick D'Auteuil

entitled

Aerodynamic behaviour of rectangular prisms with sharp edges at high Reynolds number

is accepted in partial fulfillment

of the requirements for the degree of

Master of Applied Science

Date **Chair of Examining Board**

22nd Dec '05

UNIVERSITY OF OTTAWA

Date: **November 2005**

Author: **Annick D'Auteuil**

Title: **Aerodynamic behaviour of rectangular prisms with sharp edges at high Reynolds number**

Department: **Civil Engineering**

Degree: **M.A.Sc.** Convocation: **June** Year: **2006**

Permission is herewith granted to University of Ottawa to circulate and to have copied for non-commercial purposes, at its discretion, the above title upon the request of individuals or institutions.

Signature of Author

À la mémoire de mon grand-père pour qui l'apprentissage de nouveaux horizons était source de joie de vivre et d'inspiration pour aller toujours plus loin.

"L'homme se découvre quand il se mesure avec l'obstacle."

Antoine de Saint-Exupéry

"Le travail a ses raisons que seul le coeur peut comprendre."

"Le but de la discussion ne doit pas être la victoire, mais l'amélioration."

J.Joubert

"La peur est le plus grand ennemi de l'homme."

Table of Contents

List of Tables

List of Figures

Nomenclature

A	Planform area (L $\times$ W) [m^2]
AS	Aspect ratio
C_D	Drag coefficient
C_L	Lift coefficient
C_M	Pitching moment coefficient
C_N	Normal force coefficient
C_P	Pressure coefficient
C_{P_c}	Surface pressure coefficient corrected for tubing response
C_{P_u}	Surface pressure coefficient uncorrected for tubing response
C_X	Axial force coefficient
D	Depth of the prism [m]
$D(\alpha)$	Characteristic frontal dimension [m]
EPS	Electronic Pressure Scanner
FFT	Fast Fourier Transform
I_u	Longitudinal turbulence intensity [%]
I_w	Vertical turbulence intensity [%]
IAR	Institute for Aerospace Research
$IFFT$	Inverse Fast Fourier Transform
L	Length of the prism [m]
L_u	Longitudinal length scales [m]
Ma	Mach number
N	Normal force [N]
NRC	National Research Council Canada
P_i	Surface pressure at tap i on the prism [kPa]
PA	Atmospheric pressure [kPa]

PI	Reference pressure in plenum [kPa]
P_M	Pitching moment [Nm]
PO	Total pressure [kPa]
PSD	Power spectral density
Re	Reynolds number (based on the depth of the prism)
St	Strouhal number
TO	Total temperature [^{0}C]
U	Mean wind velocity [m/s]
W	Width of the prism [m]
X	Axial force [N]
c	Chord (Width) [m]
f_s	Shedding frequency [Hz]
$fineness\ ratio$	Width-to-Depth
h	Height of the test section [m]
lc	Large chamfer (12.5% of D)
q	Dynamic pressure [kPa]
s	Smooth flow
sc	Small chamfer (4% of D)
se	Square edges
t	Turbulent flow
α	Angle of attack of the prism [deg]
ρ	Fluid density [kg/m^3]
μ	Fluid dynamic viscosity [Ns/m^2]
σ_u	Standard deviation of the longitudinal component of U [m/s]
σ_w	Standard deviation of the transversal component of U [m/s]

Abstract

This research is aimed at depicting Reynolds number effect on bluff-body shapes with sharp edges. Nine rectangular prisms were tested: three fineness ratios (width-to-depth) of 2:1, 3:1 and 4:1 and three edge configurations, namely square edges, small chamfer and large chamfer. Tests were done in a pressurised wind tunnel for a Reynolds number range from 0.15×10^6 to 4×10^6 based on the depth of the prism and for a Mach number range from 0.075 to 0.3. The prisms were tested at angles of attack from $-2°$ up to $10°$ in increments of $2°$. The results from this study represent, to the author's knowledge, aerodynamic data at the highest Reynolds number reached for 2D rectangular prisms, in turbulent flow and for incompressible flow regime.

Measurements of steady and unsteady wind loads were made using an external sidewall force balance and surface pressures. In addition, a wake survey was performed using a hot-wire probe. The fineness ratio, the edge treatment, the angle of attack of the prism, and the wind turbulence are shown to affect the aerodynamic characteristics of the prisms. These effects appear to be influenced by Reynolds number suggesting that there is a limit to the non-sensitivity of bluff-body shapes with sharp edges to Reynolds number.

Acknowledgements

L'écriture de cet ouvrage au sens propre du terme est sans aucun doute le fruit de mon travail mais au sens figuré, il est le produit de plusieurs personnes qui ont été, par leurs différentes contributions, des sources inestimables d'inspiration et de soutien tant au niveau moral que monétaire.

D'abord, c'est au Conseil National de Recherches Canada (CNRC) que je remets la médaille d'or des remerciements. En effet, en plus de m'avoir offert un emploi d'été hautement enrichissant à l'intérieur de leur laboratoire d'aérodynamique en 2002, le CNRC m'a permis de faire la rencontre d'un chercheur hors pair qui allait devenir un être important dans le tournant de ma carrière. Dr. Guy Larose m'a proposé un projet de recherche qui m'a d'abord accroché par la pertinence des résultats que cette étude allait apporter à la communauté scientifique et d'ingénierie d'aujourd'hui mais en plus, par le caractère fondamental et pratique à la fois du problème qui se mariaient parfaitement à ma personnalité et à ma formation reçue avec un baccalauréat en génie physique. L'Institut de recherche en aérospatial du CNRC, sous la direction de M. David Simpson et par la suite de M. Jerzy Komorowski, m'a donné l'opportunité de faire mes travaux de recherche en tant que chercheure invitée et a contribué financièrement à la réussite de ma maîtrise par l'octroi d'un supplément de bourse pour étudiants gradués. Je remercie donc l'Institut et ses dirigeants du fond du coeur.

Dr. Larose a joué un rôle clé dans la réussite de ma maîtrise. Il a été bien plus qu'un superviseur de qualité, prévoyant, disponible et à l'écoute, il est devenu un ami pour qui j'ai la plus grande estime. Il a su me guider par son expérience et me fournir tous les documents nécessaires pour développer mes connaissances et progresser dans mon étude. Je garderai toujours en tête cette pensée qu'il m'a dite un jour: *Things take time.* Pour toute

cette richesse du savoir que tu m'as léguée à ce jour, pour cette progression sur mes connaissances en aérodynamique, pour l'évolution de ma propre personne et pour l'immense confiance que tu as en moi au niveau professionnel et personnel, merci Guy.

De plus, je tiens à remercier Dr. Larose pour sa contribution hautement significative côté monétaire par l'entremise d'une bourse de recherche qui m'a été offerte au cours de mes 28 mois d'étude. Dr. Larose a obtenu ce financement par une subvention à la Découverte du Conseil de Recherches en Sciences Naturelles et en Génie du Canada (CRSNG).

J'aimerais aussi remercier Vinh Nguyen, ami et professeur privé exceptionnel, ainsi que les chercheurs experts et les techniciens du CNRC pour leur participation et travail de qualité au projet *Bluff Body* qui a permis de recueillir des données précieuses jamais mesurées auparavant dans le monde et qui constituent la base de mon étude.

Au niveau institutionnel, j'aimerais offrir toute ma gratitude à l'université d'Ottawa et à l'Institut Ottawa-Carleton en génie civil pour m'avoir permis de compléter mes cours et développer mes connaissances scientifiques auprès d'excellents professeurs. Un merci spécial à Prof. Tanaka pour m'avoir d'abord admise au département de génie civil mais aussi pour son enseignement et sa gentillesse exceptionnelle. Puis, merci à l'équipe du département de génie civil, Claire, Yolande et Alain sans qui mes visites occasionnelles remplies de bonne humeur et de petites histoires n'auraient pas été les mêmes.

Je profite de cette occasion pour remercier également une personne qui a contribué au développement de ma passion pour l'aérodynamique par la qualité de son enseignement, son approche méthodique, organisée et sa personnalité agréable et sympathique, Guy Dumas, de l'Université Laval, merci pour tout.

Merci à Guy et Rick pour leur aide exceptionnelle dans la correction de cette thèse au niveau technique et linguistique et merci à Mario pour tout le temps qu'il a réussi à me faire sauver au moment où j'en avais le plus besoin.

Finalement, j'aimerais souligner la présence des gens qui partagent ma vie, Thierry, papa, maman, famille et amis qui ont un regard différent sur la personne que je suis n'étant pas impliqués dans le monde scientifique mais qui croient délibéremment en mes capacités, mon talent et en ma passion pour mon travail ce qui me donne l'élan pour aller toujours plus loin.

Introduction

In all major cities in the world, buildings and bridges are part of the landscape. The most common shape of buildings, bridge decks, bridge pylons, and bridge towers are bluff-body prisms with sharp edges (Figure 1). The large dimensions of these structures combined with a typical wind velocity of 15 to 30 m/s lead to a Reynolds number, Re, regime greater than 10^6.

Figure 1: Typical bridge tower (left) and downtown city buildings (right).

Prior to their construction, wind-tunnel tests are generally done on a model of the structure in order to evaluate its resistance to wind loads. Structures should resist to a maximum wind velocity according to the civil engineering code. Wind-tunnel tests assess, depending on the structure geometry and engineers requirements, the steady and unsteady aerodynamic behaviour such as galloping, buffeting and vortex-induced vibrations. For such

dynamic problems, different approaches can be used, such as the addition of a tuned mass damper, to reduce or eliminate the amplitude of motion or, in another way, the design of the structure could be slightly modified.

Wind-tunnel tests usually have to respect a number of non-dimensional parameters. One of them is the Reynolds number, Re, that involves first, the characteristics of the fluid such as viscosity, μ, and density, ρ, then the mean wind velocity, U and finally, a characteristic dimension of the structure, D [1]:

$$Re = \frac{\rho U D}{\mu} \tag{0.0.1}$$

The Reynolds number parameter represents the ratio of the inertia forces over the viscous forces of the fluid acting on the model. For a minimum Re around $10^3 - 10^4$, the viscosity becomes less important compare to the inertia forces.

The viscosity of the fluid has an important effect in the boundary layer that develops on the model [1]. Then, for flow attached to a body, the viscosity term will have an impact on the aerodynamic force coefficients while for separated flow, the boundary layer and the viscosity of the fluid will not be a major factor for aerodynamic force coefficients.

Since model size is usually smaller than the prototype for bridges and buildings, the wind-tunnel velocity has to be higher than the ambient wind speed in real life, or tests can be done in a pressurised wind tunnel to vary the density of the air, or test can be done in another fluid that has a density greater than air. These solutions will allow a similitude of Reynolds number for the model, m, and the prototype, p:

$$Re_p = Re_m \tag{0.0.2}$$

However, a general assumption proposed by Prandtl and Tietjens in 1934 [2] stipulates that for bluff-body shapes with sharp edges for which the separation point is well defined on the body and for which the pressure drag dominates over the friction drag, there are no Reynolds number effects on the aerodynamic force coefficients. This affirmation means that even if *Re* similitude is not satisfied for bluff-body shapes with sharp edges, the aerodynamic force coefficients will likely be the same at low *Re* ($10^3 - 10^4$) and at high *Re* ($> 10^6$).

Given that tests at low *Re* reduces the cost of wind-tunnel operations by having low wind speed and smaller test section and also, given the Prandtl and Tietjens assumption, many tests were and are still done in wind tunnel at low *Re* ($10^3 - 10^4$) even if the prototype structure will be in a *Re* regime larger than 10^6.

The impossibility of doing tests at high *Re* is not a reason to explain the popularity of low *Re* tests since there exist wind tunnels in the world, like the 1.5 m x 1.5 m Trisonic Blowdown Wind Tunnel used at the National Research Council Canada (NRC) to do this research, that provides the opportunity to perform tests at high *Re* while keeping the Mach number, *Ma*, in the incompressible region, meaning lower than *Ma* of 0.3.

The issue is that there could be a limit to *Re* non-sensitivity of bluff-body shapes with sharp edges that will affect the similitude of forces obtain at low *Re* ($10^3 - 10^4$) compared to the ones that the structure will face in real life ($> 10^6$).

In fact, recent experiments from [3]:

- Large low-speed wind tunnel;
- pressurised wind tunnel;
- full-scale measurements;

and a compendium of data from:

- Simiu and Scanlan [4]

tend to show that a limit to *Re* non-sensitivity is more than likely a reality. In the NRC 9m x 9m Wind Tunnel, study for the Stonecutters Bridge (Figures 2 and 3) was carried out for a large sectional model that used dimensions closer to the one in real life and with a wind-tunnel velocity that can reach 55 m/s [3].

On the other hand, the 1.5m x 1.5m Trisonic Blowdown Wind Tunnel, with an integrated test section of 0.381 m wide by 1.524 m high [5], was used to perform sectional model testing on a long span bridge deck. All these tests on bluff-body prisms with sharp edges have shown results that differ from those obtain for the same geometry at low *Re* ($10^3 - 10^4$).

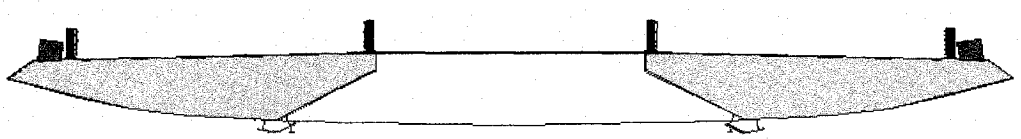

Figure 2: Deck cross-section for the Stonecutters Bridge in Hong Kong.

Also, full-scale measurements were done on the Storebaelt Bridge in Denmark during and after construction phase. The results have shown a difference for the approach bridge deck sections compared to the results obtained at low *Re* from wind-tunnel tests while

Figure 3: Photomontage of the Stonecutters Bridge.

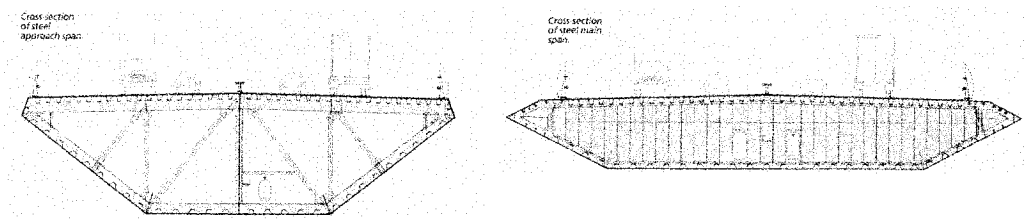

Figure 4: Deck cross-sections for the Storebælt East Bridge in Denmark, Approach Bridge (left), Suspension Bridge (right).

the main cable supported bridge deck gave comparable results in full and model scales (Figure 4). In this case, two bluff bodies with sharp edges having different width-to-depth (fineness) ratio did not seem to react the same way with the variation of Re.

Finally, Simiu and Scanlan [4] present a graph (Figure 5) that regroups data from different sources regarding drag coefficient, C_D, versus the fineness ratio of rectangular prisms with square edges. The value of C_D should be unique for a given fineness ratio if Re or other test parameters do not affect these kinds of shapes for a given wind turbulence. But, Figure 5 shows a zone where C_D is not well defined for a fineness ratio between 2 and 4.

Thus from these references, suspicion becomes more important regarding the validity of the assumption made in 1934 by Prandtl and Tietjens. The limit of the Re non-sensitivity for bluff-body shapes with sharp edges should be investigated to define it more accurately

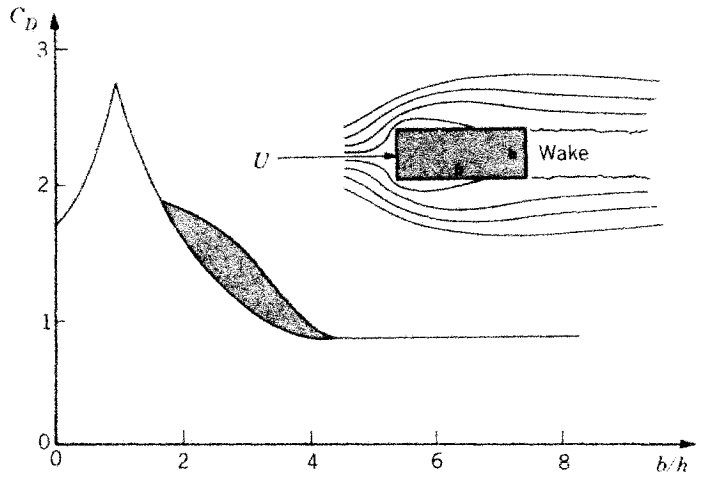

Figure 5: Drag coefficient versus fineness ratio b/h of rectangular prisms with square edges (after Simiu and Scanlan).

based on prism characteristics such as fineness ratios and edge configurations.

It has been established that a square prisms with fineness ratio of 1:1 are not affected by the variation of *Re* and do not have any reattachment for all angles of attack. However, at the opposite end of the spectrum, bluff bodies with round edges such as circular cylinders have shown a large variation of aerodynamic coefficients with *Re*. Thus, for prisms in between these two cases such as rectangular prisms with fineness of 2, 3 and 4 and for different sharp edge configurations, there could be a *Re* effect on the aerodynamic coefficients related to a possible reattachment as a function of *Re* (Figure 6).

This is the primary interest of the present research that focus on finding a limit to the *Re* non-sensitivity for bluff bodies with sharp edges by performing wind-tunnel tests on rectangular prisms. To complete this study, four different parameters were modified over a *Re* range from 0.15×10^6 to 4×10^6 based on depth, D, of the prism and Mach number

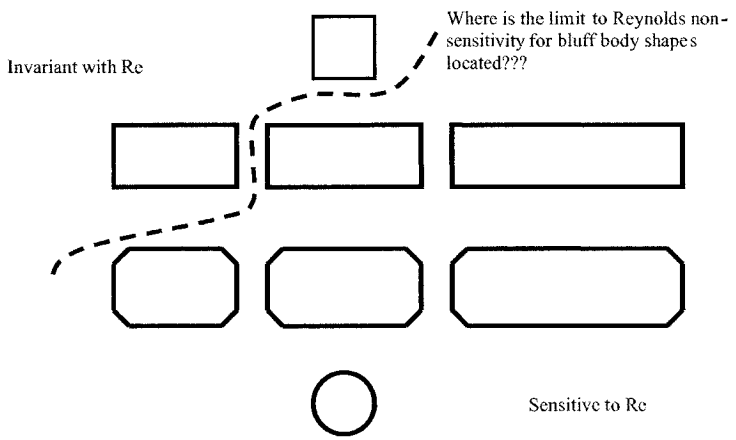

Figure 6: Bluff body cross-sections for different fineness ratios and edge configurations.

range from 0.075 to 0.3.

The first parameter was the width-to-depth ratio (fineness) of 2, 3 and 4 and the second parameter was the edge configuration with square edges, small chamfer (4% of D) and large chamfer (12.5% of D). These two parameters, combined together, gives nine bluff-body prisms that were tested during this research under two different flow conditions: smooth and turbulent that represents the third parameter. Finally, each body configuration for a given flow condition was tested at angles of attack from $-2°$ up to $10°$ in increments of $2°$ representing the fourth parameter of this study [6].

External force balances, surface pressures, and hot-wire wake probe were used to characterise the aerodynamics of the prisms such as its drag, C_D, and lift, C_L, aerodynamic pitching moment, C_M, steady and unsteady surface pressures, C_P, and vortex shedding frequency, f_s.

This thesis is composed first of a review of what has been published on the topic of aerodynamics of prisms at high and low Reynolds number. Then, the experimental conditions for the test are covered in Chapter 2 followed by the presentation of the results of this research in Chapter 3 for external force balance measurements, Chapter 4 for surface pressure measurements, and Chapter 5 for wake measurements. The results are analysed and interpreted in the Chapter 6. Appendix A presents a comparison of methods used to measure the frequency response of pneumatic tubing used for the unsteady surface pressure measurements and finally, Appendix B presents results on the validity of the two-dimensionality flow condition.

Chapter 1

Literature Review

1.1 Definition of a bluff body

A bluff body is defined as a body for which the major contribution to the drag force is due to pressure forces arising from the separation of the boundary layer and to the formation of a large recirculating flow region aft of the body.

However, an interrogation remains in this general definition: "*How bluff is bluff?*" and to which extend the appellation "*bluff*" can be apply to rectangular prism with sharp edges?

Based on the definition mentioned above, a rectangular prism could be classified in two categories: bluff body with separated flow and bluff body with separation and reattachment [7]. The possibility of reattachment of the boundary layer on the top and/or bottom surfaces of the prism will depend on parameters such as the fineness ratio (width-to-depth), edge treatment, angle of attack, Reynolds number, turbulence and the surface roughness.

A square prism is definitely a bluff body with separated flow with no possibility of reattachment on the top and bottom surfaces of the prism but, rectangular prisms with sharp edges oriented along the flow could have a possibility of reattachment of the boundary layer

which will affect the flow on the top and bottom surfaces of the prism as well as the flow in the wake and ultimately, the aerodynamics of the body [8].

1.2 Flow mechanism around rectangular prisms with sharp edges

One of the main characteristics of the flow around a rectangular prism with sharp edges is the separated shear layer that is generated at the leading edge corners (Figure 1.1). In fact, the boundary layer that develops on the leading edge of a rectangular prism is forced to separate at the corners. The boundary layers that separate from the top and the bottom of the body are separated by a region of the order of the thickness of the body. The boundary layers tend to roll up in this region producing large vortices which separate from the body and move downstream. These vortices are called von Kármán vortices when they are shedding in a rythmic alternate pattern.

The boundary layer from the top or the bottom surface of the body is developing in the wake in a vortex form and will start to have an effect on the boundary layer that comes from the opposite surface entraining fluid into a new vortex. Thus, vortices are shed from the top and the bottom of the body alternatively. The frequency to which vortices are shed in the wake of the prism is called the shedding frequency [9].

Thus, the separated shear layer generated at the leading edges plays an important role in the production of the aerodynamic forces. The behaviour of the shear layer separated from the windward corner and vortices shed into the wake are dependant on the fineness

ratio (width-to-depth) of the prism [7].

On the other hand, the more elongated rectangular prisms can have a separation at the leading corners that is followed downstream by flow reattachment and finally a flow separation at the trailing edge (Figure 1.1). Thus, in this case it is not only the flow at the leading edge that affects the wake but also the flow that develops on the top and bottom surfaces of the prism plays a role in the wake formation [10].

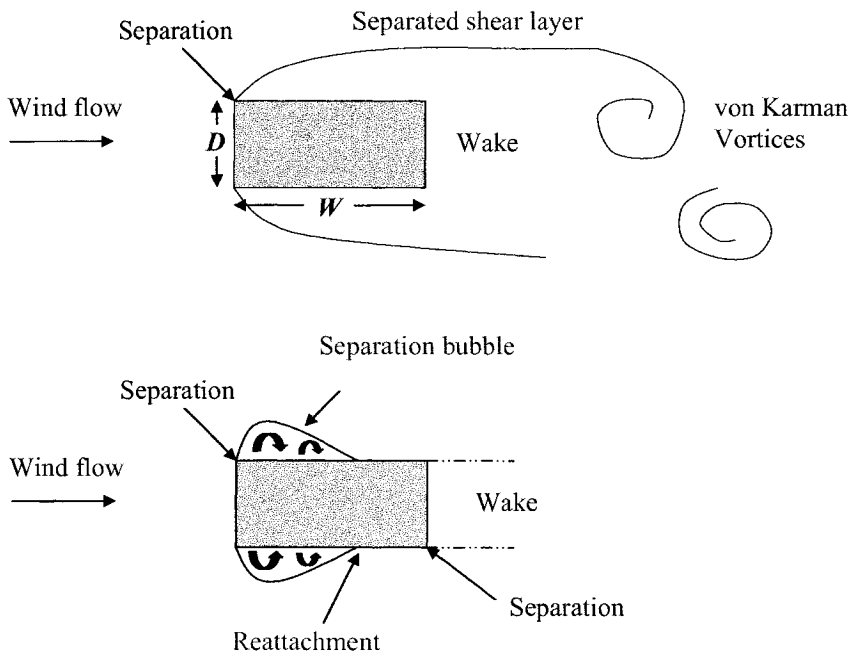

Figure 1.1: Flow separation and wake regions of rectangular prisms for bluff bodies with separated and reattached flow.

The boundary layer characteristics is divided in two categories: laminar and turbulent [9]. A laminar boundary layer will be thinner than a turbulent boundary layer but, will

be less robust and will be more susceptible to separate from the body surface if a positive pressure gradient is acting along the surface. The transition from laminar to turbulent boundary layer can occur when the boundary layer is attached to the body surface or when the boundary layer is separated from the surface. For the latter condition, the increase in energy by mixing the particles of fluid more efficiently in a turbulent environment may give the opportunity to the boundary layer to reattach.

The separated flow region between the leading corners and the reattachment point is called a separation bubble (Figure 1.1). The reattachment will depend on the body shape and on the fineness ratio (width-to-depth). The length and the intensity of the separation bubble could be influenced by the state of the boundary layer before its separation at the leading corners and thus could have an effect on the aerodynamics of rectangular prisms with reattached flow.

Finally, the condition of the oncoming flow will affect the development of the boundary layer on the body surface. Turbulent flow is known to add entrainment and help to curve the separated shear layer towards the body, increasing its tendency to reattach [10].

1.3 Turbulence effect on rectangular prisms with sharp edges

Turbulence in the flow will have an effect on the aerodynamic force coefficients for a rectangular prism. Laneville, Gartshore and Parkinson [11] have shown that the intensity of the turbulence, I_u, will reduce the potential for aerodynamic instability such as galloping

of a rectangular prism by changing the slope of the lift coefficient C_L with the angle of attack α, from a negative to a positive value at an angle of 0°. For tests done at a *Re* of 3×10^4, the intensity of turbulence required to reach a positive slope of the lift at 0° for a rectangular prism with fineness ratio of 2 and square edges was found to lie between 9% and 12%. Since turbulence increases the stability of a body, increasing the level of intensity of turbulence gives the opportunity to reduces the angle of attack of a rectangular prism at which reattachment occurs [11].

The drag coefficient is also affected by the intensity of the turbulence in the flow. For a rectangular prism with fineness between 1 and 3 and with square edges, the turbulence was found to decrease the drag force coefficient at 0° [12]. For a drag coefficient that decreases, it means that a reattachment or near-reattachment took place, leading to a narrower wake and thus a base pressure recovery and to a smaller drag [13]. Turbulence could be considered as a parameter that helps the flow to reattach for rectangular prisms with sharp edges.

Another parameter that characterises the flow turbulence is the length scales of the vortices, L_u^x within a turbulent flow. From experience done by Laneville, Gartshore and Parkinson [11] at a *Re* of 3×10^4, small length scales with high frequencies have shown to cause an earlier reattachment, by increasing the rate of entrainment of the shear layer and influencing the drag and lift coefficients and, the base pressure.

1.4 Reynolds number effect on rectangular prisms with sharp edges

While several papers exist on the aerodynamics of rectangular prisms with sharp edges at low *Re*, results at *Re* higher than 10^6 are rare. Moreover, results at high *Re* in turbulent flow for these kinds of shapes are, to the author's knowledge, nonexistent.

Delany and Sorenson have carried out tests in 1953 [14] at high *Re* for many bluff-body shapes in smooth flow. They have found in particular that for rectangular prisms with fineness ratio of 2, there is a reduction of the drag coefficient with *Re* at a value of *Re* of 1.5×10^6. In fact, for a rectangular prism with edges having a radius of curvature of 4.2% of the depth of the prism, the C_D was constant up to 1.0×10^6 and then decreases and reach a minimum at 1.5×10^6 and increases thereafter.

However, for a rectangular prism with round edges of 16.7% of the depth of the prism, the drag coefficient started to decrease at a *Re* of 0.9×10^6, reached the minimum C_D value at *Re* of 1.5×10^6 and increases thereafter but, to a higher C_D value than the one at low *Re*.

Finally, Schewe has carried out test at high *Re* in a pressurised wind tunnel in smooth flow on a trapezoidal-shaped body [15]. He analysed the aerodynamic coefficients at 0° angle of attack with a model having an aspect ratio of 6. He found that this bluff body with sharp edges had a drag reduction with *Re* up to 4.0×10^5 and had a constant value up to 10^7 thereafter. The lift coefficient was affected for the entire range of *Re* studied, $10^4 < Re < 10^7$. The Strouhal number also suffers from *Re* variation with an increase from 0.18 to 0.22 from

Re of 10^5 to 10^6. The hypothesis to explain these variations, has suggested by Schewe are [15]:

- *Re* effects are caused by changes in the topological structure of the wake.
- The location of the laminar/turbulent transition plays a key role in these structural changes.
- The flow around 2D sections can be highly 3D at high *Re*.
- There are 2D bodies that behaves as bluff or streamline bodies, depending on the *Re* range.
- Slender bodies having sharp-edged sections may suffer pronounced *Re* effect.
- In general, *Re* effects have drastic consequences on the unsteady behaviour and the fluid forces acting on an aeroelastic system.

Schewe argued that the transition from laminar to turbulent will have an effect on the flow pattern around a bluff body. Depending if the separation occurs in the separated shear layer aft of the body or at the edge of a separation bubble or, before separation of the shear layer at the leading edge of the bluff body, the wake and the aerodynamic coefficients will be affected.

Chapter 2

Experimental conditions

2.1 Model characteristics

2.1.1 Dimensions

To investigate a wide range of bluff-body shapes with sharp edges, nine rectangular prisms were studied. A main rectangular prism with a fineness ratio of 2 was built with dimensions 381.0 mm long, 152.4 mm wide and 76.2 mm high. Spacers were added at the leading and trailing edges of the model to obtain a fineness ratio of 3 (381.0 mm x 228.6 mm x 76.2 mm) and a ratio of 4 (381.0 mm x 304.8 mm x 76.2 mm). The depth of the prism was kept constant to 76.2 mm (Figures 2.1 and 2.2).

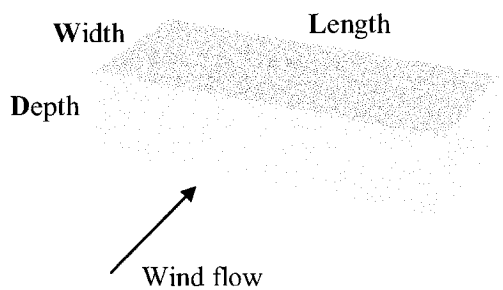

Figure 2.1: General view of the prism.

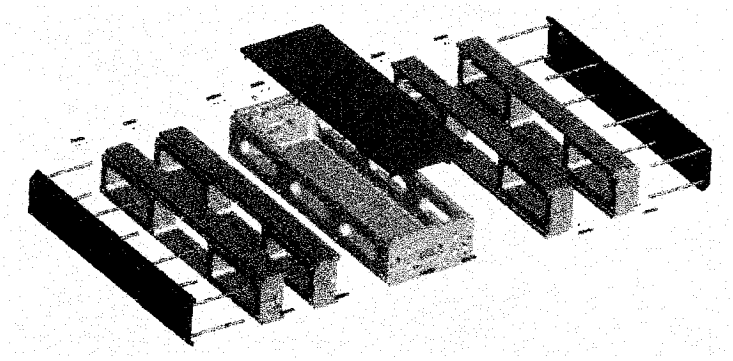

Figure 2.2: Exploded view of the model.

The aspect ratio, defined as length over the width of the prism, varied from 2.5 to 1.67 and 1.25 for the 2:1, 3:1 and 4:1 fineness ratios respectively. There were also three different thin end caps to complete the two sides: square edges, small chamfer (4% of D) and large chamfer (12.5% of D) that are shown on Figures 2.3 and 2.4. The three fineness ratios combine with the three edge configurations lead to tests on nine bluff-body prisms with sharp edges.

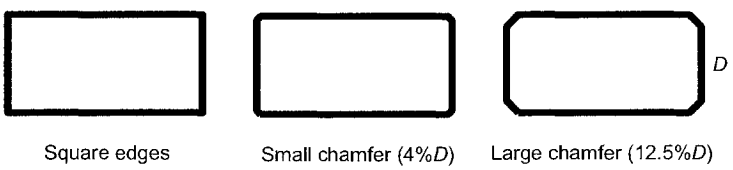

Figure 2.3: Cross-sections investigated.

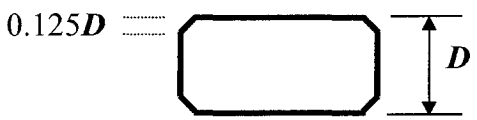

Figure 2.4: Definition of the chamfer contribution to the depth of the prism.

2.1.2 Material

The whole model was made of aluminium except for the inserts at the extremities of the model that were made of steel so that the steel pins of the external balance could fit well into the model (Figure 2.5). Also, strips of Teflon were used to prevent air flow through the very small gaps between the model and the side walls of the test section.

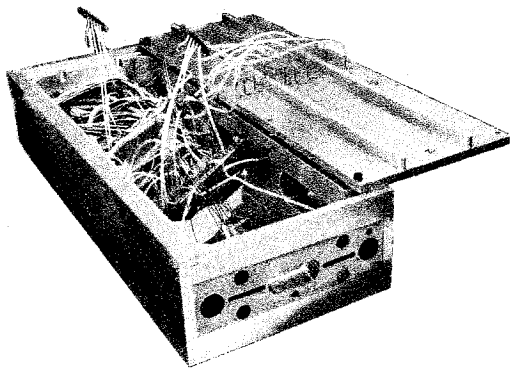

Figure 2.5: View of the 2:1 prism with top cover opened.

2.1.3 Physical properties

The weight of the prisms varied from 5.1 kg to 10.6 kg depending on fineness ratio and edge configuration. The model natural frequencies was found by manually exciting the model and performing a Fast Fourier Transform, FFT, of the lift and drag signals from the external balances over a period of time. The frequency signal obtained for the normal axis signal gave a peak at 256 Hz and 171 Hz for the axial axis drag signal for a prism with fineness ratio of 2. The lift natural frequency was observed to be close to the vortex-shedding frequency, f_s, in some cases. In fact, based on a Stouhal number, St, of 0.08 for a

2:1 prism and 0.13 for a 3:1 and 4:1 prisms [16], the expected vortex-shedding frequencies are 110 Hz, 180 Hz and 180 Hz at Ma of 0.3. Thus, a possibility of resonance between the vortex-shedding frequency and the eigen-frequency of the axial bending mode was present for all tests at Mach number of 0.3 for 3:1 and 4:1 prisms [16].

2.2 Wind-tunnel characteristics

2.2.1 Design and Capabilities

The NRC 1.5m x 1.5m Trisonic Blowdown Wind Tunnel was used to perform this research. The 2D test section is 381.0 mm wide by 1524 mm high [5]. The wind tunnel was chosen for its capability to reach high Reynolds number while keeping low Mach number by increasing the pressure in the test section using valves upstream and downstream of it. The test section has a perforated roof and floor that reduces possible wall interference and blockage effects.

The solid side walls are fitted with a suction plate system integrated within the walls and centred on the model axis with dimensions of 0.6 m x 0.46 m. It allows to keep a 2D flow configuration by suction of the boundary layer that develops on the walls of the test section (Figure 2.6). The suction was set to a value of 0.0084 that represents the normal suction velocity to mean wind velocity (U) ratio and this value was chosen based on previous tests on bluff-body shapes (circular cylinders and bridge deck) carried out in the wind tunnel.

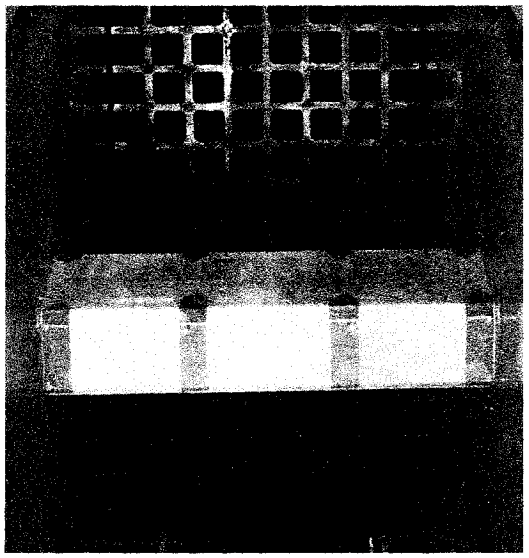

Figure 2.6: Rectangular prism in the test section with the suction plates on each side walls and the turbulence grid in background.

2.2.2 Grid turbulence

The wind tunnel has the capability to perform tests in turbulent flow. To add turbulence to the flow in the test section, a grid can be installed upstream of the model. The isotropic grid used for the test was set at a position 762 mm upstream of the model axis. It had a porosity of 64% with 9.525 mm width bars on 47.625 mm centres (Figure 2.6). The longitudinal turbulence intensity measured at the location of the model was I_u of 5% and length scales L_u^x of 35 mm [17]. Tests done earlier for a bridge deck section with the same grid have shown that the dynamic pressure in the test section should not exceed 12.4 kPa for safe operation with grid in place. Above this value, there could be damage to the grid that may affect the model.

2.3 Instrumentation

There were three different apparatuses used in this study to get quantitative data. First one was a set of external force balances, second one surface pressure measurements and finally a hot-wire wake probe.

2.3.1 External force balances

Two balances were mounted on each side walls of the test section and allowed the support of the model using two mounting pins that were introduced into machined holes at the model extremities. The balance used for the test had a range of 7 kN for across-wind force and 1.8 kN for along-wind force.

The balance system was designed to obtain the total body-axial load from the sum of outputs of two flexures located at the end of the model while the body-normal force was obtained from the summation of the four flexures arranged in pairs upstream and downstream of the centre of rotation. The pitching moment was calculated from the difference between upstream and downstream normal flexures multiplied by an appropriate distance.

The calibration performed on the balance gave an uncertainty of 0.6% for normal force, N, and 0.9% for axial force, X [17]. The external force balances were built in a way with high rigidity to provide not only a recording of the mean aerodynamic forces but also the unsteady aerodynamic forces acting on the model.

Regarding the bluff bodies tested for this study, the expected lift value was inferior to

4.4 kN and the drag up to a value of 1.8 kN while the pitching moment value expected was lower than 4.5 Nm [16]. The corresponding aerodynamic forces are converted to aerodynamic coefficients in the body-reference axis using the equations:

$$C_X = X/qA \tag{2.3.1}$$

$$C_N = N/qA \tag{2.3.2}$$

$$C_M = PM/qAc \tag{2.3.3}$$

where:

q : freestream dynamic pressure [kPa]

A : planform area [m^2]

c : chord [m]

Finally, the wind-axis aerodynamic force coefficients are computed from body-axis such as:

$$C_D = C_X cos\alpha + C_N sin\alpha \tag{2.3.4}$$

$$C_L = C_N cos\alpha - C_X sin\alpha \tag{2.3.5}$$

where:

α : angle of attack of the model.

2.3.2 Pressure measurements

There were two types of pressure measurements. The first one was tunnel-related measurements and the second one was surface pressure measurements on the model. The tunnel-related measurements included the stagnation pressure PO at the inlet of the 2D test section,

the test section reference static pressure *PI* measured at a wall pressure tap well upstream of the model, and the atmospheric pressure *PA*. The first two pressures were measured with a Digiquartz pressure transducer.

There were also static pressure measurements along the wind tunnel test section at the ceiling and floor using rail pressures that involved 32 pressure taps on each rail over a 2.5 meter length and that were connected to an electronic pressure scanner which was referenced to *PI*. When the turbulence grid was in place, the tunnel-related measurements were affected and had to be referenced to a static pressure measured downstream of the grid location. Another important tunnel-related parameter measured is the stagnation temperature *TO* in the tunnel settling chamber using a resistance thermometer.

The second category of pressure measurements is the one done at the model surface. There were 32 pressure taps for the 2:1 fineness ratio, 38 for the 3:1 and 42 for the 4:1. Pressure taps were distributed on one chord-wise strip at the centreline of the model (Figure 2.7). The positions of pressure taps were chosen to allow the possibility of detecting reattachment point, if any. Thus, there are more pressure taps towards the trailing edge that will help indicate a pressure difference from suction to positive pressure suggesting a reattachment. Also, the large chamfer configuration has pressure taps located on the chamfers of the leading edge of the prism giving the opportunity to follow the boundary layer development or the evolution of the separated shear layer.

There were also two pressure taps positioned transversely at the trailing edge of the

prism in order to verify the transverse-axis flow uniformity and the bi-dimensionality of the flow regime. Two electronic pressure scanners with a capacity of 103 kPa were used to measure the unsteady surface pressures.

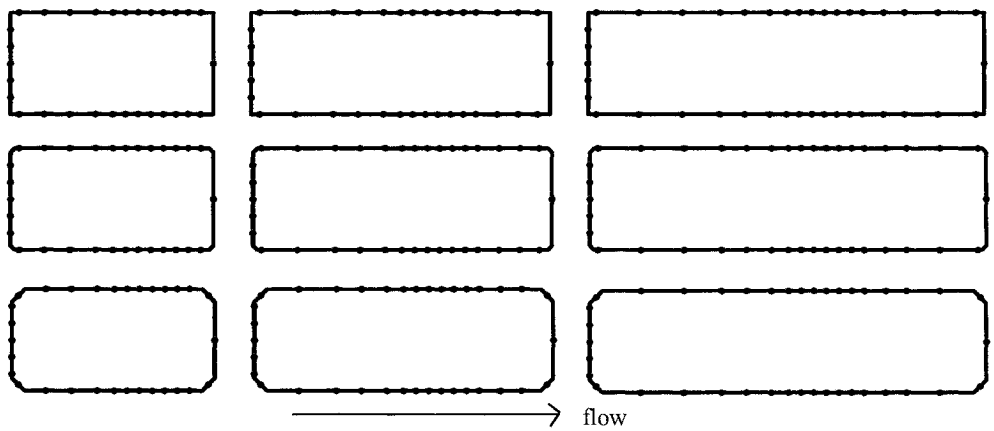

Figure 2.7: Pressure tap distribution on the nine bluff-body prisms tested.

2.3.3 Hot-wire wake probe

A hot-wire wake probe was used to measure the shedding frequency of the vortices shed from the top and bottom of the prism. The selection of the position of the hot-wire was made by moving the probe downstream of the trailing edge of the prism vertically and horizontally looking for the best signal with high fluctuations (Figure 2.8).

The position of the hot-wire in the wake was not fixed to a single position since the pitching angle of the model changed the position and shape of the wake. Table 2.1 presents the position of the hot-wire probe as function of the angle of attack of the prism and the fineness ratio. The positions are referenced to the axis at the trailing edge of the prism.

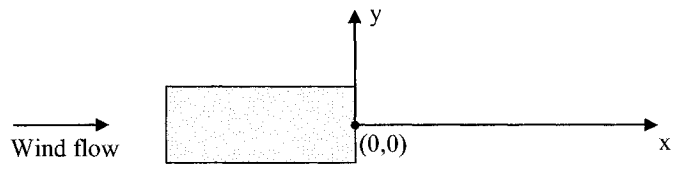

Figure 2.8: Position of the hot-wire probe in the wake of the prism referenced to the axis with origin at mid-depth of the trailing edge.

Angle of attack	2 :1		3 :1		4 :1	
	x [mm]	y [mm]	x [mm]	y [mm]	x [mm]	y [mm]
-2^0	266.7	-12.70	228.6	38.1	190.5	38.1
0^0	266.7	25.40	228.6	15.24	190.5	15.24
2^0	266.7	25.40	228.6	19.05	190.5	19.05
4^0	266.7	63.50	228.6	25.4	190.5	25.4
6^0	266.7	38.10	228.6	25.4	190.5	25.4
7^0	266.7	38.10	228.6	-	190.5	-
8^0	266.7	38.10	228.6	25.4	190.5	25.4
10^0	266.7	31.75	228.6	0	190.5	0

Table 2.1: Position of the hot-wire in the wake given for x and y axis for different angles of attack of the prism.

For the bluff-body prisms tested, the shedding frequency was expected to fall in between 30 and 200 Hz for Mach number ranging for 0.075 to 0.3 [16].

2.4 Wind spectrum

Wind-tunnel flow is characterised by turbulence intensity I and by turbulence length scales L. The flow turbulence is measured using a hot-wire. The turbulence intensity in the 1.5m x1.5m Trisonic Blowdown Wind Tunnel for an empty test section was 0.3% while the grid-generated turbulence produced a longitudinal turbulence intensity I_u of 5% and length scales L_u^x of 35 mm for a grid installed 762 mm upstream of the model axis [17]. The

measurements of the wind spectrum were performed for different Ma and Re. Figures 2.9 and 2.10 show power spectral density (PSD) results for the longitudinal u, and transverse w, velocity components of the flow. The turbulence intensity is calculated using the following equations:

$$I_u = \sigma_u / U \tag{2.4.1}$$

$$I_w = \sigma_w / U \tag{2.4.2}$$

where:

σ_u : standard deviation of the longitudinal component of wind velocity U;

σ_w : standard deviation of the transversal component of wind velocity U.

Turbulence intensity created by the grid has to be representative of the turbulence that the structure will experienced on site. For practical cases, I_u of 5% is a good approximation of the turbulence intensity in real life for the highest frequency range of the spectrum. However, the other parameter that characterise the turbulence is the length scales of the vortices. The grid produced L_u^x of 35 mm that is much smaller in comparison with the length scales of vortices in real life that can reach 200 m [17]. Usually, tests done in wind tunnel on model scale in turbulent flow will have to respect a similitude parameter that links a characteristic dimension of the body, such as depth D, to the length scales for both prototype and model:

$$\left(\frac{L_u^x}{D}\right)_p = \left(\frac{L_u^x}{D}\right)_m \tag{2.4.3}$$

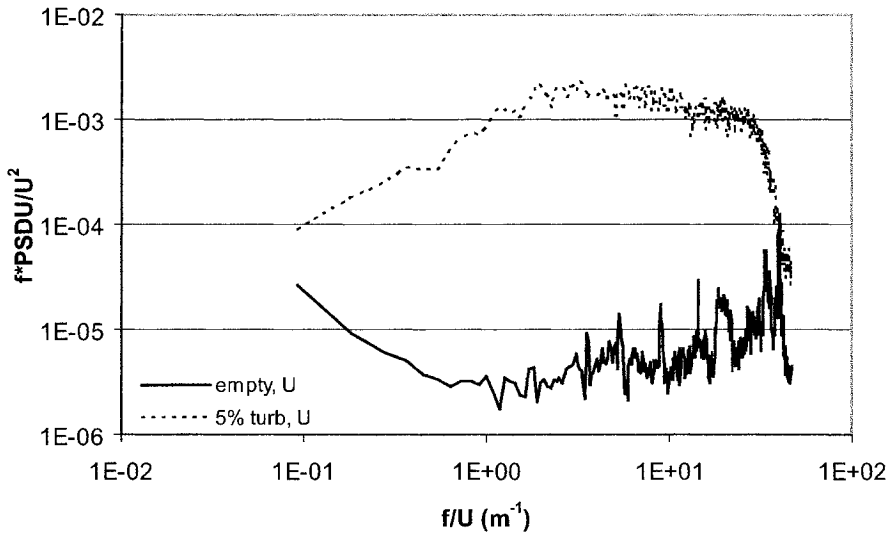

Figure 2.9: Normalised power spectral density of the longitudinal wind velocity for empty and grid-in-place test section.

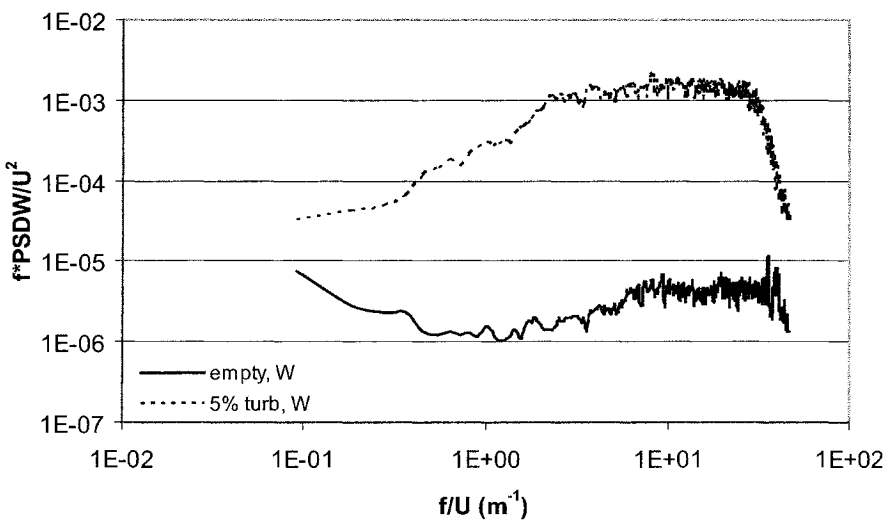

Figure 2.10: Normalised power spectral density of the transversal wind velocity for empty and grid-in-place test section.

If this is not possible to achieve, it is considered preferable to produce vortices with small length scales than large vortices since the small length scales generated by the grid have shown to affect the state of the boundary layer and thus, the separation and reattachment points that are of interest for aerodynamic research [17]. The wind spectrum has a shape as shown on Figure 2.11.

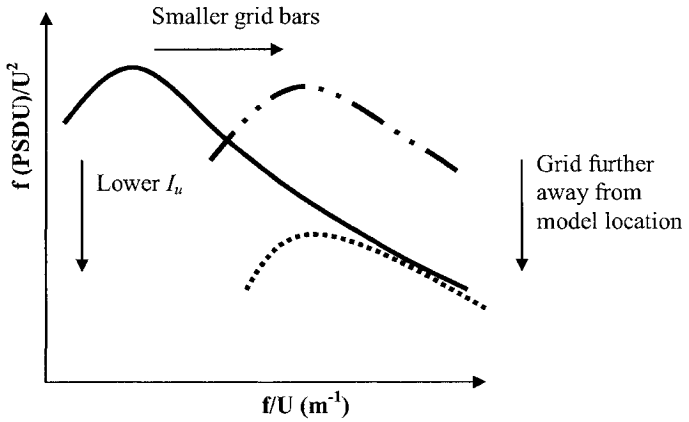

Figure 2.11: Typical wind spectrum (solid line) and other spectrums based on parameter modifications.

To model the small length scales which have high frequency vortices, a grid has to be made with small bars (dashed-dotted line in Figure 2.11) that will create the same amount of turbulence intensity but with high vortex frequencies. The grid can be placed further away from the model location (thus reducing the turbulence intensity) to allow the wind-tunnel spectrum to fit with the wind spectrum for the high frequencies range (dotted line on Figure 2.11).

2.5 Correction

2.5.1 Flow angularity

The 1.5m x 1.5m Trisonic Blowdown Wind Tunnel uses valves upstream and downstream of the test section to obtain a given pressure within the test section. This technique can introduce a flow angle at the entrance of the test section that was not eliminated in the settling chamber. In order to depict any flow angularity and to correct for this potential error, a 2D airfoil (CAST 10) was tested in the upright and inverted positions within the range of Ma of interest from 0.075 to 0.3.

Following this procedure and comparing the variations of lift coefficient with angle of attack α for the upright and inverted positions, a slight flow angularity of approximatively 0.2° was observed. This flow angularity was observed to vary also with Ma. The variation of the flow angularity correction $\Delta\alpha$ versus Ma was found to be a linear relationship as expressed by Equation 2.5.1 and nominal pitch angles were corrected during the test.

$$\Delta\alpha = -0.1562Ma + 0.236° \tag{2.5.1}$$

Ma	$\Delta\alpha$
0.075	0.224°
0.150	0.213°
0.300	0.190°

Thus physically, the model was not at 0° in the wind tunnel but the flow streamline perceived by the model were at 0°. The wall interference correction on angle of attack was not taken into account for the flow angularity correction.

2.5.2 Wall interference

The presence of walls around the model tested in the wind tunnel disturbs the flow pattern by modifying the streamline direction. There are two types of effect caused by wall interference.

First, the modification of the streamline orientation at the model location combined with the presence of the walls will affect the model causing a lift increment and an upwash effect. Accordingly, a model will have more lift at a given angle of attack than it would have in free air.

The second effect is the blockage caused by presence of the model in the closed test section. If the model frontal area is large compared to test-section area, the streamlines will have to be closer to each other in between the model and roof and, model and floor. It means that the velocity and pressure fields will be affected and will not act the same way on the model than in free air.

For this study, the upwash effect on the model was taken into account. However, the blockage effect was not considered and the aerodynamic forces were not corrected for blockage. In fact, since the model has a frontal area of 381 mm x 76.2 mm and the test section area was 381 mm x 1500 mm, it represented a blockage area ratio of 5%. On the other hand, the floor and ceiling of the test section are perforated with small holes with a porosity of 2.5%.

By comparison, it was determined experimentally that for a circular cylinder with a diameter of 150 mm, blockage area ratio of 10% and with perforated ceiling and floor at 2.5% porosity, the residual correction on aerodynamic forces was less than 1% [17]. Thus, for a blockage of 5% for the rectangular prisms in this study, the residual correction on aerodynamic forces due to blockage would be expected to be less than 1% and was therefore not considered.

Usually, wall interference correction for the 1.5m x 1.5m Trisonic Blowdown Wind Tunnel uses a technique developed by Mokry and Ohman [18] based on potential flows and rail pressures, one at the floor and one at the ceiling, both having 32 pressure taps that measure the static pressure distribution along the test section length (2.5 m). This allows a correction of the angle of attack α, and force coefficients, and was found to be very effective for streamlined bodies. For bluff bodies however, the static pressure signature measured by the rails was found to be quite different than streamlines bodies and excessively large and was considered not physically representative.

Thus, the wall interference correction method presented in Barlow, Rae and Pope [19] was applied for the present experiments. The correction was found to lie between two boundaries such as no ceiling and floor and, four solid walls since the 1.5m x 1.5m Trisonic Blowdown Wind Tunnel has a test section involving two perforated walls (roof and floor) and two solid walls (left and right). The upwash correction on the angle of attack given

in [19] for closed walls is:

$$\Delta\alpha = \frac{\pi}{96}(\frac{c}{h})^2 C_L(\frac{180}{\pi}) \tag{2.5.2}$$

where c/h is the ratio of the chord of the model to the height of the test section.

For an open section with side walls only, the equation for angle of attack correction is:

$$\Delta\alpha = -[\frac{1}{4}(\frac{c}{h}) + \frac{\pi}{24}(\frac{c}{h})^2]C_L(\frac{180}{\pi}) \tag{2.5.3}$$

Since the 1.5m x 1.5m Trisonic Blowdown Wind Tunnel test section lies in between these two situations having perforated floor and ceiling, and by inspection of the corrections based on the rail pressure measurements, it was inferred that the corrections to adopt for this study were:

$$\Delta\alpha = -0.5C_L \qquad fineness\ of\ 2 \tag{2.5.4}$$

$$\Delta\alpha = -1.2C_L \qquad fineness\ of\ 3 \tag{2.5.5}$$

$$\Delta\alpha = -1.5C_L \qquad fineness\ of\ 4 \tag{2.5.6}$$

based on:

c : chord;

h : height of the wind tunnel test section.

Thus, the correction is higher for larger angle of attack up to the stall angle where the lift coefficient reaches its highest value. Typical wall interference correction for the 2:1 prism ranged between $\Delta\alpha$ of 0.05° to 0.29°. For the 3:1 prism, the correction was between $\Delta\alpha$ of 0.24° to 0.9° and the 4:1 prism have a wall interference correction $\Delta\alpha$ of 0.3° to 1.2°.

2.5.3 Tubing frequency response

The presence of pneumatic tubing, linking the pressure tap at the surface of the model to the pressure transducer module, introduces an error by distorting the pressure signal. To remove this error, the tubing frequency response was measured by sending a known signal over a wide range of frequencies in the tube and, to a reference pressure transducer at the same time. The ratio of the two signals gave the response of the tube itself that was used to correct the time series of all pressure taps for all runs done during the tests following the correction method proposed by Irwin and Cooper [20].

The transfer function measured was for a urethane tube length of 216 mm and an inside diameter of 1.067 mm. The measurements were done for each of the 12 pressures used in the test section to perform the tests since it was observed that the magnitude of the distortion was function of the ambient pressure as shown on Figure 2.12. In order to correct the time series of all pressure taps at the surface of the model for tubing frequency response, a FFT of the time series was done to which was added its complex conjugate. This signal in the frequency domain was then divided by the tubing frequency response and the result was converted back to time domain by computing the Inverse Fast Fourier Transform, $IFFT$, of the corrected pressure spectra as per equation 2.5.7.

$$C_{P_c} = IFFT\left(\frac{FFT(C_{P_u}) + complex\ conjugate}{tubing\ frequency\ response}\right) \tag{2.5.7}$$

with:

C_{P_u} = pressure coefficient uncorrected for tubing response.

C_{P_c} = pressure coefficient corrected for tubing response.

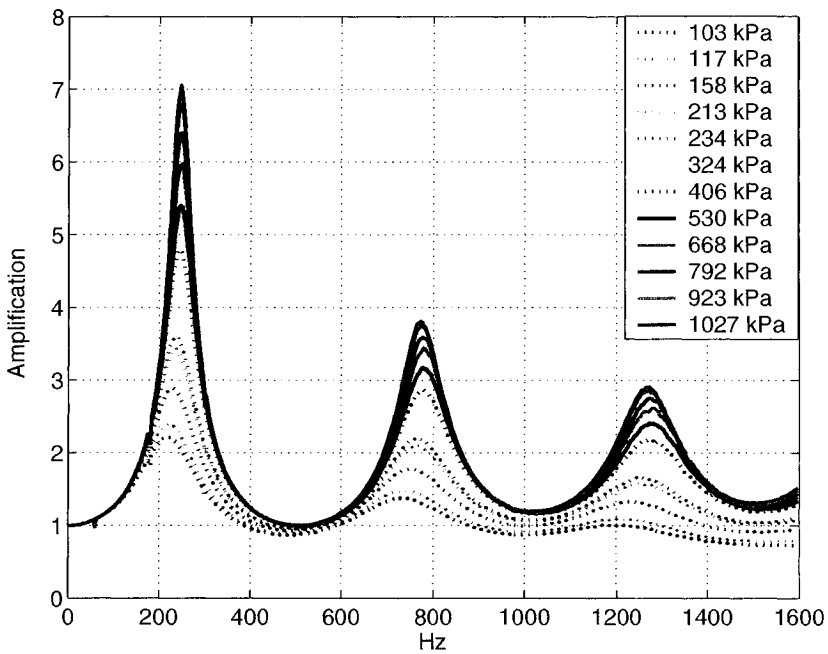

Figure 2.12: Amplitude of the tubing transfer functions for different test-section pressures.

Figures 2.12 and 2.13 show the 12 tubing frequency responses that are represented by complex transfer functions composed of a magnitude and a phase. Both the magnitude and the phase are pressure dependent. The shape of all magnitude curves are the same with three peaks around 250 Hz, 780 Hz and 1260 Hz. However, increasing the pressure in the test section multiply by a factor of seven the amplification of the tubing signal between pressure of 103 kPa and 1027 kPa and higher pressure tend to shift to the right the resonance peak frequency.

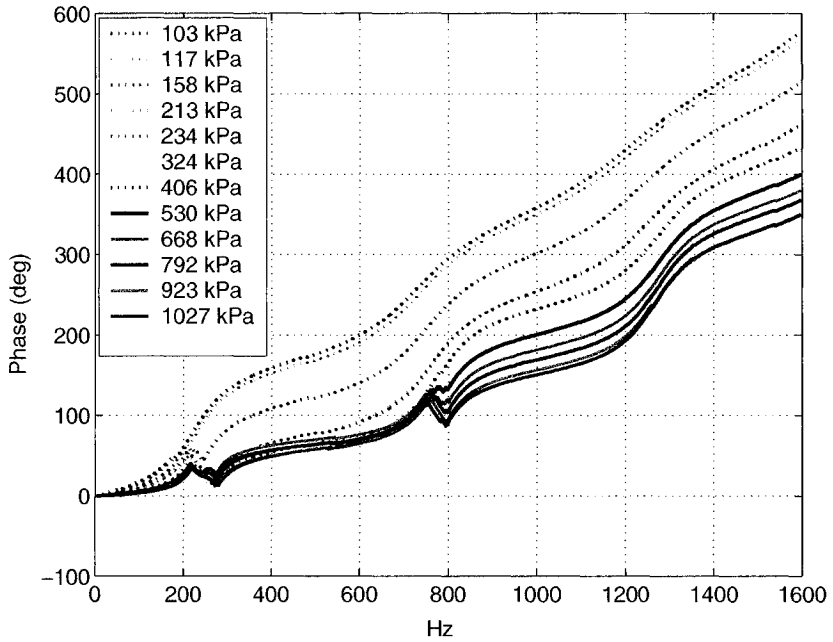

Figure 2.13: Phase of the tubing transfer functions for different test-section pressures.

2.6 Test program

In this study, the *Re* range covered was from 0.15×10^6 to 4×10^6 based on depth of the prism (constant at 76.2 mm), for *Ma* from 0.075 to 0.3. The sampling time was set at 4 seconds for each data point. This was considered long enough to reach a steady state condition in the test section. In fact, the rule of thumb suggests that 100 chord lengths are necessary to get stable aerodynamic conditions. For this study, it represents 15 m for a chord of 0.15 m. For a wind velocity of 26 m/s, the lowest velocity used in this study, it gives 100 m that is much larger than the 15 m suggested by the rule of thumb.

The data acquisition system for the external balances as well as tunnel-related measurements had a sampling frequency of 200 Hz while surface pressures and the hot-wire probe signal had a sampling frequency of 4800 Hz. The tests were carried out in smooth flow and were repeated in turbulent flow using the isotropic grid for each of the nine prisms investigated (except for the fineness ratio of 2 with small chamfer where tests in turbulent flow were not carried out).

The maximum wind velocity used to perform the tests was at Ma of 0.3 with 104 m/s and was chosen to prevent entering in the compressible flow regime not representative of general wind effects on structures. On the other hand, tests done in turbulent flow were limited to a maximum dynamic pressure of 12.4 kPa to avoid damage on the grid due to high drag force. Then, turbulent flow tests were done only for Ma of 0.075 and 0.15 and for Re up to 2.0×10^6.

For a given geometry (fineness ratio and edge configuration), tests were done in smooth and turbulent flow for seven to eight angles of attack between $-2°$ up to $10°$ in increments of $2°$ for all Ma and Re ranges mentioned above. Table 2.2 summarises the test program covered and Figure 2.14 shows the relation between the pressure in the test section and the Reynolds and Mach numbers covered for the test.

Flow	Fineness ratio	Edge configuration			Angles of wind incidence (deg)
		Square edges	Small chamfer	Large chamfer	
Smooth	2:1	14	17	17	-2, 0, 2, 4, 6, 7, 8, 10
Turbulent	2:1	11	0	14	-2, 0, 2, 4, 6, 7, 8, 10
Smooth	3:1	4	12	9	-2, 0, 2, 4, 6, 8, 10
Turbulent	3:1	7	7	8	-2, 0, 2, 4, 6, 8, 10
Smooth	4:1	9	8	10	-2, 0, 2, 4, 6, 8, 10
Turbulent	4:1	8	4	7	-2, 0, 2, 4, 6, 8, 10

Table 2.2: Summary of the model configurations tested and the number of points per configuration.

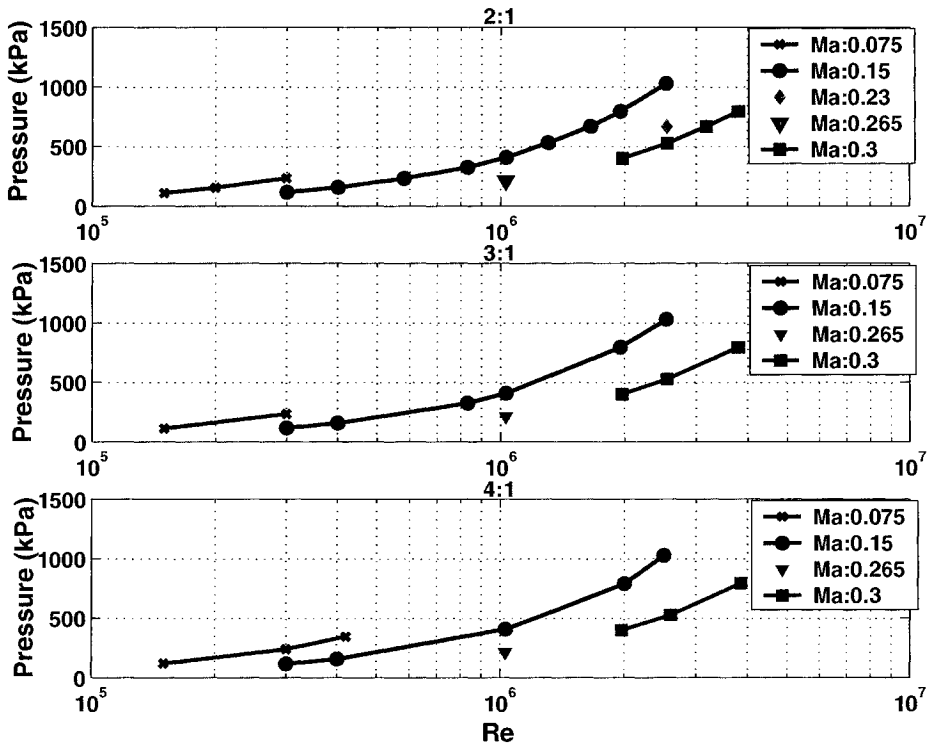

Figure 2.14: Pressure in the test section versus Reynolds number for different Mach number for prisms with fineness ratio of 2, 3 and 4.

Chapter 3

Balance measurements

This chapter presents the external balance data measured for the following conditions:

- Ma : 0.15;
- Re : 0.3×10^6 to 2.5×10^6 based on the depth of the prism;
- smooth and turbulent flow;
- prism angles of attack of $-2°$, $0°$, $2°$, $4°$, $6°$, $7°$, $8°$, $10°$;
- fineness ratio of 2, 3 and 4;
- edge configuration: square edges (se);
  small chamfer (sc);
  large chamfer (lc).

The mean aerodynamic force and moment coefficients C_L, C_D, C_M as defined in Chapter 2, were computed from coefficients C_N and C_X derived from balance force measurements, N and X, and using the planform area (length x width) for normalisation. Data were collected during 4 seconds at each test point. This period was found to be long enough to reach a stationary state since the mean force value did not change significantly (less than 1% for most of the cases) over an averaging period of 1, 2, 3 or 4 seconds.

Results are presented within this chapter in graphical form. A series of figures for each of the three coefficients show their variation with angle of wind incidence α, for nine *Re* and then a second series presents their variation with *Re* for five wind angles α. This presentation allows to depict more easily the aerodynamic coefficient sensitivity to those parameters.

3.1 Lift force coefficient C_L

3.1.1 C_L versus α

By looking first at the variation of C_L versus α on Figure 3.1, it can be observed for a 2:1 prism that most edge configurations show the potential for aerodynamic instability with a positive lift coefficient for angle of attack that are negative. In fact, square edges in smooth and turbulent flow as well as small chamfer in smooth flow show potential for galloping based on Den Hartog criteria (3.1.1) given their negative slope of C_L versus α at 0° [4]:

$$\frac{\partial C_L}{\partial \alpha} + C_D \leq 0 \tag{3.1.1}$$

The turbulence intensity is a parameter that modifies the pressure distribution around the prism which in turn can promote aerodynamic stability. As shown on Figure 3.1 turbulence intensity I_u of 5% gave enough energy to the flow to let the prism becoming aerodynamically stable (positive C_L slope) for a geometry with large chamfer.

Depending on the level of turbulence intensity, the stall angle represented by the maximum C_L value for an angle of attack range is shifted toward higher value of α. From

Figure 3.1, it can be observed that for large chamfer, the stall angle occurs at a higher angle of attack in turbulent flow than in smooth flow at Re around 2.0×10^6. Increasing Reynolds number is also a parameter affecting the 2:1 prism with large chamfer as the smooth curve is changing from negative slope of C_L versus α at $0°$ at Re of $0.3 \times 10^6 - 0.4 \times 10^6$ to a positive slope at the higher Re of 0.83×10^6.

Focusing now on the results for the 3:1 fineness ratio prisms on Figure 3.2, square edges in smooth flow show potential for aerodynamic instability such as galloping with negative slope of C_L at $0°$ while turbulent flow reversed this slope to a positive sign. The two other edge configurations with chamfers are aerodynamically stable in both flow conditions.

Finally, all the 4:1 prisms present a positive value of C_L for angles of attack above $0°$ as shown on Figure 3.3. In summary:

- Chamfers added to rectangular prism;
- fineness ratio increased from 2 to 4;
- adding turbulence intensity;

help to reduce the potential for aerodynamic instability.

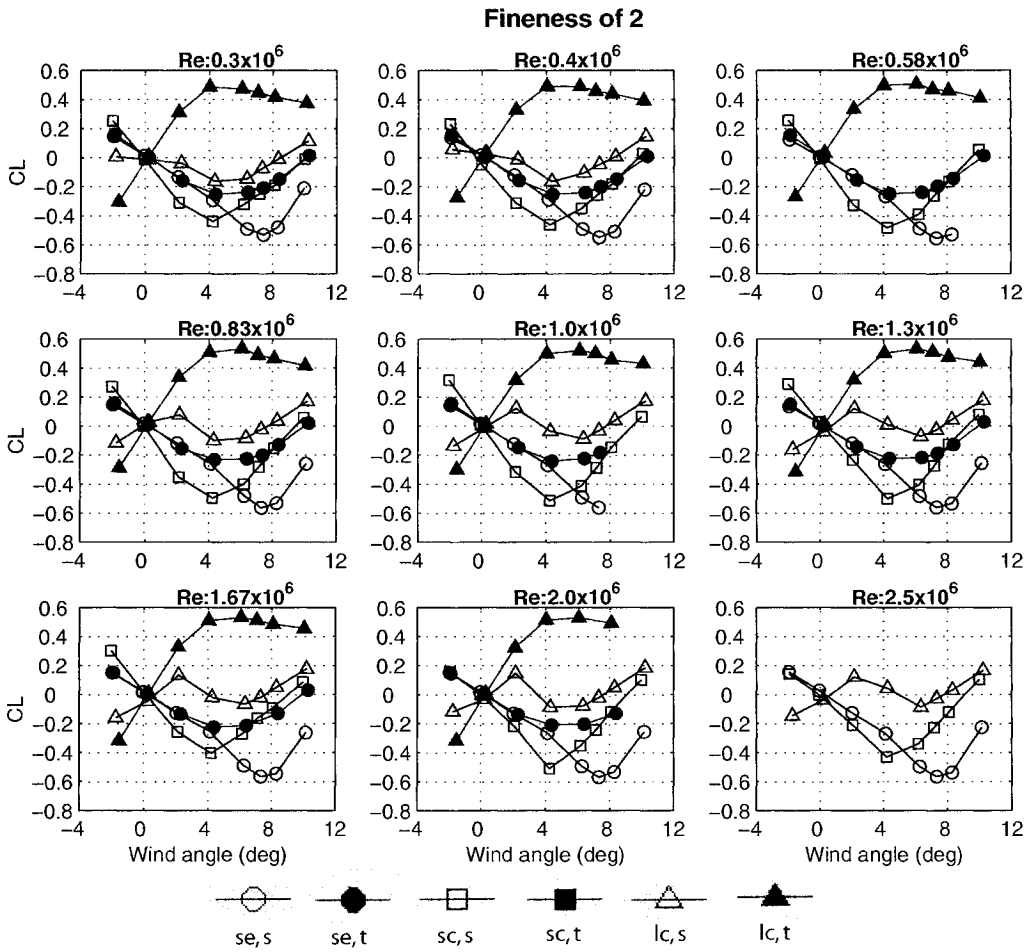

Figure 3.1: Lift coefficient versus wind angle for fineness of 2, three edge configurations, nine Reynolds numbers, in smooth (open) and turbulent (solid) flow, Mach: 0.15.

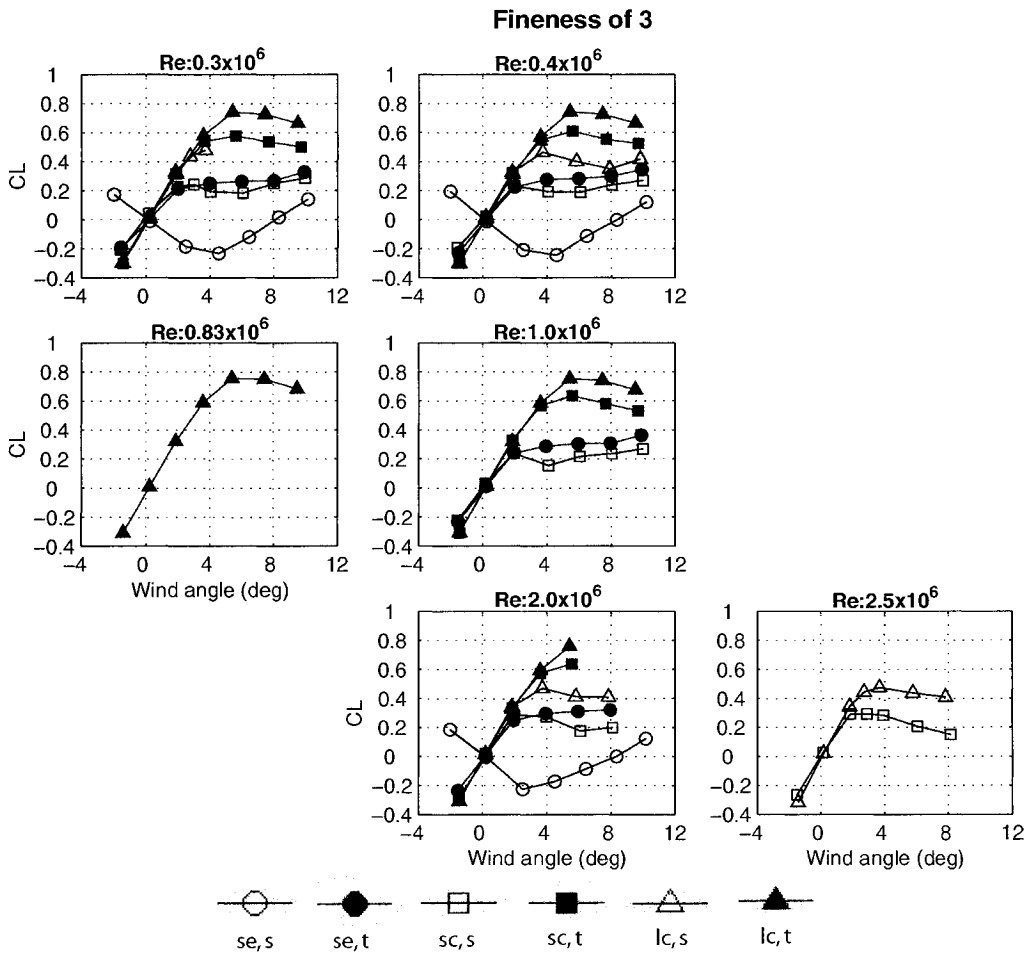

Figure 3.2: Lift coefficient versus wind angle for fineness of 3, three edge configurations, six Reynolds numbers, in smooth (open) and turbulent (solid) flow, Mach: 0.15.

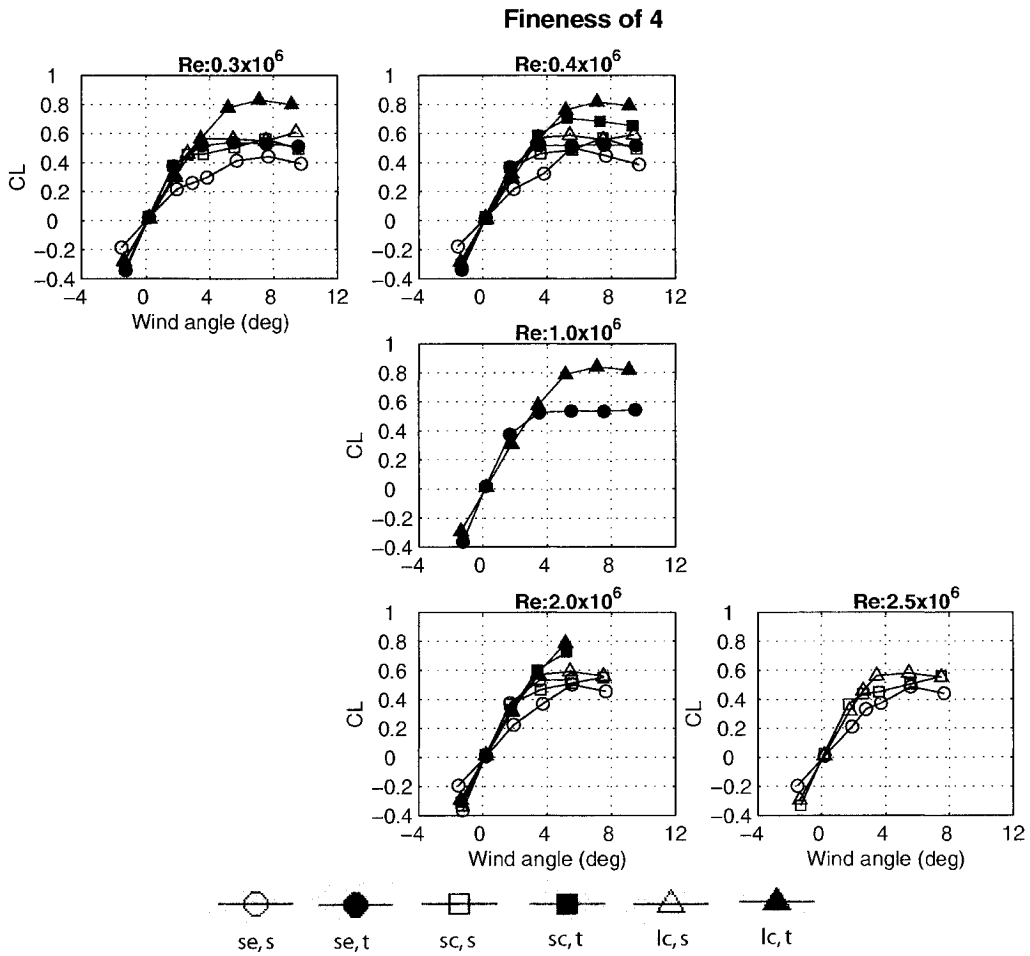

Figure 3.3: Lift coefficient versus wind angle for fineness of 4, three edge configurations, five Reynolds numbers, in smooth (open) and turbulent (solid) flow, Mach: 0.15.

3.1.2 C_L versus Re

Figures 3.4 to 3.6 present the variations of C_L with Re for the 2:1 prism. In Figure 3.4, it can be observed that square edges in smooth flow (circle) do not show a large variation of C_L with Re for the six angles of attack presented. However, looking carefully at the magnitude of the results, it represents for example at $-2°$, a variation of 20% (normalised by the smallest value) for C_L between the smallest and largest value measured within the Re investigated.

The effect of Re is however clearly present for a 2:1 prism with chamfers as Figures 3.5 and 3.6 show. The variation of C_L with Re is around 28% to 120% depending on the angle of attack for small chamfer and can reach more than 115% for large chamfer with a remarkable behaviour that shows positive and negative values for the same prism only by modifying Re. This situation occurs at almost all angles with the exception of 6°.

The turbulent results show a different reaction to the variation of Re. The effect on square-edge prism for C_L is between 10% to 20% depending on angle of attack considered while large chamfer has large C_L variation at $-2°$ and 6° with ΔC_L up to 18% and small variation for 2° and 4°. It becomes clear that Re variation is less significant in turbulent flow than in smooth flow for 2:1 prisms, regardless of the edge configuration.

Concerning the 3:1 prism (Figures 3.7 to 3.9), smooth flow results show a high level of Re sensitivity for square edges and small chamfer edge treatments. Figure 3.7 shows

a maximum difference of C_L around 44%. Small chamfer in Figure 3.8 presents large C_L variation and the maximum is observed at 4° with 86%. Less significant C_L variation was noticed for large chamfer on Figure 3.9 with a maximum variation of 10% at 6°.

Thus, a 3:1 prism is less affected by the variation of *Re* for large chamfer configuration compared with a 2:1 fineness ratio prism. In turbulent flow, only the square edges present large C_L variation above 15%.

Finally, the 4:1 prisms show clearly on Figure 3.10 a *Re* dependance for higher angles of attack for a square-edge prism. While for $-2°$, 0°, and 2°, the variation is around 5-10%, angles of attack of 4° and 6° present a C_L variation up to 25%. However, C_L variation of less than 8% was observed for small and large chamfers in smooth flow and for all edge configurations in turbulent flow.

In summary:

- C_L of prisms with fineness ratio of 2, regardless of edge configuration, are considerably affected by *Re*;
- a smaller fineness ratio prism shows C_L variation for a wider range of angle of attack compare to larger fineness ratio that are affected for higher angles of attack only;
- turbulence tends to decrease considerably the effect of *Re* on C_L.

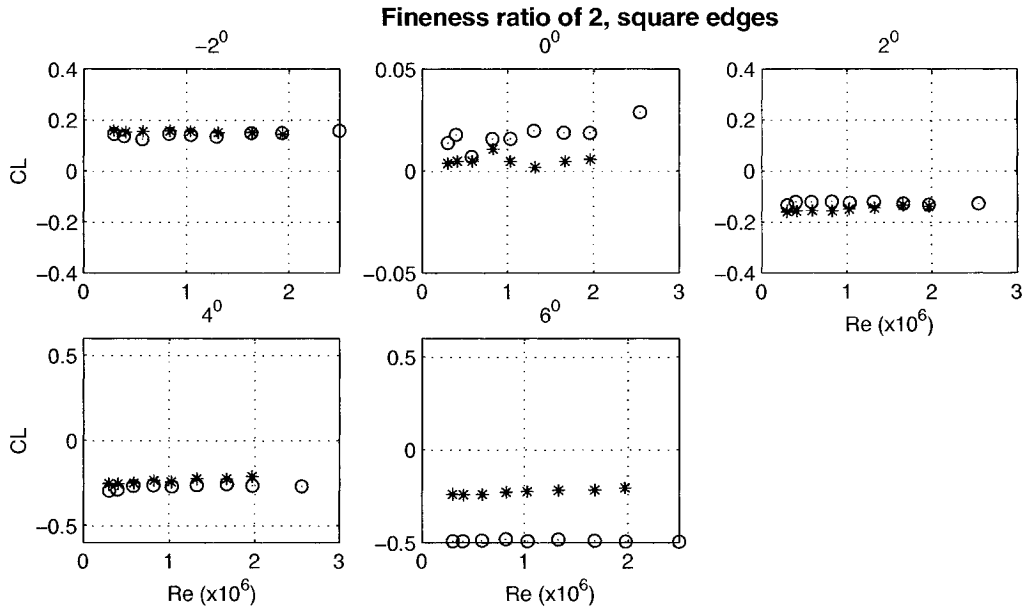

Figure 3.4: Lift coefficient versus Reynolds number for fineness of 2, square edges, five angles of attack in smooth (circle) and turbulent (star) flow, Mach: 0.15.

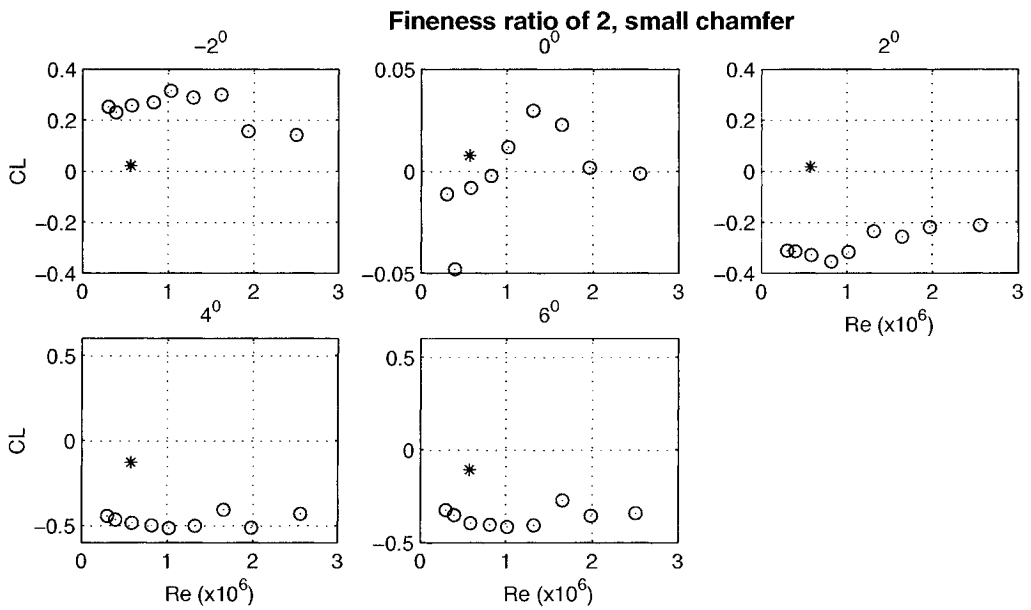

Figure 3.5: Lift coefficient versus Reynolds number for fineness of 2, small chamfer, five angles of attack in smooth (circle) and turbulent (star) flow, Mach: 0.15.

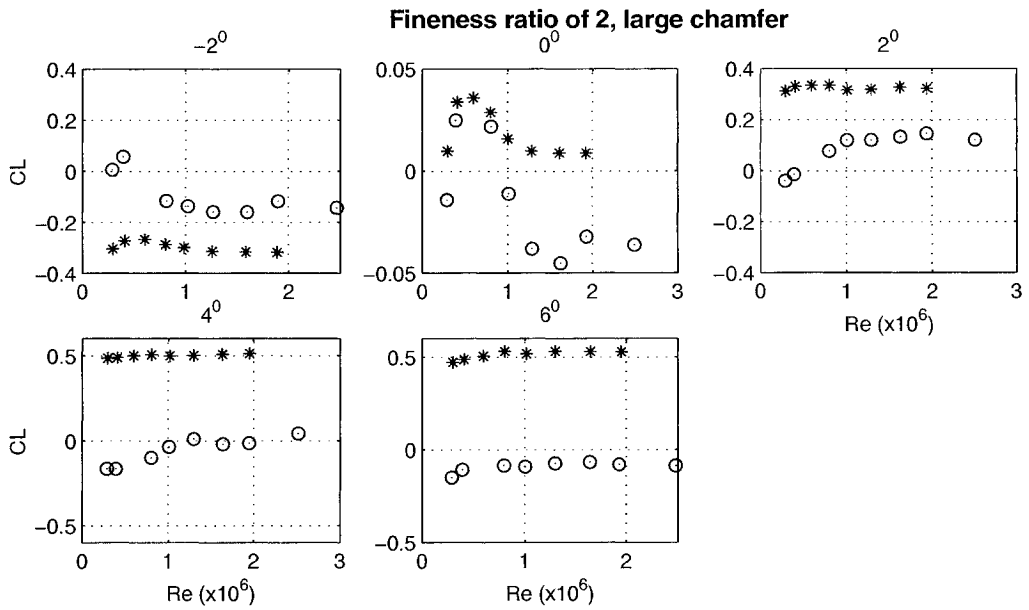

Figure 3.6: Lift coefficient versus Reynolds number for fineness of 2, large chamfer, five angles of attack in smooth (circle) and turbulent (star) flow, Mach: 0.15.

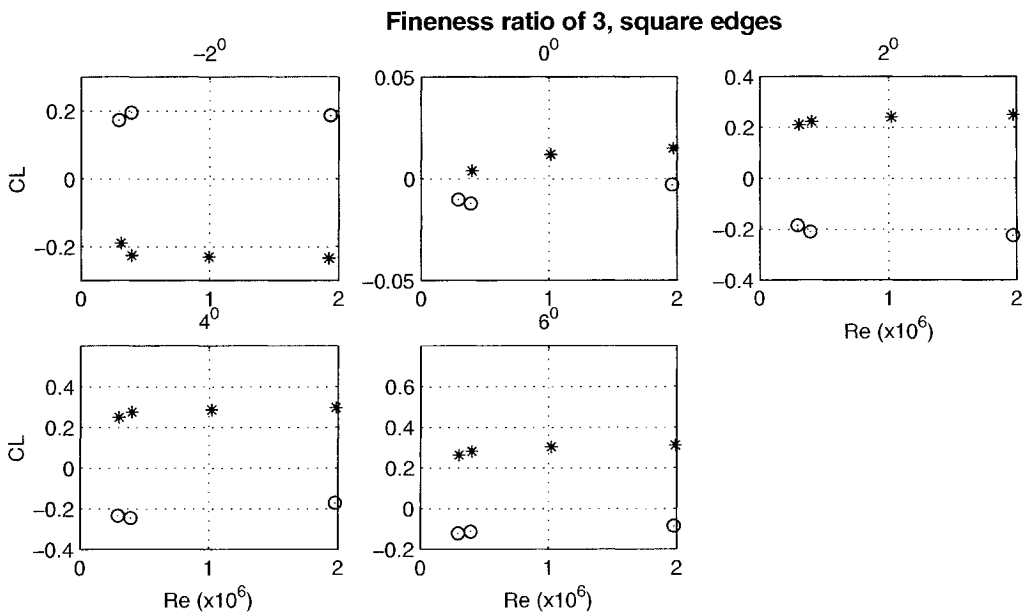

Figure 3.7: Lift coefficient versus Reynolds number for fineness of 3, square edges, five angles of attack in smooth (circle) and turbulent (star) flow, Mach: 0.15.

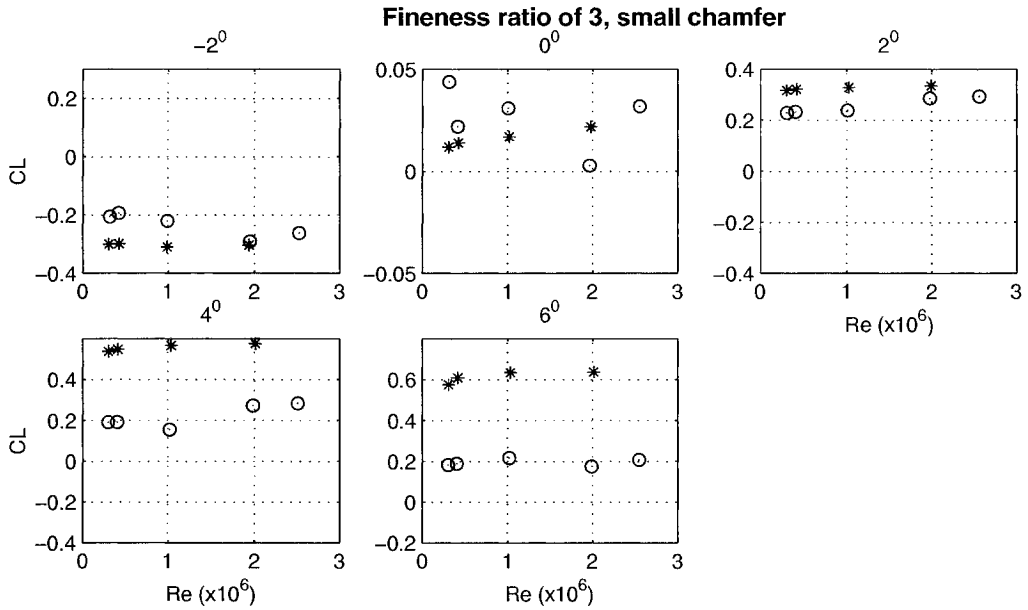

Figure 3.8: Lift coefficient versus Reynolds number for fineness of 3, small chamfer, five angles of attack in smooth (circle) and turbulent (star) flow, Mach: 0.15.

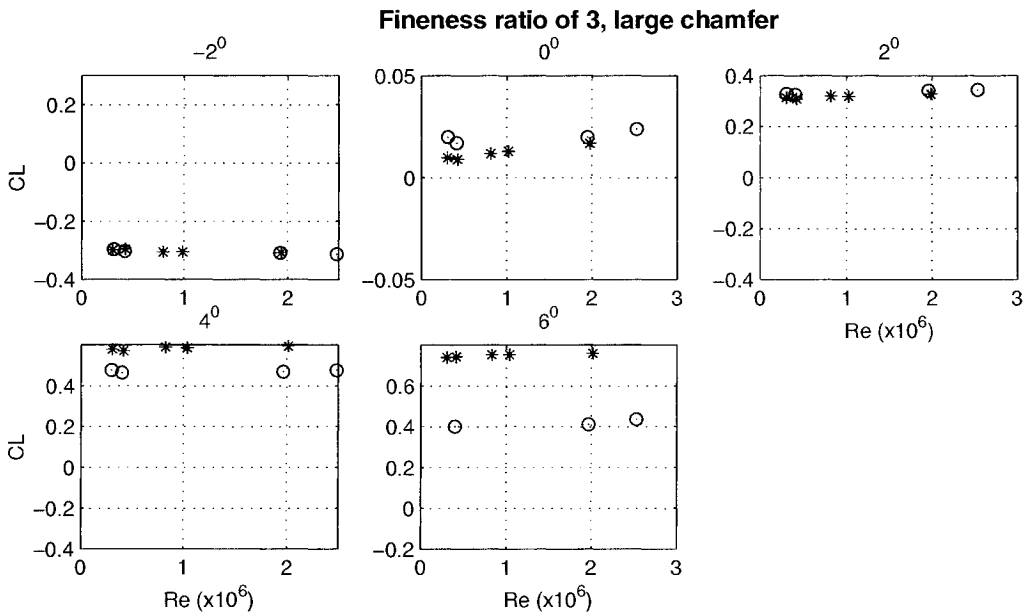

Figure 3.9: Lift coefficient versus Reynolds number for fineness of 3, large chamfer, five angles of attack in smooth (circle) and turbulent (star) flow, Mach: 0.15.

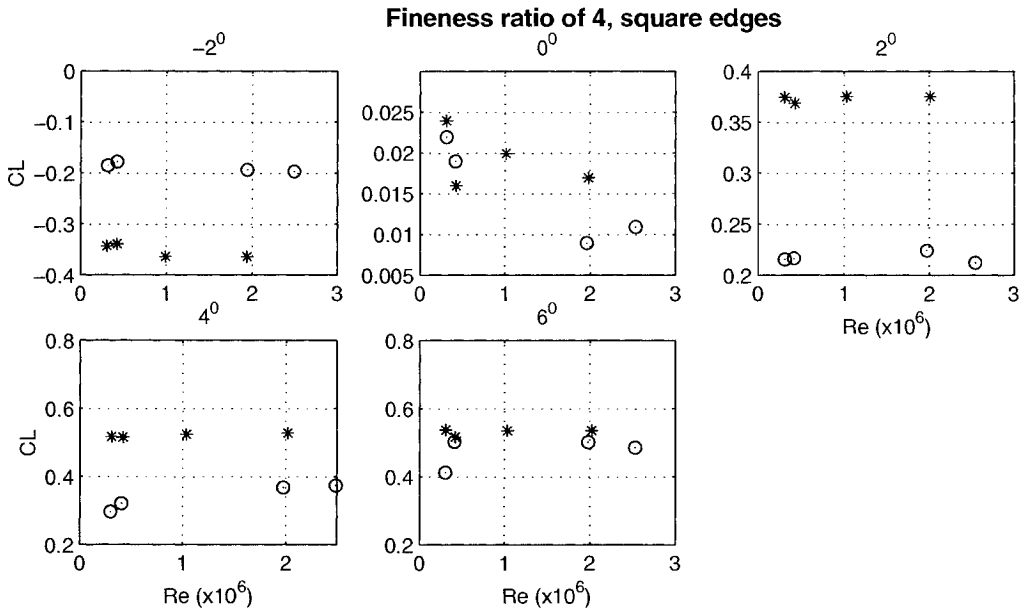

Figure 3.10: Lift coefficient versus Reynolds number for fineness of 4, square edges, five angles of attack in smooth (circle) and turbulent (star) flow, Mach: 0.15.

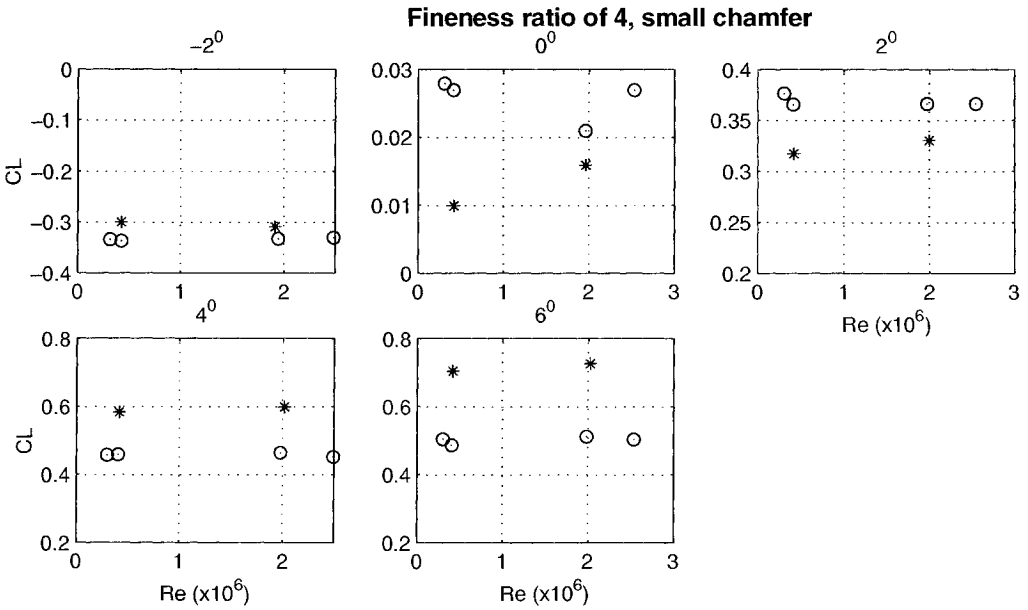

Figure 3.11: Lift coefficient versus Reynolds number for fineness of 4, small chamfer, five angles of attack in smooth (circle) and turbulent (star) flow, Mach: 0.15.

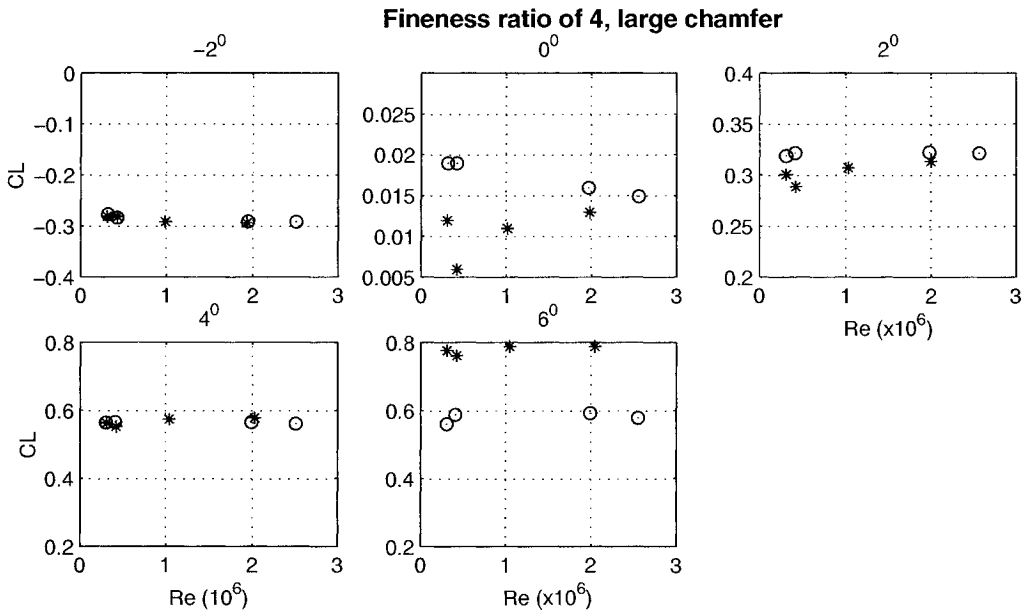

Figure 3.12: Lift coefficient versus Reynolds number for fineness of 4, large chamfer, five angles of attack in smooth (circle) and turbulent (star) flow, Mach: 0.15.

3.2 Drag force coefficient C_D

While for a square prism, C_D is known to be constant for Re up to and greater than 10^6 and for a circular cylinder, C_D is completely dependant of Re, it is expected that the rectangular prisms studied here would give results in between these two opposite cross-sectional shapes.

3.2.1 C_D versus α

The drag coefficient variations with wind angle α for a 2:1 prism have shown to be a function of the edge configuration considered. From Figure 3.13, it is observed that the square-edge prism as well as the prisms with small chamfer in smooth flow show a negative parabola at 0° while square edges in turbulent flow as well as large chamfer for both flow conditions have a positive parabola at 0°. Expecting a higher drag for prism with angle of attack higher than 0°, the square edge and small chamfer configurations in smooth flow present the opposite behaviour. However, the 3:1 and 4:1 prisms on Figures 3.14 and 3.15 are showing a positive parabola at 0°.

Higher C_D values were observed for square-edge prism while large chamfer had the lowest one. The C_D is also higher for a 2:1 prism compare to a 4:1 prism for the same edge configuration. For example, Figure 3.13 presents a C_D value of 0.68 at 0° for Re of 0.3×10^6 while a 3:1 prism (Figure 3.14) gives 0.35 and 4:1 prism gives 0.24 (Figure 3.15).

On the other hand, turbulent flow gives in general higher C_D values regardless of the

fineness ratio for the same edge configuration. Looking at Figures 3.13, 3.14 and 3.15, all turbulent flow results show larger C_D values for α larger than 4°. However, in agreement with Courchesne and Laneville [12] for a square-edge prisms at Re of $10^4 - 10^5$, turbulent flow has shown the tendency to reduce C_D compare to smooth flow results for a 2:1 prism around 0° angle of attack.

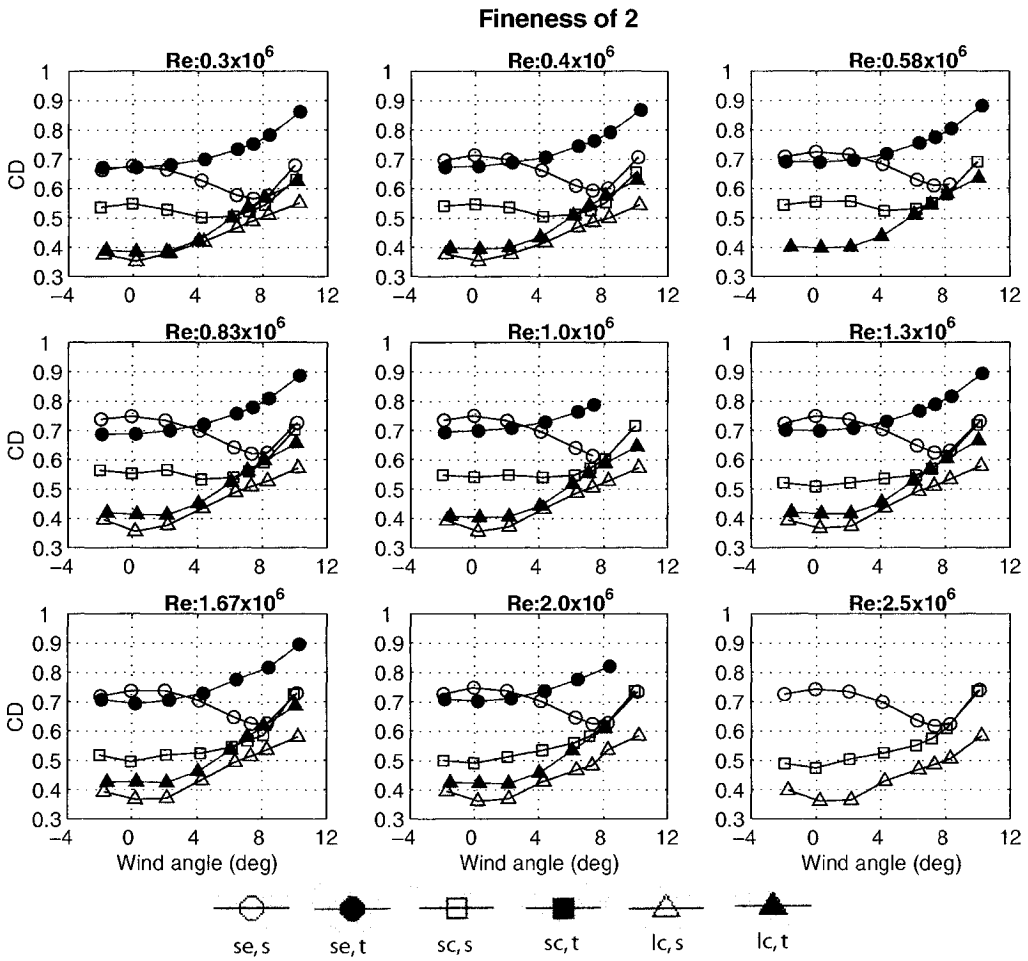

Figure 3.13: Drag coefficient versus wind angle for fineness of 2, three edge configurations, nine Reynolds numbers, in smooth (open) and turbulent (solid) flow, Mach: 0.15.

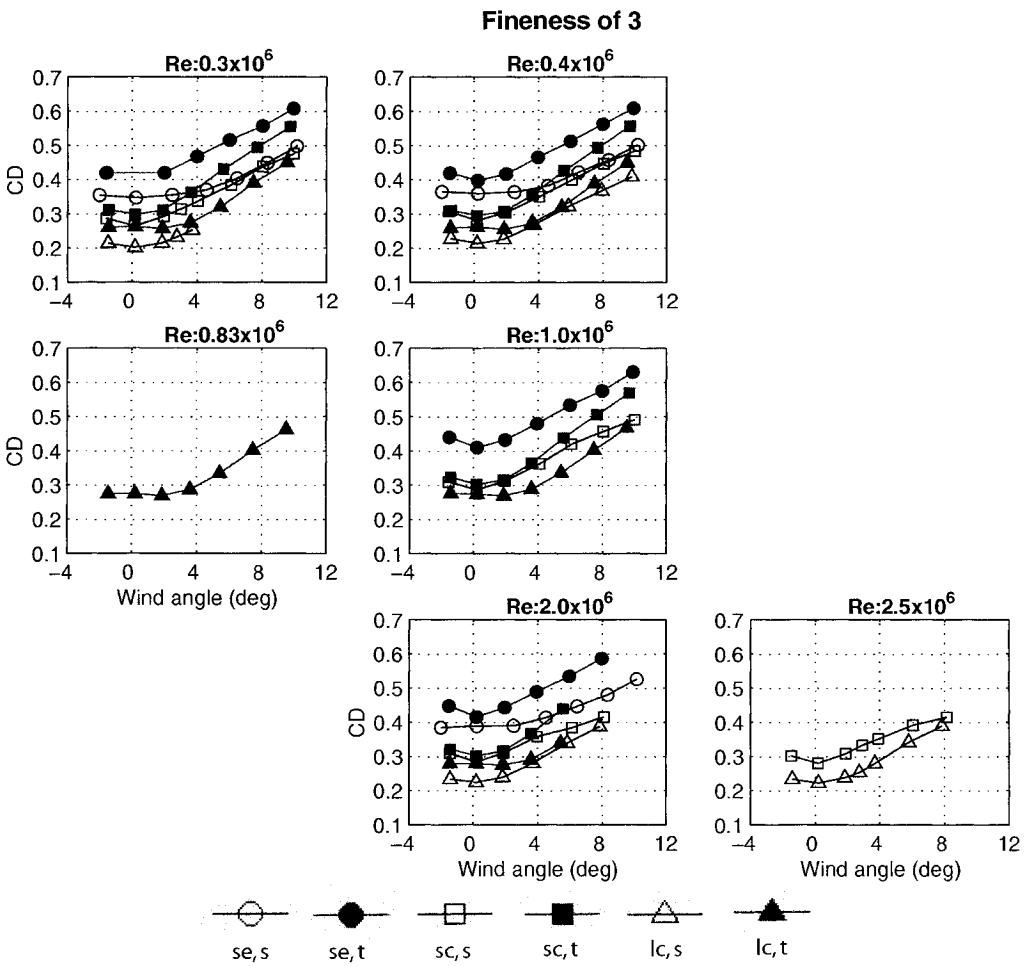

Figure 3.14: Drag coefficient versus wind angle for fineness of 3, three edge configurations, six Reynolds numbers, in smooth (open) and turbulent (solid) flow, Mach: 0.15.

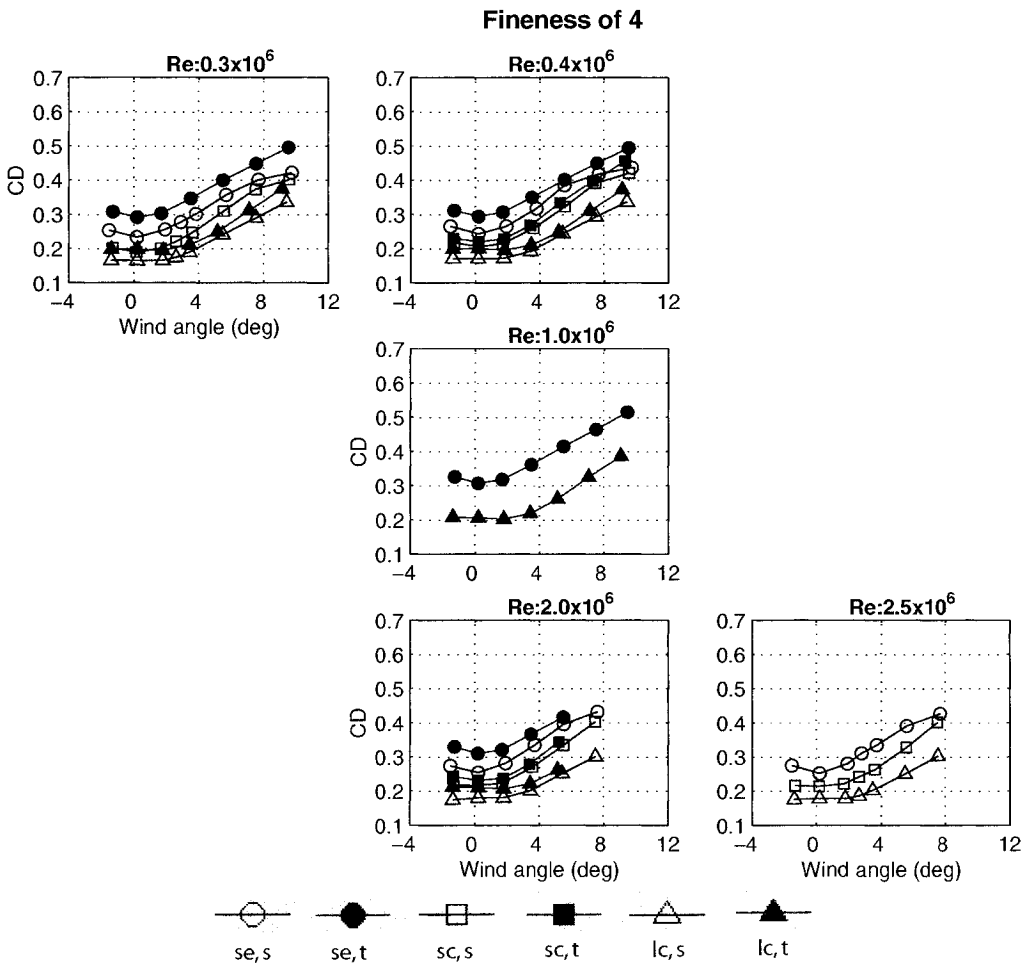

Figure 3.15: Drag coefficient versus wind angle for fineness of 4, three edge configurations, five Reynolds numbers, in smooth (open) and turbulent (solid) flow, Mach: 0.15.

3.2.2 C_D versus Re

Figures 3.16, 3.17 and 3.18 present the variations of C_D with Re for the 2:1 prisms. It is observed in Figure 3.16 that a 2:1 prism with square edges shows a variation that has exactly the same trend for all angles of attack presented with an increase of C_D up to Re of 0.83×10^6 and constant thereafter. The variation is around 11%.

For small chamfer, tests conducted at angles of attack of $-2°$ and $2°$ have shown an increase of the C_D up to a Re of 0.83×10^6 and then, a decrease of C_D for the rest of the Re range covered. However, for angles of attack of $4°$ and $6°$, there is an increase of C_D until Re of 0.83×10^6 and a plateau thereafter (Figure 3.17). The results for large chamfer do not show an important variation like the two previous configurations have shown (Figure 3.18).

For a 3:1 prism, the drag coefficient tends to increase with Re, with variation of around 10% for square-edge prisms (Figure 3.19) while small chamfer and large chamfer do not present any particular trend, and their C_D variation with Re is around 11% (Figures 3.20 and 3.21).

A 4:1 prism seems to have a C_D affected in the same way for all edge configurations tested with a small increase of the C_D at low Re and a plateau after (Figures 3.22, 3.23 and 3.24). A maximum C_D variation of 11%, based on normalisation with the smallest C_D value, is observed on the three figures. In general, the turbulence intensity reduces the Re effect on C_D regardless of the fineness or the edge configurations of the prism.

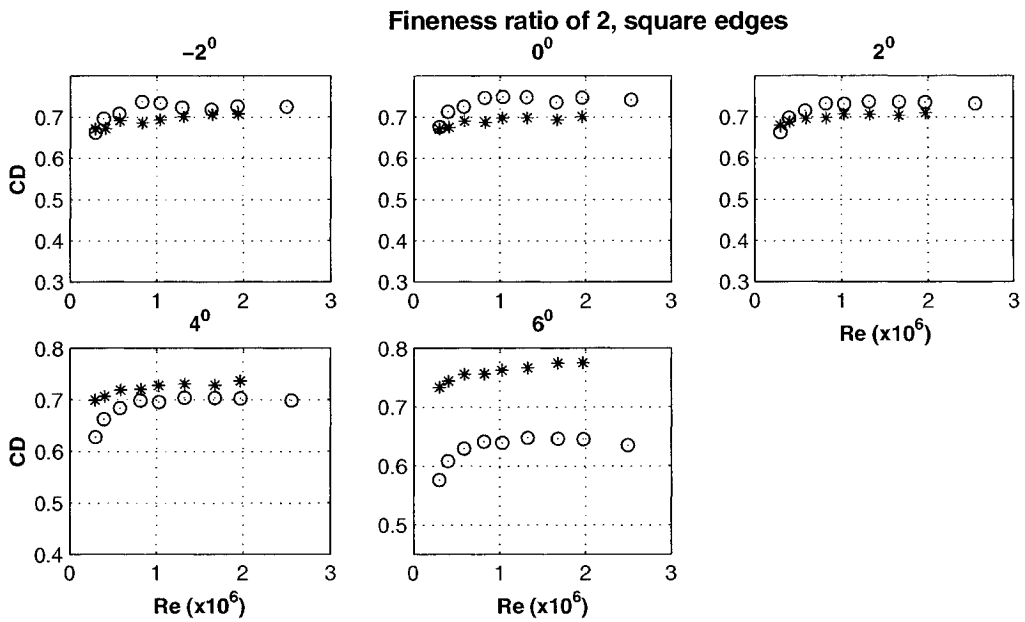

Figure 3.16: Drag coefficient versus Reynolds number for fineness of 2, square edges, five angles of attack in smooth (circle) and turbulent (star) flow, Mach: 0.15.

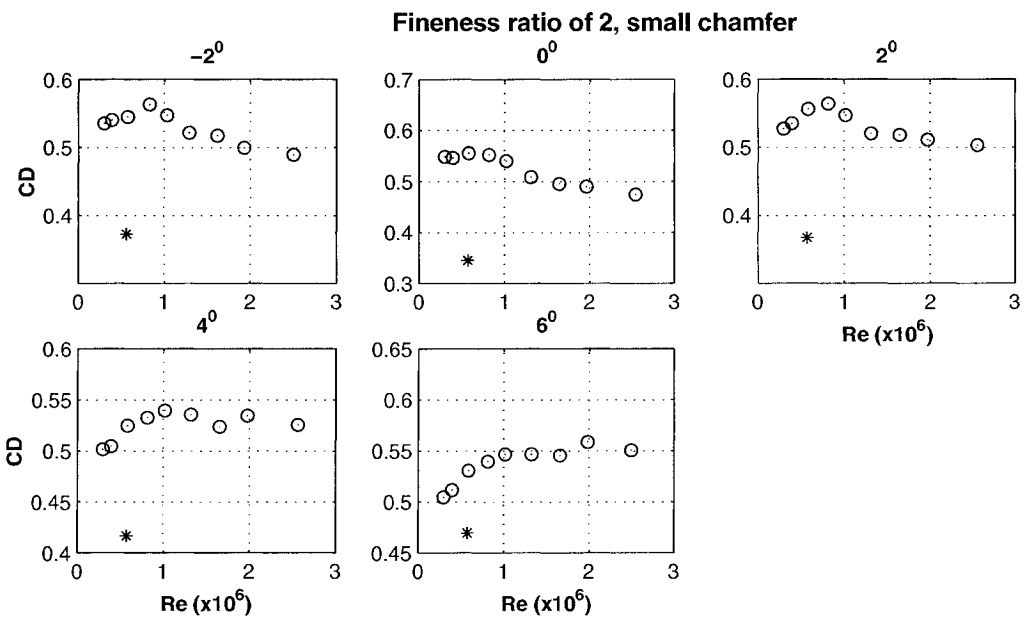

Figure 3.17: Drag coefficient versus Reynolds number for fineness of 2, small chamfer, five angles of attack in smooth (circle) and turbulent (star) flow, Mach: 0.15.

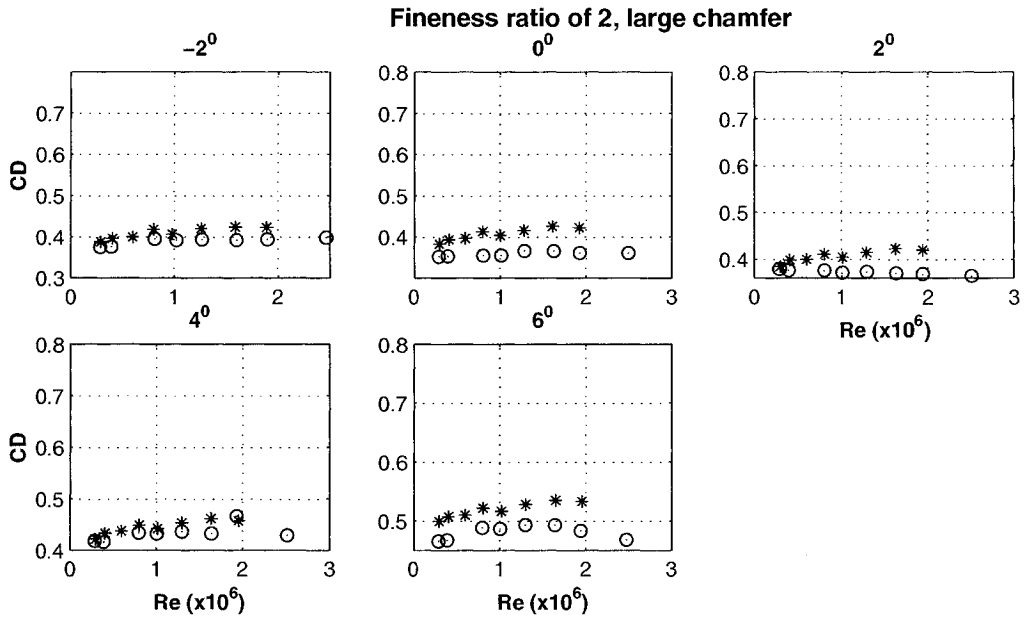

Figure 3.18: Drag coefficient versus Reynolds number for fineness of 2, large chamfer, five angles of attack in smooth (circle) and turbulent (star) flow, Mach: 0.15.

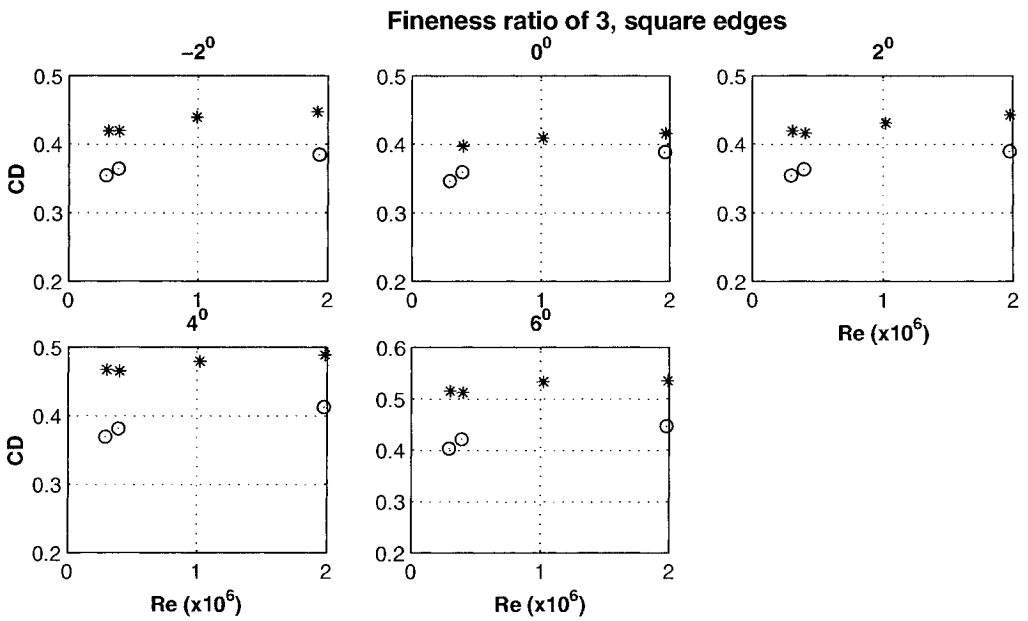

Figure 3.19: Drag coefficient versus Reynolds number for fineness of 3, square edges, five angles of attack in smooth (circle) and turbulent (star) flow, Mach: 0.15.

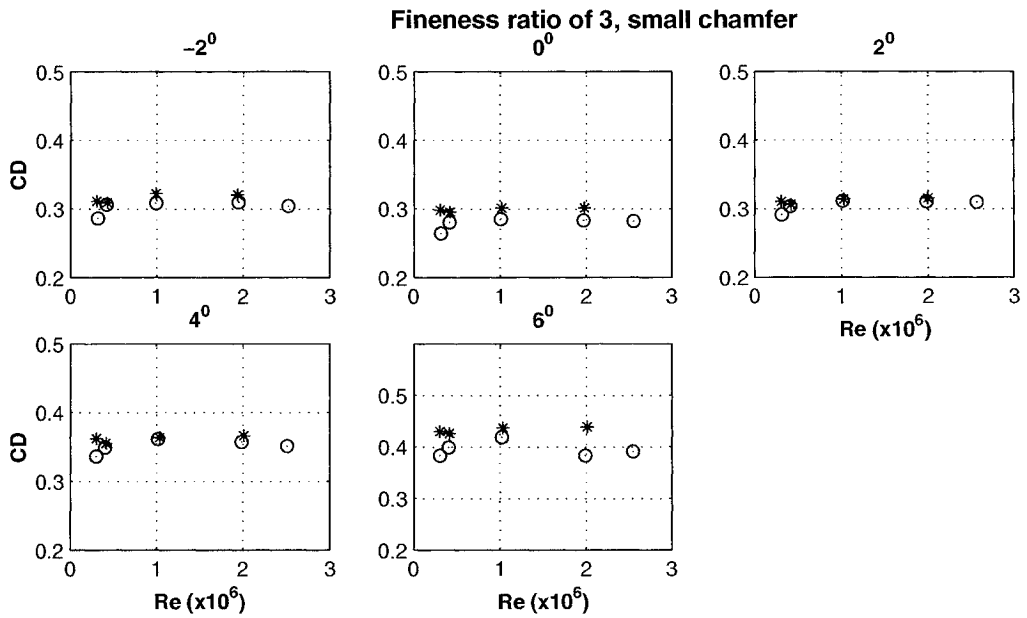

Figure 3.20: Drag coefficient versus Reynolds number for fineness of 3, small chamfer, five angles of attack in smooth (circle) and turbulent (star) flow, Mach: 0.15.

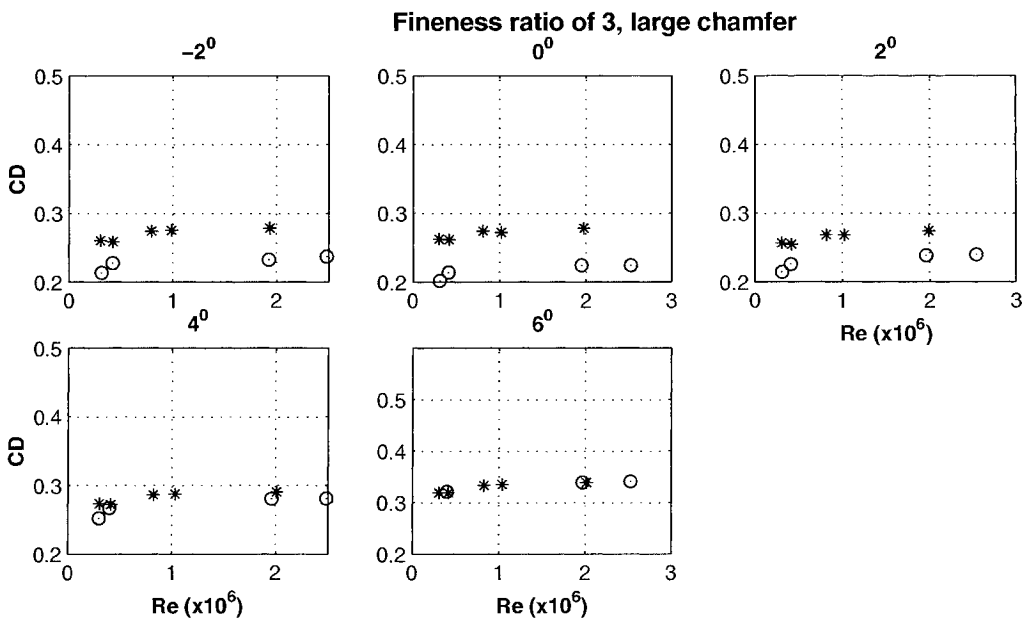

Figure 3.21: Drag coefficient versus Reynolds number for fineness of 3, large chamfer, five angles of attack in smooth (circle) and turbulent (star) flow, Mach: 0.15.

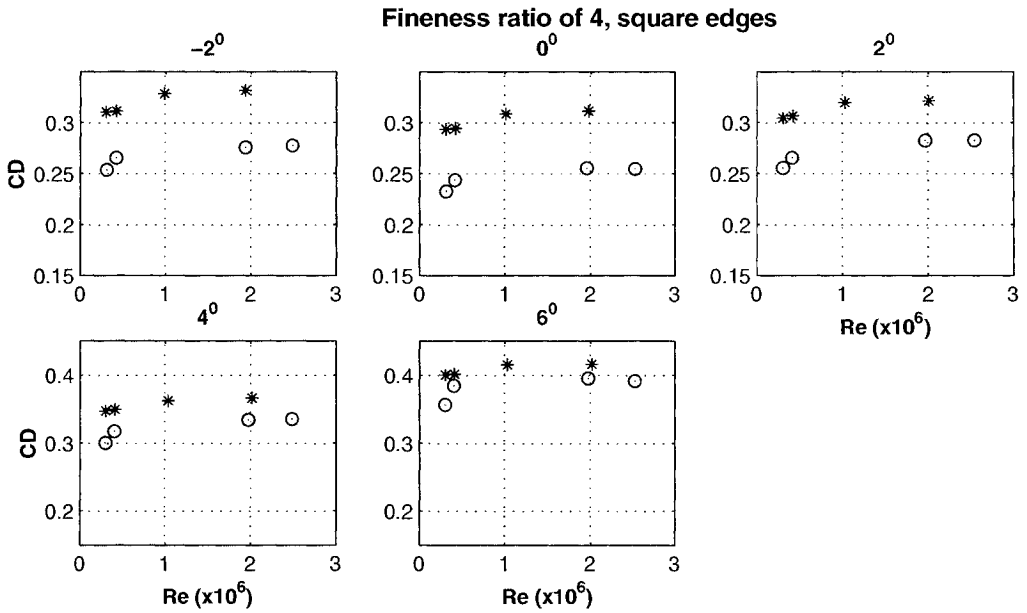

Figure 3.22: Drag coefficient versus Reynolds number for fineness of 4, square edges, five angles of attack in smooth (circle) and turbulent (star) flow, Mach: 0.15.

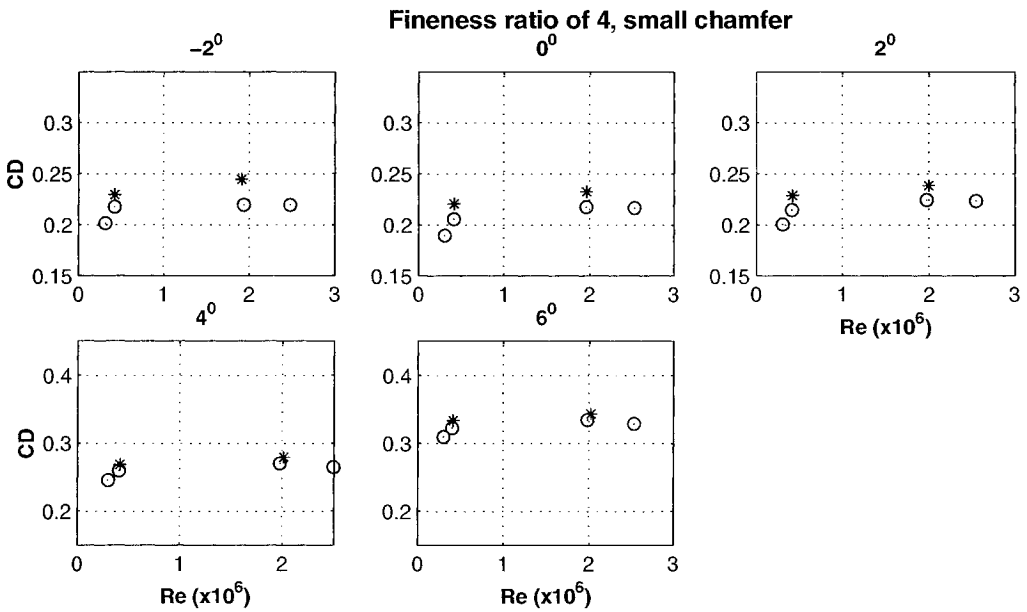

Figure 3.23: Drag coefficient versus Reynolds number for fineness of 4, small chamfer, five angles of attack in smooth (circle) and turbulent (star) flow, Mach: 0.15.

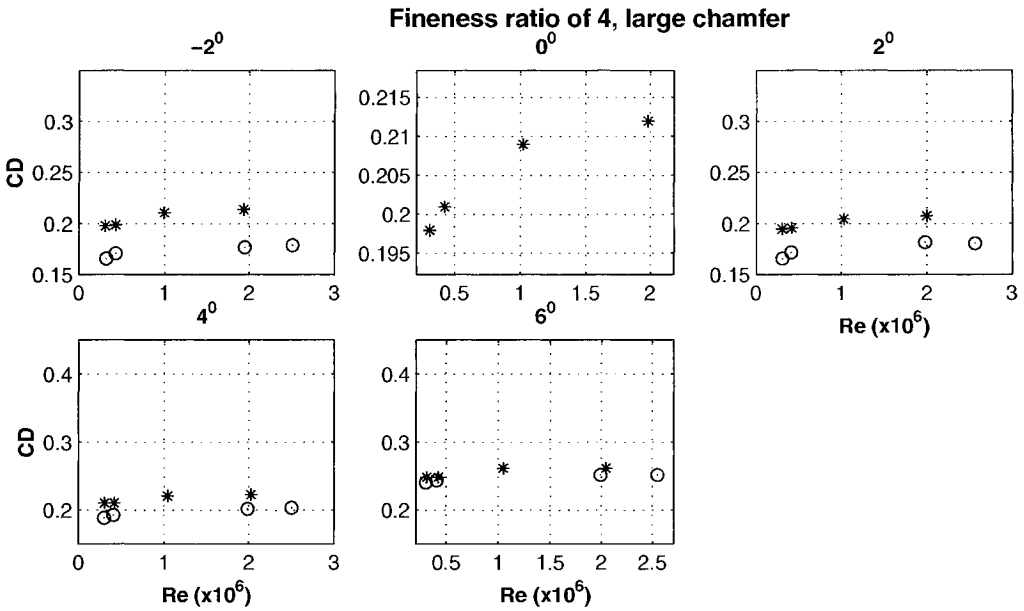

Figure 3.24: Drag coefficient versus Reynolds number for fineness of 4, large chamfer, five angles of attack in smooth (circle) and turbulent (star) flow, Mach: 0.15.

3.3 Pitching moment coefficient C_M

3.3.1 C_M versus α

The sign convention applied for the pitching moment coefficient is a positive C_M given for the conditions shown on Figure 3.25. Thus, it is expected for a positive angle of attack, a positive C_M up to a stall angle where the pitching moment reaches its maximum value.

From Figure 3.26, all graphs show a negative C_M with angle of attack positive except for large chamfer in turbulent flow that has a positive C_M until α of 4° and then, C_M is equal to zero at 6° and negative for higher angles of attack. This positive slope of C_M at 0° is in agreement with the curve for the same prism for the lift coefficient C_L on Figure 3.1.

However, for a 3:1 prism, small chamfer in turbulent flow and large chamfer in smooth and turbulent flow have a positive C_M for positive angles of attack. There is a maximum angle for which the C_M value starts to decrease and this angle is moved to higher angles of attack in turbulent flow in comparison with smooth flow (Figure 3.27). For example, the results for large chamfer show the highest C_M value at 6° in turbulent flow while in smooth flow the maximum C_M occurs at angle of 2°.

Finally, the results for fineness ratio of 4 presents the same characteristics than 3:1 prism. However, square edges in turbulent flow and small chamfer in smooth flow have a positive moment slope at low angle of attack with positive C_M at α of 2° (Figure 3.28). There is an important effect of the edge treatment on C_M. As Figure 3.28 shows, square

edges and large chamfer are not in the same range of C_M value with a maximum at 0.12 for large chamfer that corresponds to a maximum of -0.03 for square edges for the same angle of attack.

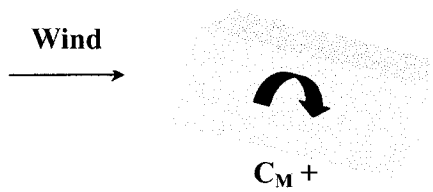

Figure 3.25: Sign convention for positive pitching moment coefficient.

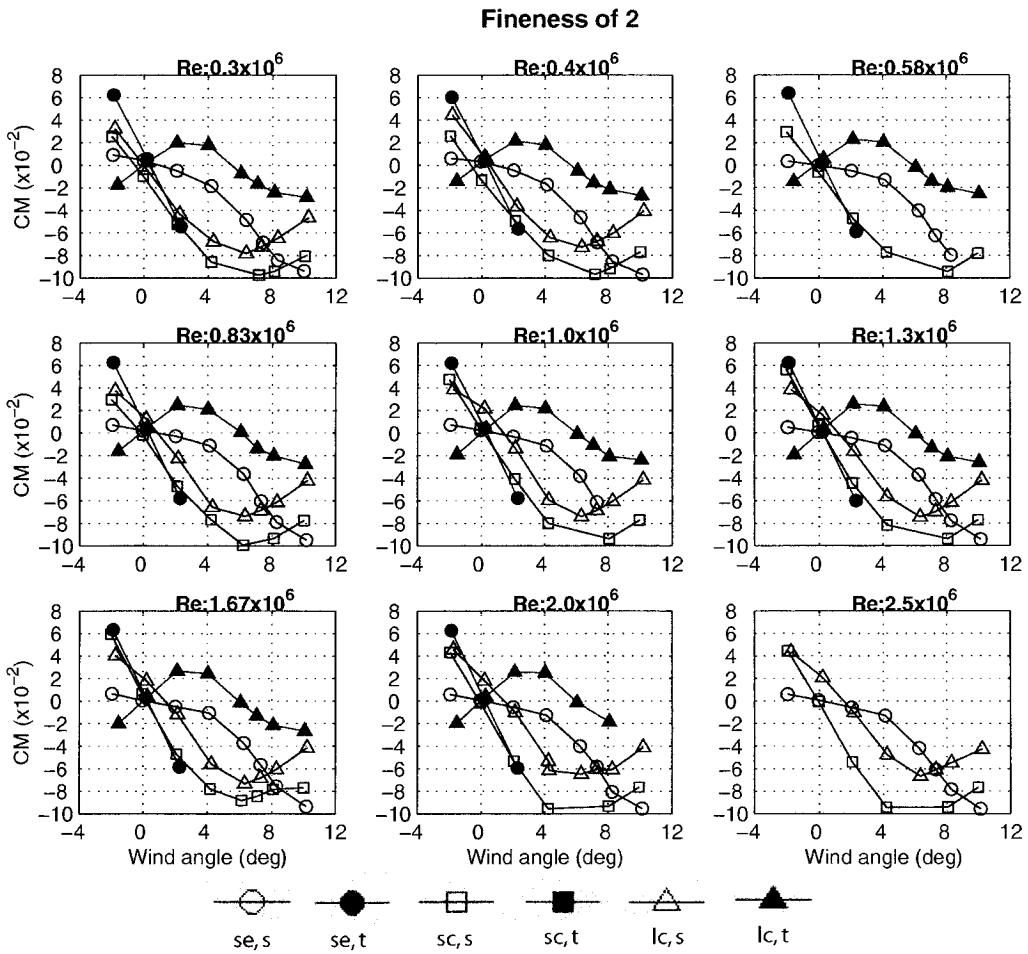

Figure 3.26: Pitching moment coefficient versus wind angle for fineness of 2, three edge configurations, nine Reynolds numbers, in smooth (open) and turbulent (solid) flow, Mach: 0.15.

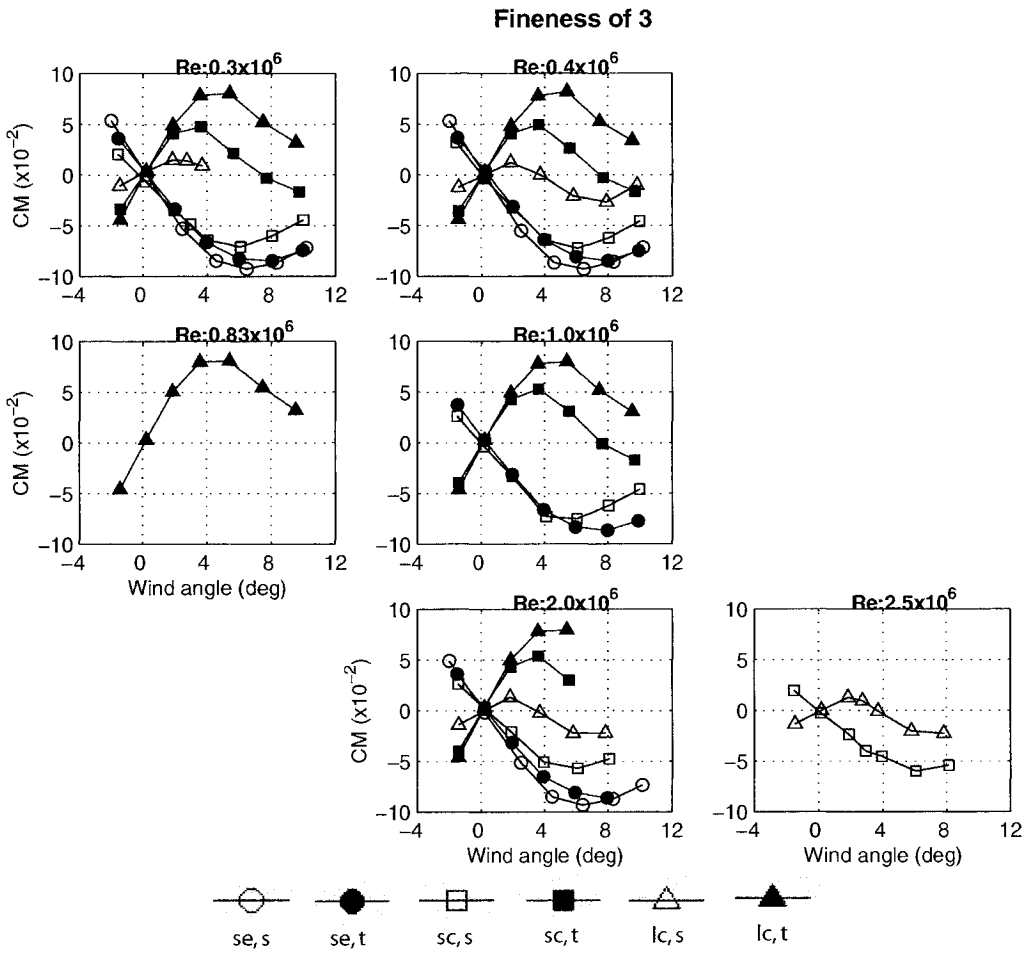

Figure 3.27: Pitching moment coefficient versus wind angle for fineness of 3, three edge configurations, six Reynolds numbers, in smooth (open) and turbulent (solid) flow, Mach: 0.15.

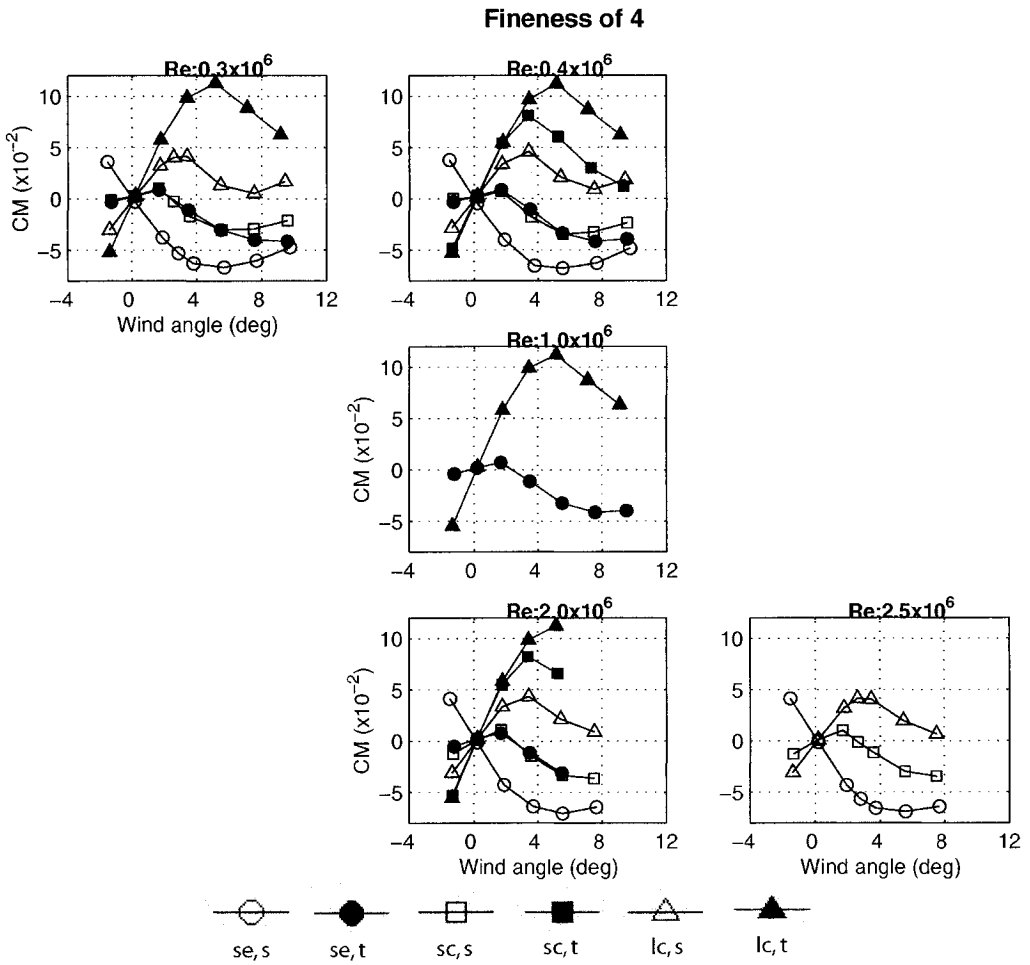

Figure 3.28: Pitching moment coefficient versus wind angle for fineness of 4, three edge configurations, five Reynolds numbers, in smooth (open) and turbulent (solid) flow, Mach: 0.15.

Chapter 4

Surface pressure measurements

4.1 Steady surface pressure coefficient C_P

Surface pressure measurements were made on a chord-wise strip of each prism and results are presented using mean pressure coefficient C_P.

$$C_P = \frac{P_i - PI}{q} \tag{4.1.1}$$

where:

P_i: Local pressure at the pressure tap i on the chord-wise strip;

PI: static pressure reference;

q: dynamic pressure.

The pressure taps are shown on Figures 4.1, 4.2 and 4.3 for an angle of attack of 0°. These figures present the cross-section of the prism and lines inside of the cross-section means a positive pressures while lines around the cross-section represent a negative pressure. The magnitude of C_P is normalised using the depth of the prism: C_P of 1 is represented by a line with a half-depth length. There are three figures, each for a different fineness ratio and on each figure, the three edge configurations are presented with results in smooth and

turbulent flow for two Re, 0.4×10^6 and 2.0×10^6.

4.1.1 C_P distribution at 0°

The mean local surface pressure distribution around a prism with square edges did not change with Re as shown on Figure 4.1. However, the turbulence intensity modified the pressure pattern by reducing the suction at the top and bottom surfaces toward the trailing edge. For small chamfer and large chamfer in smooth flow, the pressure distribution was affected by Re variation with again a reduction of the suction near the trailing edge.

Thus, the effect of increasing turbulence intensity is similar to increasing Re. However, the effect of Re is not clear for turbulent flow as opposed to what was observed in smooth flow.

By inspection of Figure 4.2, it can be concluded that the prism with a 3:1 fineness ratio was slightly affected by Re only for the small chamfer configuration in smooth flow with a small reduction of the suction close the trailing edge of the prism. On the other hand, turbulence intensity affected the square edge, small and large chamfer configurations at both Re presented here (Figure 4.2).

Finally, the 4:1 prism did not show sensitivity to Re for all the edge configurations tested and, turbulence has still an impact on the pressure distribution but is less important and significant than for the 2:1 and 3:1 prisms (Figure 4.3).

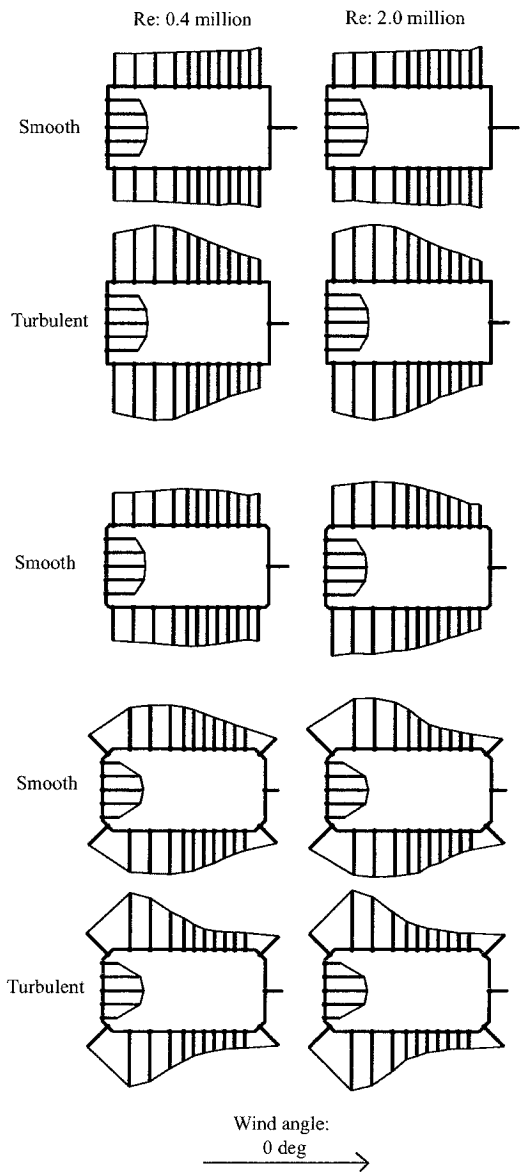

Figure 4.1: Static pressure coefficient C_P, at 0°, fineness of 2, three edge configurations (square edges at the top, small chamfer in the middle and large chamfer at the bottom), smooth and turbulent flow, two Reynolds numbers, Mach: 0.15.

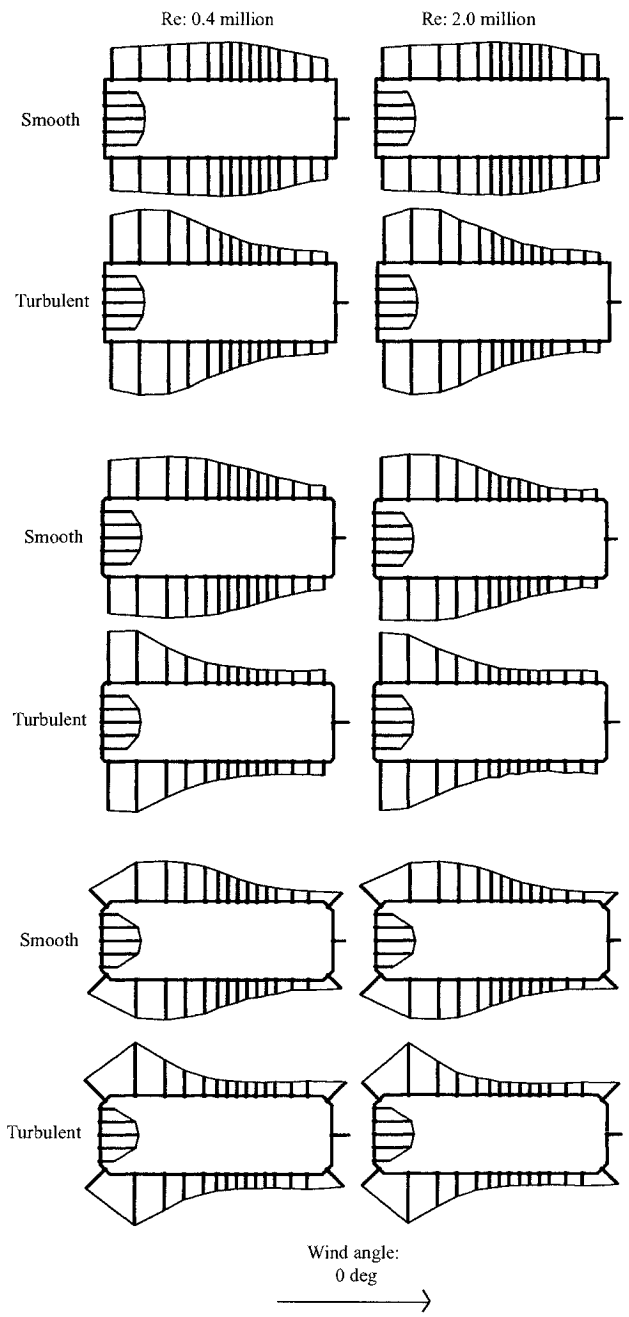

Figure 4.2: Static pressure coefficient C_P, at 0°, fineness of 3, three edge configurations (square edges at the top, small chamfer in the middle and large chamfer at the bottom), smooth and turbulent flow, two Reynolds numbers, Mach: 0.15.

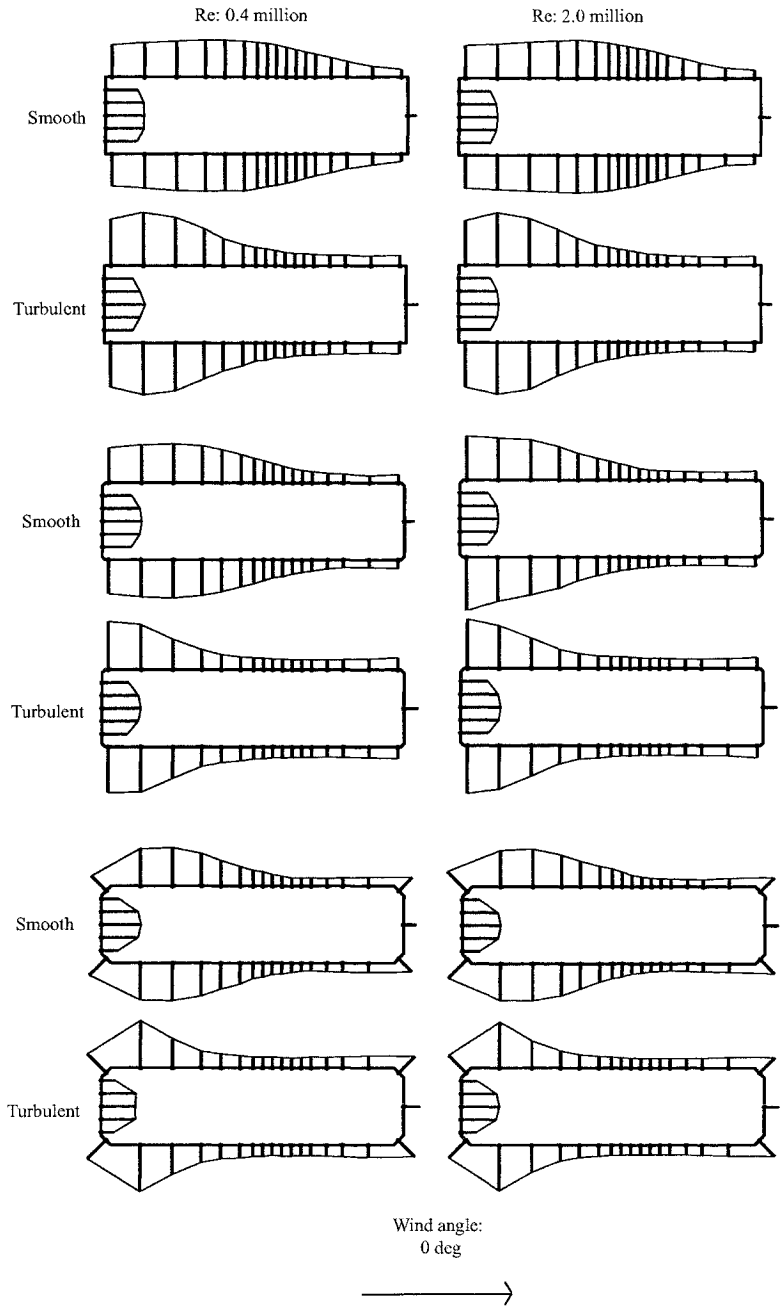

Figure 4.3: Static pressure coefficient C_P, at 0°, fineness of 4, three edge configurations (square edges at the top, small chamfer in the middle and large chamfer at the bottom), smooth and turbulent flow, two Reynolds numbers, Mach: 0.15.

4.1.2 C_P distribution at 6°

Local surface pressure coefficient C_P at 6° have shown similarity and some differences with results at 0°. First, the prism with a fineness ratio of 2 did not show *Re* sensitivity in smooth and in turbulent flow as it was the case for 0° particularly for small and large chamfer (Figure 4.4).

However, for 3:1 prism on Figure 4.5, the behaviour is quite the same with a small variation of the local surface pressure distribution at the top of the prism and a 4:1 prism do not present significant variation of C_P with *Re* (Figure 4.6). All prisms in turbulent flow do not seem to be affected by the variation of *Re*.

On the other hand, turbulence intensity changes the flow pressure around the bluff body at low *Re*. While there is less suction at the bottom of the prism for square edges and small chamfer, turbulence for large chamfer tends to increase the negative pressure at the top of the prism and reduce it at the bottom that is different than results obtained at 0°.

For a 3:1 and 4:1 prisms, turbulence intensity acts in the same way. It increases the suction for the first part at the top of the prism and the bottom has less negative pressure than in smooth flow.

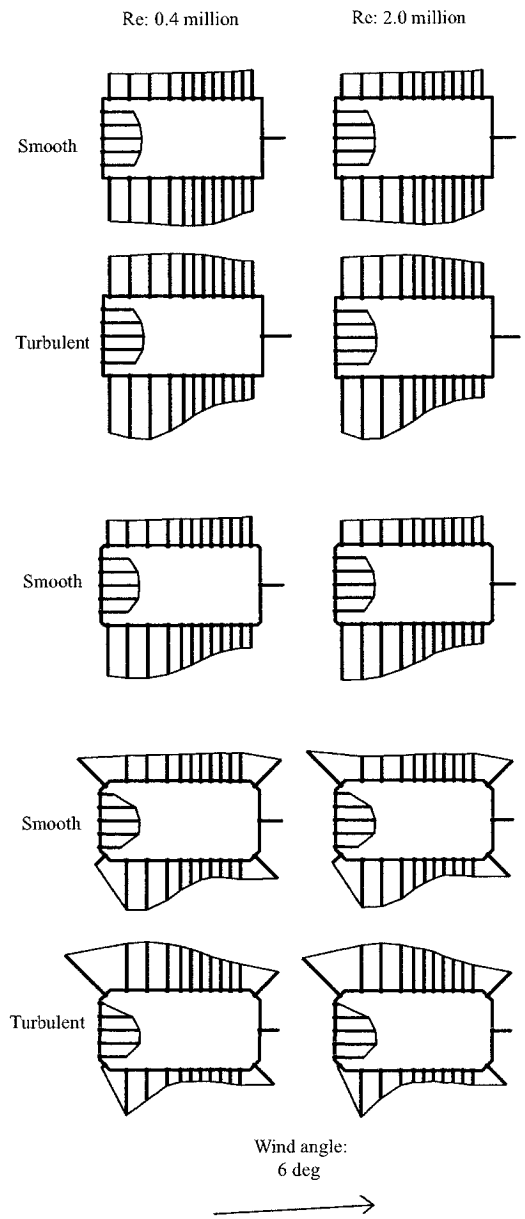

Figure 4.4: Static pressure coefficient C_P, at 6°, fineness of 2, three edge configurations (square edges at the top, small chamfer in the middle and large chamfer at the bottom), smooth and turbulent flow, two Reynolds numbers, Mach: 0.15.

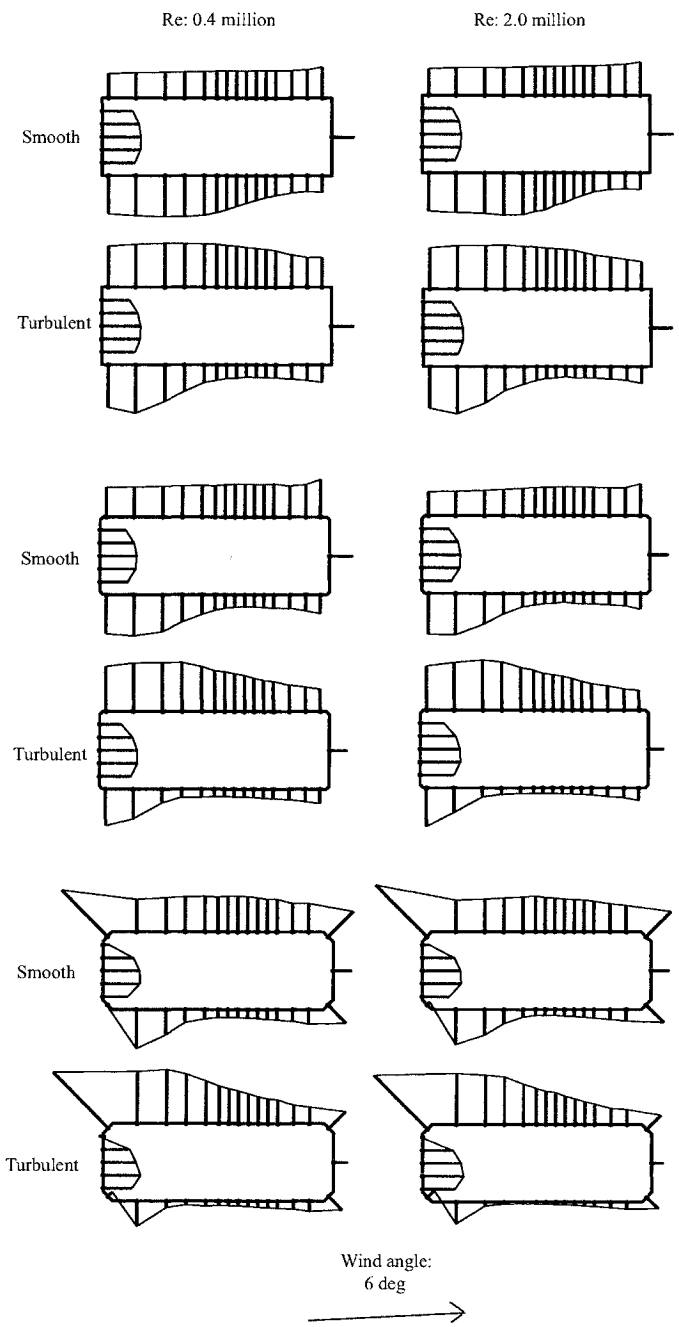

Figure 4.5: Static pressure coefficient C_P, at 6°, fineness of 3, three edge configurations (square edges at the top, small chamfer in the middle and large chamfer at the bottom), smooth and turbulent flow, two Reynolds numbers, Mach: 0.15.

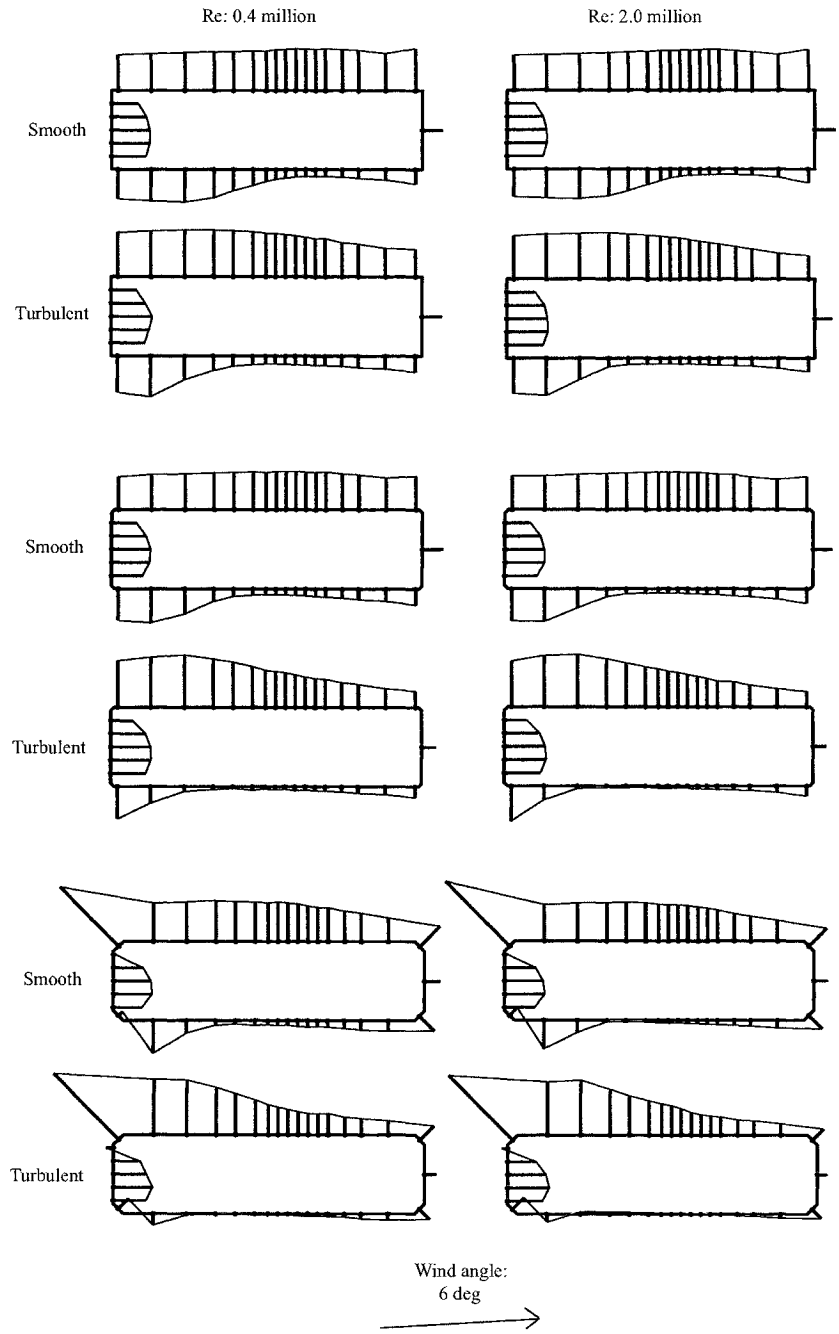

Figure 4.6: Static pressure coefficient C_P, at 6°, fineness of 4, three edge configurations (square edges at the top, small chamfer in the middle and large chamfer at the bottom), smooth and turbulent flow, two Reynolds numbers, Mach: 0.15.

4.1.3 Relation between mean C_P and reattachment

A strong indication of the separation-reattachment phenomenon is given by the pressure variation along the top and the bottom surfaces of the prism. A positive local surface pressure could be interpreted as a flow reattachment on the top surface for example. Table 4.1 presents the reattachment possibility based on the mean local surface pressure C_P on the top and bottom surfaces of the prism.

As it can be observed in Table 4.1, there is no visible reattachment of the shear layer on the surfaces of the prism for a 2:1 and 3:1 fineness ratio in both flow condition. Otherwise, the 4:1 prism has a tendency to reattach in smooth flow for large chamfer configuration at higher angles of attack. The shear layer shows a reattachment at the mid-distance along the top or bottom surface of the prism while negative local pressure are still present close the trailing edge.

This suggests that there is probably a reattachment of the shear layer but further aft of the body, the shear layer separated again. Turbulent flow gives the opportunity to the shear layer to curves towards the body and helps the shear layer to reattach at lower angle of attack and also for a prism with smaller chamfer.

Fineness of 2, smooth and turbulent flow

Angle of attack	Square edges		Small chamfer		Large chamfer	
	Re $0.3x10^6$	*Re* $2.0x10^6$	*Re* $0.3x10^6$	*Re* $2.0x10^6$	*Re* $0.3x10^6$	*Re* $2.0x10^6$
-2^0 to 10^0	NO	NO	NO	NO	NO	NO

Fineness of 3, smooth and turbulent flow

Angle of attack	Square edges		Small chamfer		Large chamfer	
	Re $0.3x10^6$	*Re* $2.0x10^6$	*Re* $0.3x10^6$	*Re* $2.0x10^6$	*Re* $0.3x10^6$	*Re* $2.0x10^6$
-2^0 to 10^0	NO	NO	NO	NO	NO	NO

Fineness of 4, smooth flow

Angle of attack	Square edges		Small chamfer		Large chamfer	
	Re $0.3x10^6$	*Re* $2.0x10^6$	*Re* $0.3x10^6$	*Re* $2.0x10^6$	*Re* $0.3x10^6$	*Re* $2.0x10^6$
-2^0	NO	NO	NO	NO	NO	NO
0^0	NO	NO	NO	NO	NO	NO
2^0	NO	NO	NO	NO	NO	NO
3^0	NO	-	NO	-	NO	-
4^0	NO	NO	NO	NO	NO	little
6^0	NO	NO	NO	NO	NO	little
7^0	-	-	-	-	-	-
8^0	NO	NO	NO	NO	NO	little
10^0	NO	-	NO	-	little	-

Fineness of 4, turbulent flow

Angle of attack	Square edges		Small chamfer		Large chamfer	
	Re $0.3x10^6$	*Re* $2.0x10^6$	*Re* $0.3x10^6$	*Re* $2.0x10^6$	*Re* $0.3x10^6$	*Re* $2.0x10^6$
-2^0	NO	NO		NO	NO	NO
0^0	NO	NO		NO	NO	NO
2^0	NO	NO		NO	NO	NO
3^0	-	-		-	-	-
4^0	NO	NO		little	little	little
6^0	NO	NO		little	YES	YES
7^0	-	-		-	-	-
8^0	NO	-		-	YES	-
10^0	NO	-		-	YES	-

Table 4.1: Identification of reattachment on the top and/or bottom surfaces of the prism for different fineness ratio, Reynolds number, flow condition and angle of attack based on mean local surface pressure C_P.

4.2 Unsteady surface pressure coefficient C_P

Figure 4.7 presents a sequence of unsteady local surface pressure distribution C_P for different times on a chord-wise strip of the model at the centreline for a 3:1 prism with square edges. It shows large variations of C_P, with time and by using a sampling frequency of 4800 Hz, some phenomena such as vortex-shedding and shear layer reattachment can be depicted from analysis of the unsteady pressure data. From the mean pressure coefficient, reattachment on this prism was not depicted.

In fact, Figure 4.7 shows that at 0.83 and 1.67 seconds, there is a reattachment point at the top surface of the prism close the trailing edge with no more negative pressure measured. The surface pressures at the top and bottom close to the leading edge (first 1/3) do not show significant variation as the last 2/3 are showing. This could be interpreted as a separated shear layer right after the first two corners of the leading edge where a rolled-up vortex is formed. The latter can shed some vortices at a given frequency but does not disappear, keeping most of its vortical energy.

Thus, the last 2/3 of the top and the bottom of the prism could be affected by the far field flow that passes by the separated shear layer and let the latter flap against the prism and also by the vortices that could be shed from the separated shear layer. The combination of this two factors can lead to the pressure flow pattern observed on Figure 4.7 at 3.12 seconds.

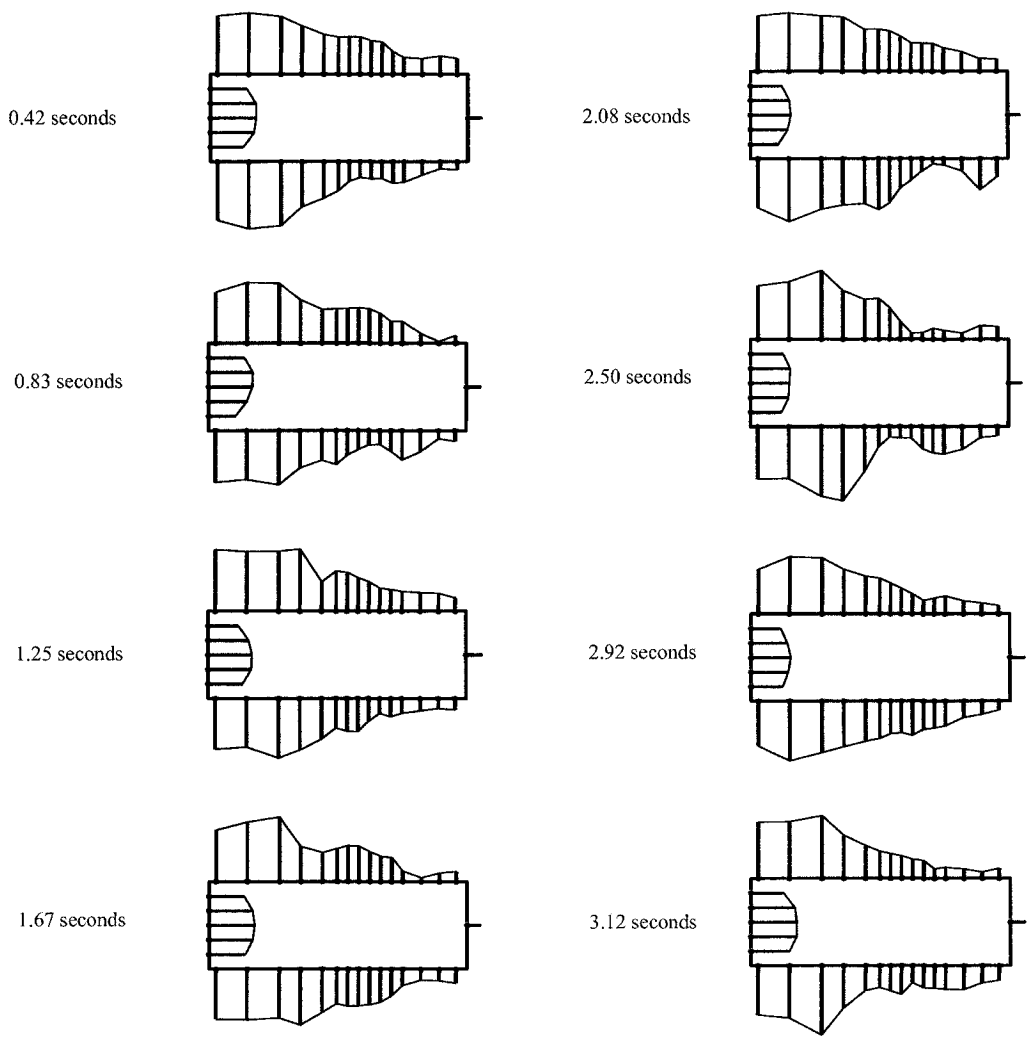

Figure 4.7: Unsteady surface pressure coefficient C_P at different times, for 0°, fineness of 3, square edges, in turbulent flow, $Re : 0.4 \times 10^6$.

4.2.1 Relation between dynamic surface pressure C_P and fluctuating reattachment

There is a permanent reattachment of the shear layer when a positive mean local surface pressure is observed at some location along the top and bottom surfaces of the prism. However, there could be also a fluctuating reattachment of the shear layer on the prism. Table 4.2 presents the possibility of reattachment based on the dynamic part of the local surface pressure time signal.

A general phenomenon observed for fluctuating local surface pressure is that there is a separated shear layer flapping on the top and bottom surfaces of the prism alternatively while a vortex is shed in the wake of the prism. This flapping shear layer phenomenon is associated with vortex shedding. There is also a high frequency surface pressure fluctuations travelling across the prism towards the trailing edge that can be responsible for reattachment. If the large vortex formed by the flapping shear layer is shed in phase with the high frequencies vortices travelling within the shear layer, there is a fluctuating reattachment observed. With turbulence added in the incoming flow, the flapping shear layer phenomena appears less important and the high frequency surface pressure fluctuations are of greatest importance.

A fineness ratio of 2 in smooth flow and with square edges exhibited no fluctuating reattachment. With small chamfer, the prism has shown a fluctuating reattachment with positive dynamic C_P for the surface pressure located very close to the trailing edge at higher

angle of attack. However, the large chamfer prism did not show has much fluctuating reattachment as the small chamfer prism and the reattachment was more concentrated midway between the leading and trailing edge on the top and bottom surfaces.

On the other hand, adding turbulence to the flow allows a 2:1 prism to exhibit more fluctuating reattachment. This dynamic reattachment occurred close to the trailing edge for lower angle of attack and moved towards midway of the bottom surface for higher angle of attack and for prism with chamfers.

The frequency at which fluctuating reattachment took place for a 2:1 prism was very small compare to the 3:1 and 4:1 prisms. The 3:1 prism with square edges has showed little fluctuating reattachment while the prism with small chamfer exhibited a high frequency of fluctuating reattachment especially for reattachment that occurs close the trailing edge at smaller angle of attack. When the reattachment was more located at mid-chord of the prism, the fluctuating reattachment reduced its frequency of occurrence.

In turbulent flow, the 3:1 prism has shown a high periodicity of fluctuating reattachment and the 4:1 prism in smooth and turbulent flow for all edge configuration exhibited fluctuating reattachment unless permanent reattachment was already present.

Fineness of 2, smooth flow

Angle of attack	Square edges		Small chamfer		Large chamfer	
	Re $0.3x10^6$	*Re* $2.0x10^6$	*Re* $0.3x10^6$	*Re* $2.0x10^6$	*Re* $0.3x10^6$	*Re* $2.0x10^6$
-2^0	NO	NO	NO	little	NO	No
0^0	NO	NO	NO	little	NO	little
2^0	NO	NO	NO	little	NO	little
3^0	NO	-	NO	-	-	-
4^0	NO	NO	little	little	NO	NO
6^0	NO	NO	little	little	NO	NO
7^0	NO	-	-	little	NO	NO
8^0	NO	NO	little	little	NO	NO
10^0	NO	NO	little	little	NO	NO

Fineness of 2, turbulent flow

Angle of attack	Square edges		Small chamfer		Large chamfer	
	Re $0.3x10^6$	*Re* $2.0x10^6$	*Re* $0.3x10^6$	*Re* $2.0x10^6$	*Re* $0.3x10^6$	*Re* $2.0x10^6$
-2^0	little	little			little	little
0^0	NO	NO			little	NO
2^0	little	little			little	NO
3^0	-	-			-	-
4^0	little	little			little	little
6^0	little	little			little	little
7^0	little	-			little	-
8^0	little	little			little	NO
10^0	little	NO			little	-

Fineness of 3, smooth flow

Angle of attack	Square edges		Small chamfer		Large chamfer	
	Re $0.3x10^6$	*Re* $2.0x10^6$	*Re* $0.3x10^6$	*Re* $2.0x10^6$	*Re* $0.3x10^6$	*Re* $2.0x10^6$
-2^0	little	little	NO	YES	YES	YES
0^0	little	little	YES	YES	YES	YES
2^0	little	little	YES	YES	YES	YES
3^0	little	-	YES	-	YES	-
4^0	little	little	YES	YES	YES	YES
6^0	little	little	little	YES	-	YES
7^0	little	-	-	-	-	-
8^0	little	little	little	YES	-	YES
10^0	little	little	little	-	-	-

Fineness of 3: turbulent, Fineness of 4: smooth and turbulent flow

Angle of attack	Square edges		Small chamfer		Large chamfer	
	Re $0.3x10^6$	*Re* $2.0x10^6$	*Re* $0.3x10^6$	*Re* $2.0x10^6$	*Re* $0.3x10^6$	*Re* $2.0x10^6$
-2^0 to 10^0	YES	YES	YES	YES	YES	YES

Table 4.2: Identification of reattachment on the top and/or bottom surfaces of the prism for different fineness ratio, Reynolds number, flow condition and angle of attack based on dynamic positive local surface pressure C_P.

Chapter 5

Wake measurements

Prisms with sharp edges have a flow separation that generally occurs at the leading edge and a separated shear layer is formed including, when fineness ratio does allow it, a separation bubble starting at the leading edge of the prism where vortices are accumulated and shed in the wake of the prism at a given frequency.

During this investigation, the frequencies of the vortices shed by the prisms were measured using a hot-wire and results of the power spectral density (PSD) of the hot-wire signals are shown on Figures 5.1 to 5.9. The hot-wire in the wake of the prism aimed at depicting von Kármán vortex shedding and any other flow fluctuations with a narrow band spectral response that could be linked to vortex shedding or shear-layer fluctuations.

The amplitude of the PSD on the following figures is not significant since the hot-wire was not calibrated but, comparison between two graphs is possible and gives information on magnitude of the flow fluctuations and the frequency at which they occurred. An analysis of the influence of the test parameters on the vortex shedding is presented in Chapter 6.2.

5.1 Power spectral densities for a 2:1 prism

First of all, the original location of the hot-wire wake probe did not allowed an effective measure of vortex shedding for all tests done with square edge prisms and small chamfer prism in smooth flow. A wake traverse flow investigation was performed following these tests to position correctly the hot-wire wake probe longitudinally and vertically from the trailing edge of the prism. The results of this investigation was presented in Table 2.1.

Thus, as it can be observed on Figure 5.1, a 2:1 prism with square edges shows spurious peaks at Re of 0.4×10^6 in smooth flow. The peaks at 60, 180, 300, 420 Hz are likely linked to noise from electrical signal and from the fact that the hot-wire was not well positioned to detect vortex shedding in the wake of the prism.

However, a peak at higher Re is observed on the top right graph at frequency $\approx$ 200 Hz that again can not be associated with vortex shedding due to the location of the hot-wire in the wake. However, the turbulent flow case does not present any obvious peak that could have been related to a vortex shedding phenomenon.

Looking at Figure 5.2, there is only a peak around 90 Hz for α of 10° while at high Re, the narrow-band disappeared. The physical interpretation of these results is not useful since the response could have been completely different with the hot-wire probe positioned at a better location in the wake.

Finally, the large chamfer configuration has clearly shown a peak of vortex shedding

for the four graphs on Figure 5.3. The hot-wire probe was located at the best position to measure the fluctuations in the wake signal (Table 2.1). This peak is located at 110 Hz except in smooth flow at the higher *Re* where the peak is moved forward to 150 Hz.

In smooth flow, for $Re : 0.4 \times 10^6$, some angles of attack of the prism did not show a peak. This is the case for $-2°$, $0°$ and $2°$ while it is the $10°$ in turbulent flow at higher *Re* that presents this situation. Regarding the amplitude of the energy, Figure 5.3 shows that the higher *Re* cases on the right side of the figure have a reduced amount of energy compare to the cases at low *Re* at the left.

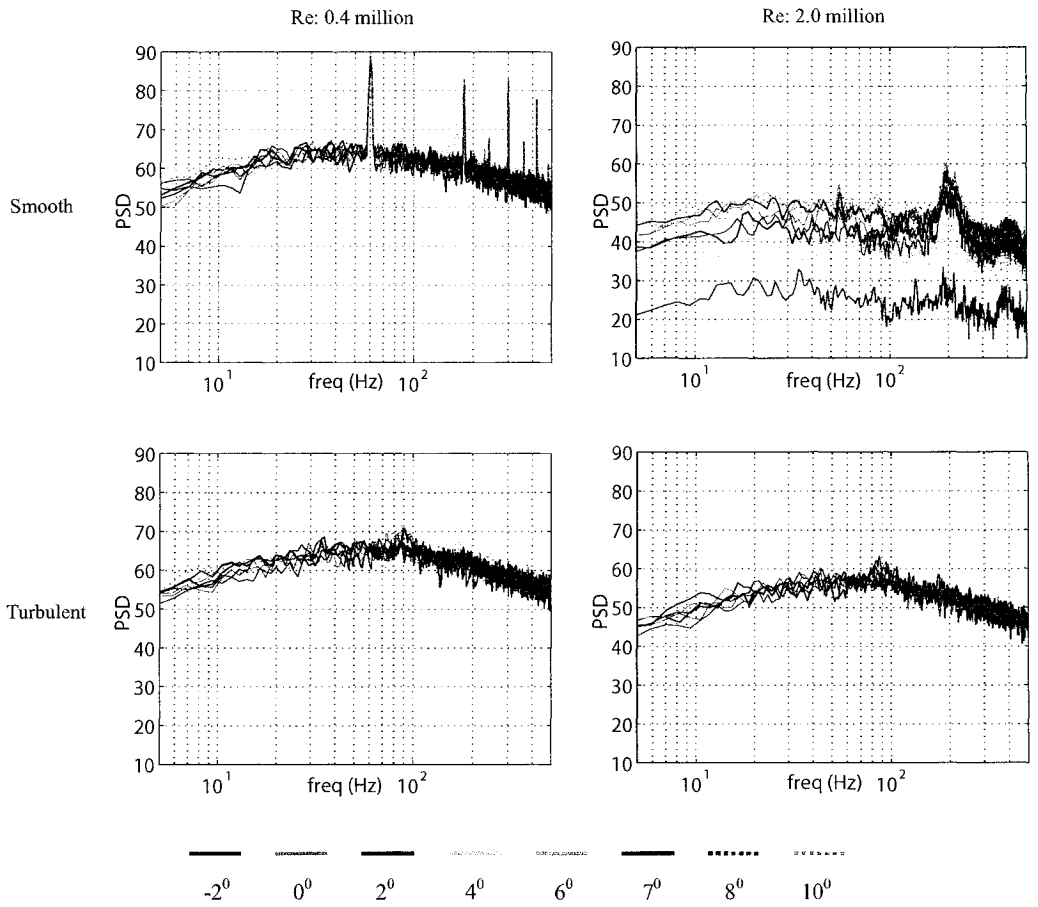

Figure 5.1: Power spectral densities of the hot-wire signal in wake of the prism, fineness of 2, square edges, smooth (top), turbulent (bottom), $Re : 0.4 \times 10^6$ (left), $Re : 2.0 \times 10^6$ (right).

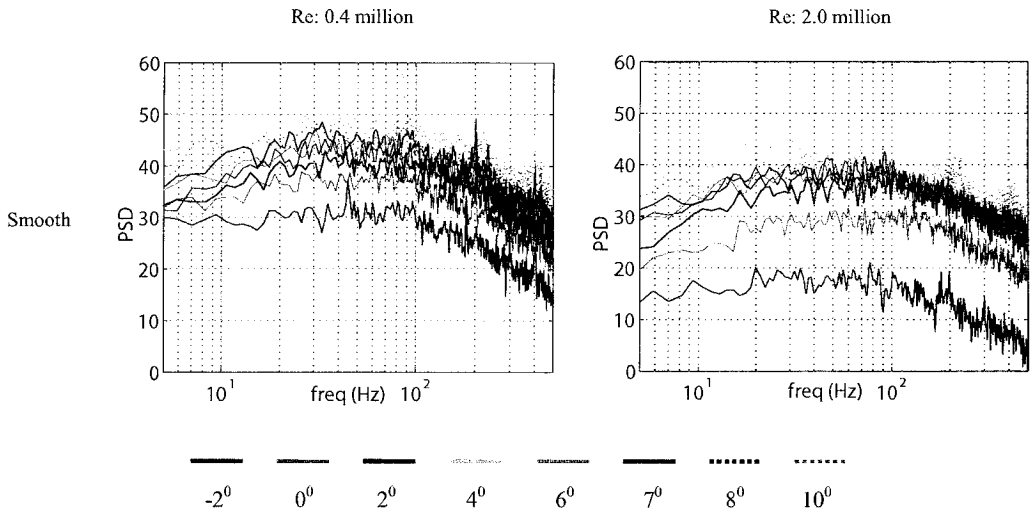

Figure 5.2: Power spectral densities of the hot-wire signal in wake of the prism, fineness of 2, small chamfer, smooth flow, $Re : 0.4 \times 10^6$ (left), $Re : 2.0 \times 10^6$ (right).

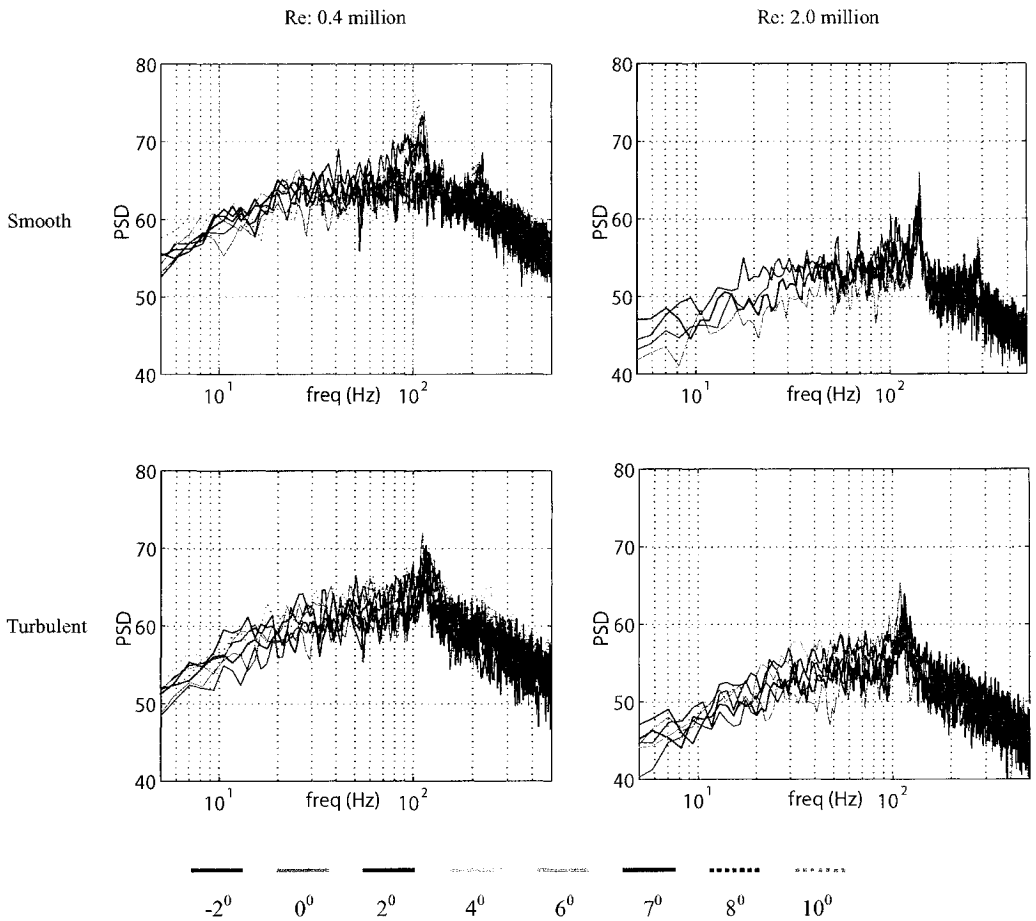

Figure 5.3: Power spectral densities of the hot-wire signal in wake of the prism, fineness of 2, large chamfer, smooth (top), turbulent (bottom), $Re : 0.4 \times 10^6$ (left), $Re : 2.0 \times 10^6$ (right).

5.2 Power spectral densities for a 3:1 prism

For a 3:1 prism, Figure 5.4 presents a peak only for the higher angles of attack of 6°, 8° and 10° at approximatively 180 Hz, 170 Hz and 160 Hz respectively. The peaks tend to move to higher value with a smaller angle of attack. By increasing the *Re* while staying in smooth flow, the peak only appears for 6° at 90 Hz and 180 Hz, for 8° at 170 Hz and for 10° at 160 Hz. With an increase of turbulence intensity the peak only appeared for 8° at 90 Hz and for 10° at 160 Hz while at high *Re*, the narrow-band frequency peak disappeared.

For small chamfers, the graph at the top left on Figure 5.5 shows vortex-shedding peaks at 100 Hz and 200 Hz at 6°, 90 Hz and 180 Hz at 8° and 170 Hz at 10°. At high *Re*, there is no evidence for a vortex-shedding peak.

For large chamfer prisms, the four graphs on Figure 5.6 show a peak at 100 Hz to 120 Hz depending on the angle of attack except for the 10° at low *Re* in smooth flow that presents a peak at 200 Hz.

Thus, for a fineness ratio of 3 and large chamfer prism, increasing *Re* as well as increasing turbulence intensity do not help to mitigate the vortex-shedding peak.

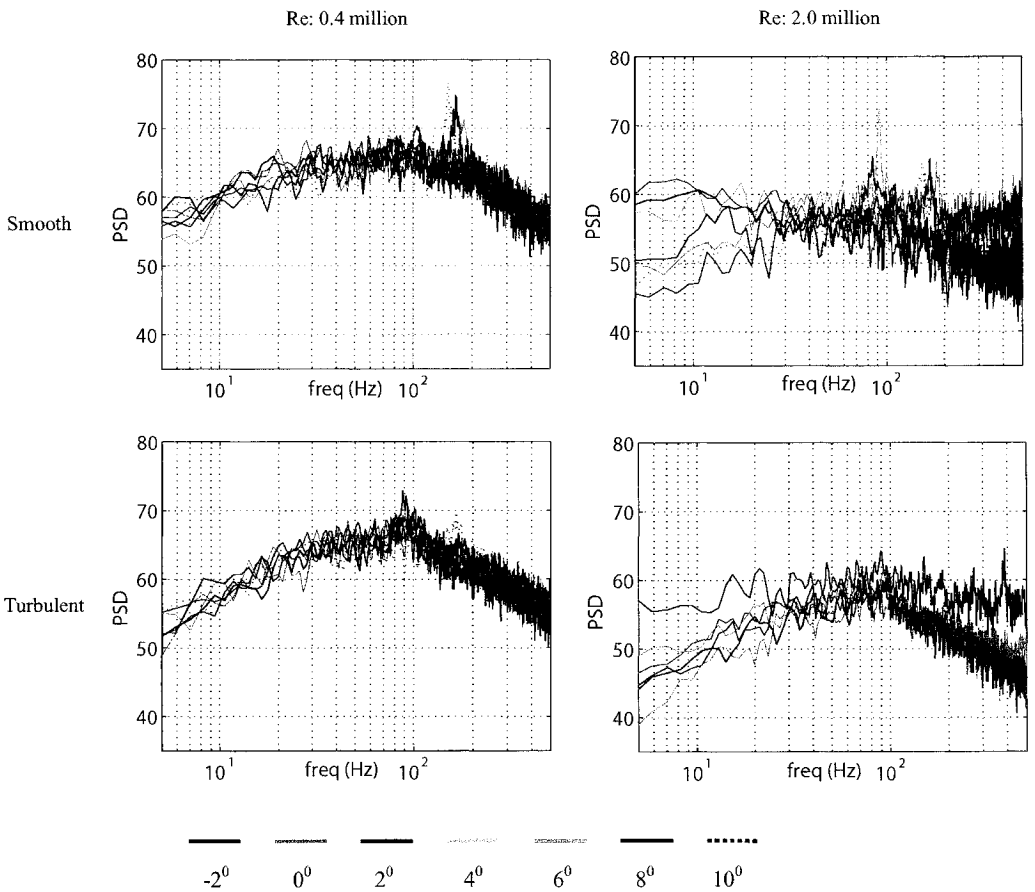

Figure 5.4: Power spectral densities of the hot-wire signal in wake of the prism, fineness of 3, square edges, smooth (top), turbulent (bottom), $Re : 0.4 \times 10^6$ (left), $Re : 2.0 \times 10^6$ (right).

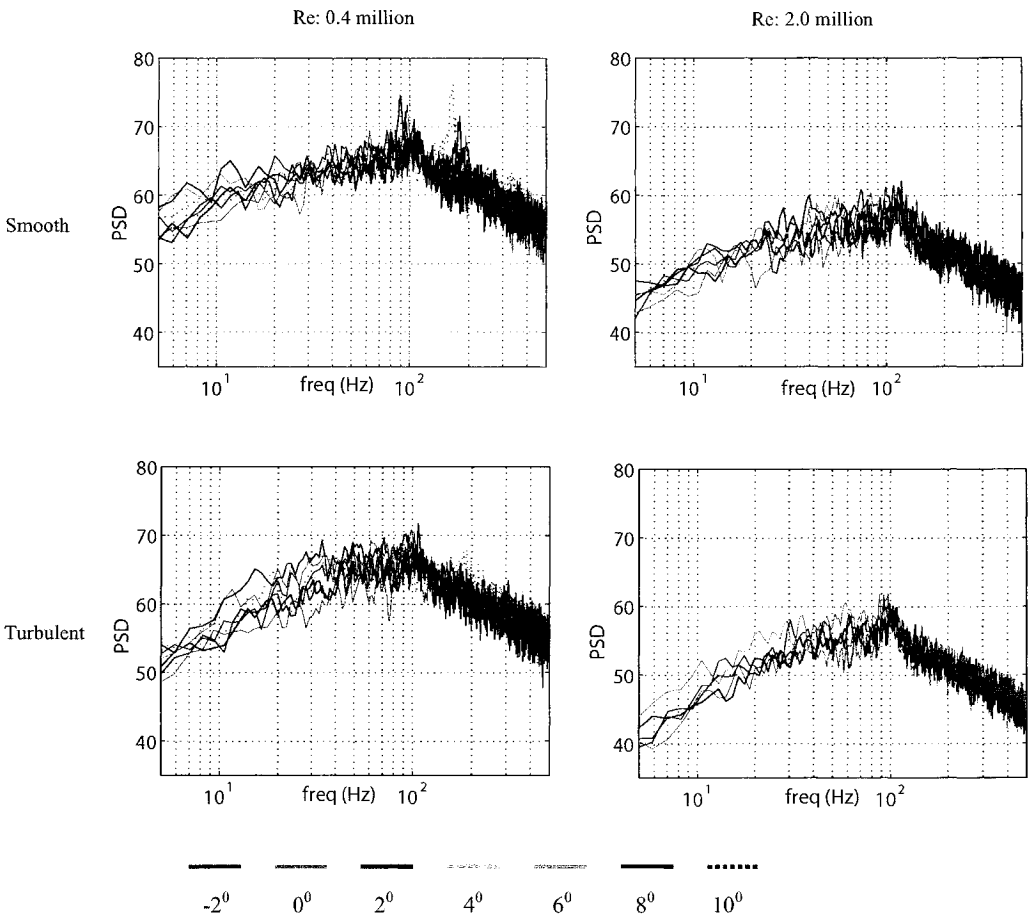

Figure 5.5: Power spectral densities of the hot-wire signal in wake of the prism, fineness of 3, small chamfer, smooth (top), turbulent (bottom), $Re : 0.4 \times 10^6$ (left), $Re : 2.0 \times 10^6$ (right).

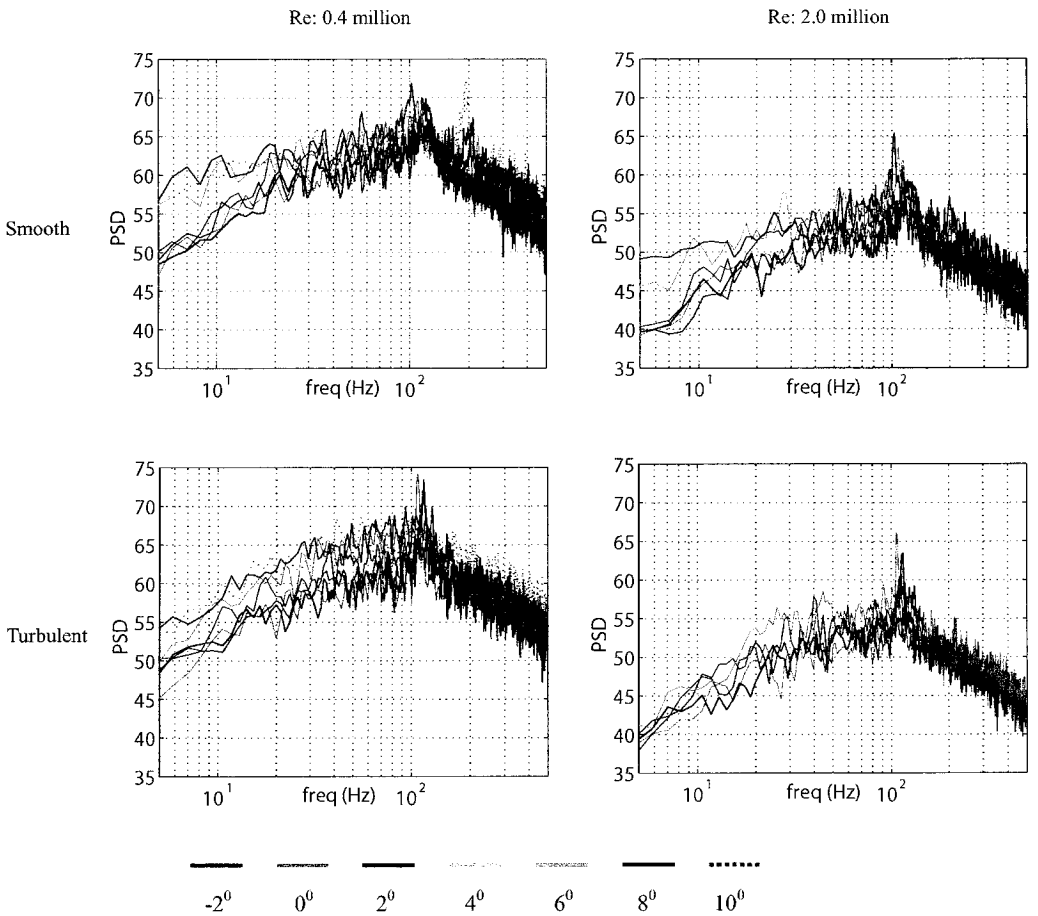

Figure 5.6: Power spectral densities of the hot-wire signal in wake of the prism, fineness of 3, large chamfer, smooth (top), turbulent (bottom), $Re : 0.4 \times 10^6$ (left), $Re : 2.0 \times 10^6$ (right).

5.3 Power spectral densities for a 4:1 prism

For a fineness ratio of 4 with square edges, the power spectral density shows the same trend in smooth flow for the two *Re* with a peak at 80 Hz to 90 Hz for all angles of attack except for 10° with a peak at 150 Hz. In turbulent flow, there is no peak related to a vortex-shedding frequency visible on the graphs (Figure 5.7).

With a small chamfer configuration presented on Figure 5.8, vortex shedding only appears in smooth flow at low *Re* with peaks at 80 Hz to 90 Hz for all angles of attack except for 10° with a peak at 150 Hz.

For large chamfer, Figure 5.9 shows a peak at 90 Hz to 110 Hz depending on the angle of attack except for the 10° at low *Re* in smooth flow that presents a peak at 170 Hz. Again, as mentioned for the 3:1 prism, increasing *Re* or turbulence intensity for large chamfer configuration did not help to mitigate the vortex shedding narrow-band peak.

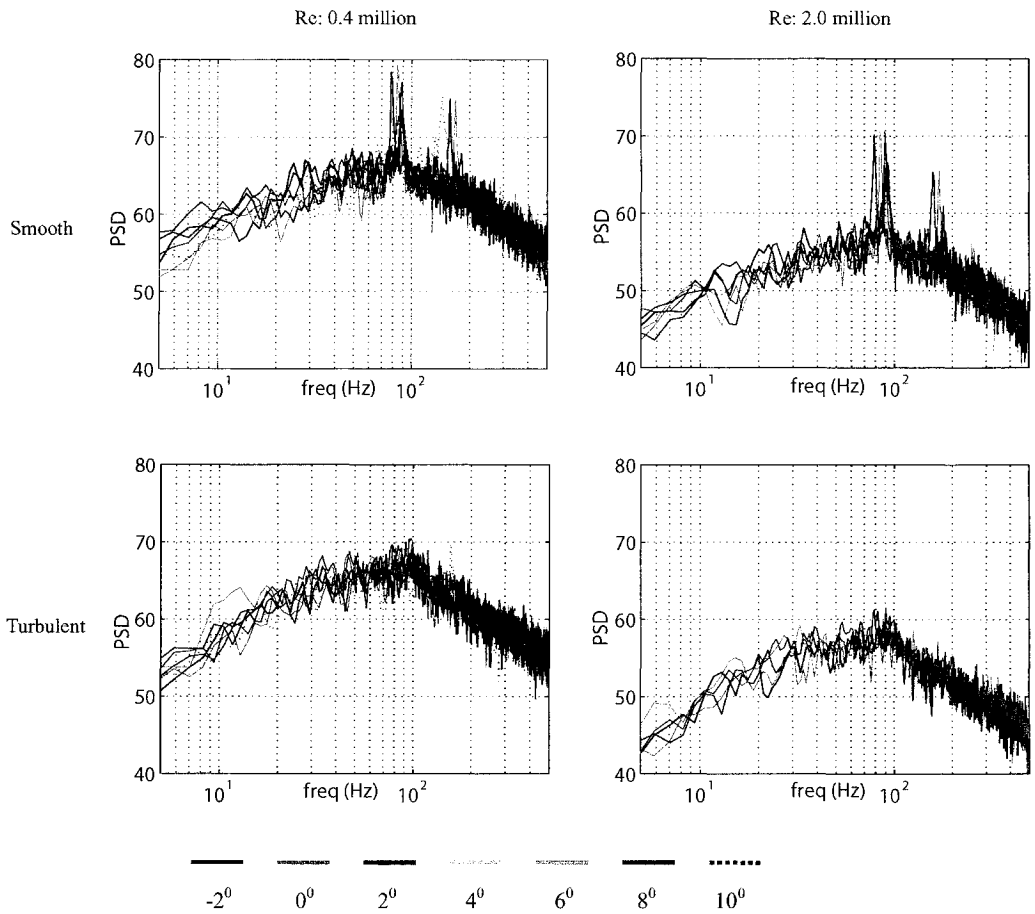

Figure 5.7: Power spectral densities of the hot-wire signal in wake of the prism, fineness of 4, square edges, smooth (top), turbulent (bottom), $Re : 0.4 \times 10^6$ (left), $Re : 2.0 \times 10^6$ (right).

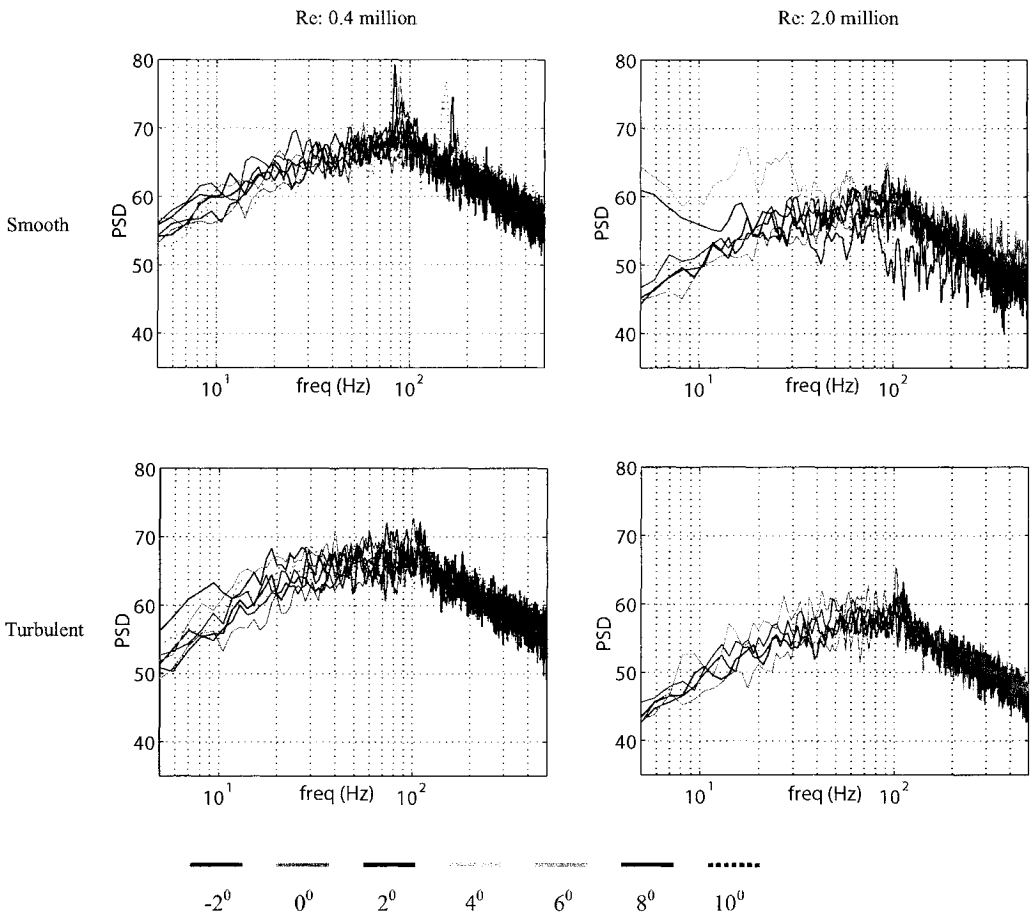

Figure 5.8: Power spectral densities of the hot-wire signal in wake of the prism, fineness of 4, small chamfer, smooth (top), turbulent (bottom), $Re : 0.4 \times 10^6$ (left), $Re : 2.0 \times 10^6$ (right).

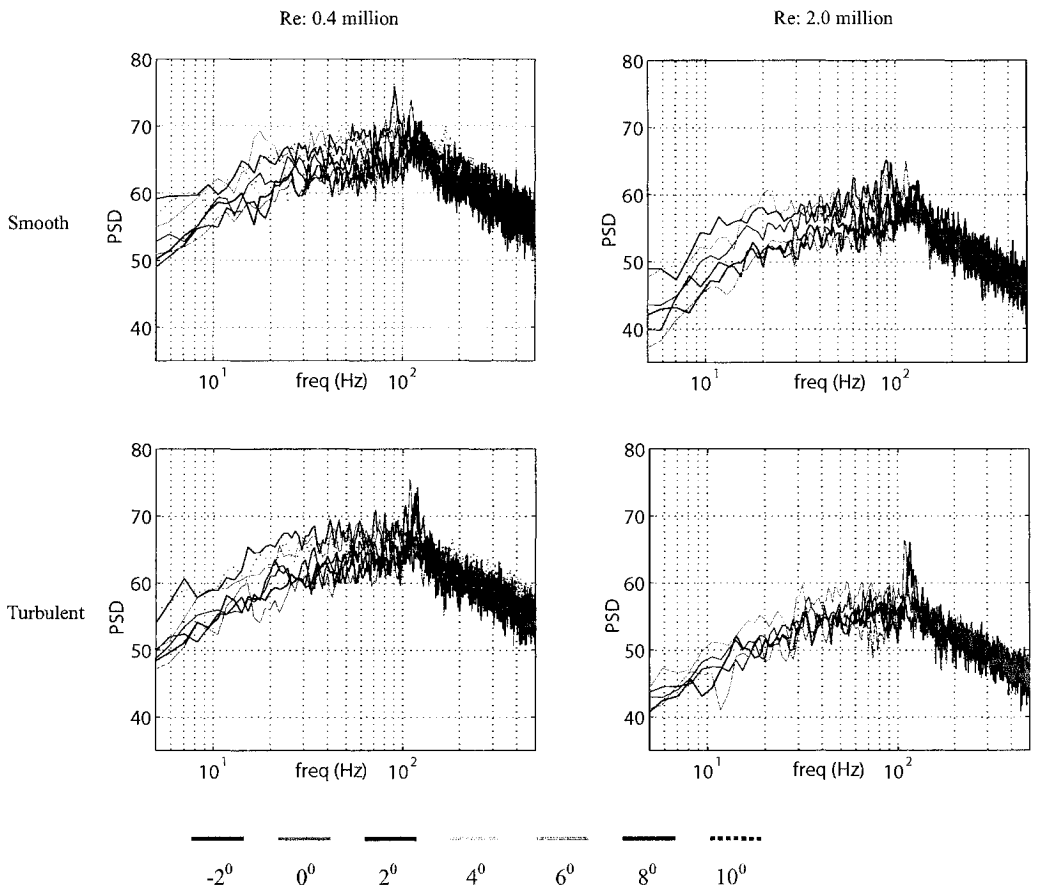

Figure 5.9: Power spectral densities of the hot-wire signal in wake of the prism, fineness of 4, large chamfer, smooth (top), turbulent (bottom), $Re : 0.4 \times 10^6$ (left), $Re : 2.0 \times 10^6$ (right).

Chapter 6

Interpretation and Analysis

6.1 C_D versus *fineness ratio*

One of the motivation to perform this study was the interrogation related to the Figure 5 and reproduced here (Figure 6.1) from Simiu and Scanlan [4] where C_D versus fineness ratio of a rectangular prism with square edges shows a grey zone between a fineness of 2 and 4. This figure was created from a compendium of many sources of data for this shape.

It was surprising to notice a non-unique value for C_D since it was believed or assumed that bluff bodies with sharp edges were not affected by *Re* variation having separated flow that will not have an influence on the aerodynamic force coefficients. However, the context for which these values where measured is not known and a full interpretation not possible.

On the other hand, the present study can add contribution to this graph and also help to understand the cause for the grey zone. Figure 6.2 presents results of the drag coefficient, for the 2:1, 3:1 and 4:1 prisms with square edges at Ma:0.15 for Reynolds number from 0.3×10^6 to 2.0×10^6 in smooth and turbulent flow. As it can be observed, there is not a

unique value for the drag coefficient C_D. To do a comparison with Figure 6.1, C_D presented in this section of this study was normalised using the depth of the prism instead of the width as for the other sections in the thesis.

For a 2:1 prism, the C_D varies from 1.35 to 1.5 in smooth flow and from 1.34 to 1.48 in turbulent flow with 5% longitudinal intensity of turbulence. For a 3:1 prism, the drag coefficient variation was 1.04 to 1.17 in smooth flow and 1.19 to 1.26 in turbulent flow. Finally, the 4:1 prism presents a C_D variation of 0.93 to 1.02 in smooth flow and 1.18 to 1.25 in turbulent flow.

A comparison of the results obtained from this study with Figure 6.1 shows a good agreement for the C_D value range for the 3:1 and 4:1 prisms. However, the 2:1 prism results from the present study is lower than the C_D values of Figure 6.1 by a factor of 1.17%.

Thus, Reynolds number as well as the turbulence intensity affect the drag coefficient. For tests done in smooth flow, the variation of C_D is higher for a small fineness ratio than larger one. Also, turbulence intensity tends to affect less the drag coefficient compare to the effects of Reynolds number in light of the data mentioned above.

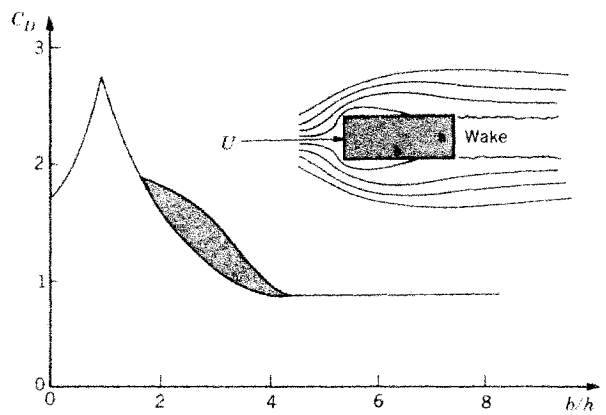

Figure 6.1: Drag coefficient versus fineness ratio b/h of rectangular prisms with square edges (after Simiu and Scanlan).

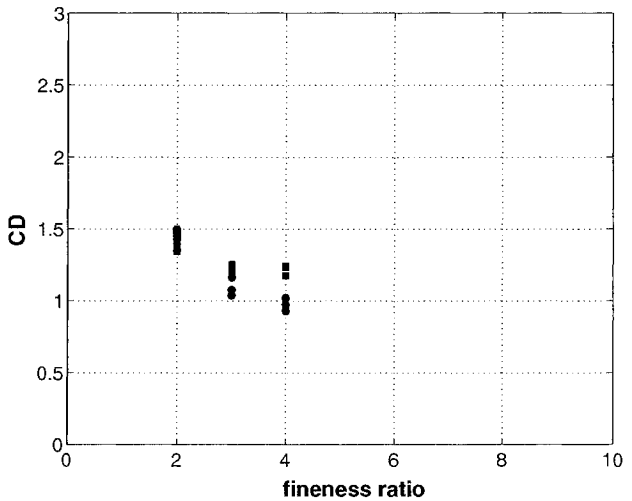

Figure 6.2: Drag coefficient versus fineness ratio for square-edge prisms, Reynolds numbers from $Re : 0.3 \times 10^6$ to $Re : 2.5 \times 10^6$, smooth (circle), turbulent (square).

6.2 C_D versus St

The Strouhal number St, is defined as the ratio of the inertia local force to the inertia convective force.

$$St = \frac{f_s D(\alpha)}{U} \tag{6.2.1}$$

where:

f_s: vortex-shedding frequency;

$D(\alpha)$: characteristic frontal dimension;

U: mean wind velocity.

This important similitude parameter has an application for unsteady flow that involves a characteristic frequency of oscillation f_s [1].

Vortices can be shed from the prism with different frequencies. Small vortices are shed with high frequency that leads to a high St and inversely, large vortices with low frequency implies a low St. On the other hand, smaller vortices shed behind the prism make the wake smaller and this is determinant for the drag coefficient magnitude C_D. A narrower wake means that the drag coefficient will be smaller.

Thus, there is a relationship between the Strouhal number St, and the drag force coefficient C_D. Theoretically, St and C_D should be inversely proportional; if small vortices with high frequency are shed in the wake of the prism, it will result in high St and a small C_D, with a narrow wake [15].

For constant characteristic dimensions D (depth) and W (width) of the prism at a given angle of attack, the frontal dimension seen by the airflow is calculated using Equation 6.2.2.

$$D(\alpha) = W|sin\alpha| + D|cos\alpha| \tag{6.2.2}$$

Considering a constant wind velocity U of 53 m/s corresponding to Ma of 0.15, the Strouhal number is directly related to the shedding frequency f_s. A summary of the expected shedding frequencies is presented in Table 6.1 based on Strouhal number of 0.08 for a 2:1 prism and 0.13 for a 3:1 and 4:1 prisms [16].

As it can be observed on Table 6.1, the theoretical shedding frequencies are underestimated for most of the angles of attack compared to the experimental shedding frequencies for the first harmonic. This situation is clear for the 3:1 prism and 4:1 prism with larger f_s from experimental results than from the theory. This suggests that the Srouhal number used to calculate the theoretical shedding frequency could have been underestimate and based on the experimental results, the Strouhal of a 3:1 fineness ratio prism with square edges was found to be 0.17 and for a 4:1 prism, the St was also 0.17.

Since the power spectral density computed from the hot-wire signal of a 2:1 prism in smooth flow was not representative of the vortex-shedding frequency given the original bad position of the hot-wire in the wake, an experimental value for Strouhal number has not been calculated.

	2 :1, square edges, smooth flow
Wind angle	**f_s th [Hz]**
-2^0	52
0^0	56
2^0	52
4^0	49
6^0	46
7^0	45
8^0	44
10^0	42

	3 :1, square edges, smooth flow		
Wind angle	**f_s th [Hz]**	**f_s exp [Hz] *Re* :0.4x10^6**	**f_s exp [Hz] *Re* :2.0x10^6**
-2^0	82	105	109
0^0	90	108	110
2^0	82	-	-
4^0	75	-	-
6^0	69	180	90, 180
7^0	67	Not measured	Not measured
8^0	64	170	85, 170
10^0	60	160	78, 160

	4 :1, square edges, smooth flow		
Wind angle	**f_s th [Hz]**	**f_s exp [Hz] *Re* :0.4x10^6**	**f_s exp [Hz] *Re* :2.0x10^6**
-2^0	79	89	90
0^0	90	88	91
2^0	79	90	91
4^0	71	90, 180	89, 180
6^0	64	85, 170	85-170
7^0	61	Not measured	Not measured
8^0	58	80, 160	80-160
10^0	54	143	Not measured

Table 6.1: Theoretical and experimental shedding frequencies f_s for three fineness ratios and eight angles of attack of rectangular prisms at Mach: 0.15, in smooth flow for two Reynolds numbers.

It is possible to analyse the relation between the C_D presented in Chapter 3 with the vortex-shedding frequency presented in Chapter 5.

The results for large chamfer in smooth and turbulent flow should decrease their vortex-shedding frequency with angle of attack since the drag coefficient increased for this case. As it was reported on Figure 5.3, the vortex-shedding frequency peak was clearly decreasing with angle of attack α in smooth flow for large chamfer.

For a 3:1 prism, a decreasing shedding frequency with higher angles of attack was observed for all edge configurations in smooth and turbulent flow. However, the turbulent flow at high Re of 2.0×10^6 mitigated the vortex shedding phenomenon with no peak visible on Figures 5.4, 5.5 and 5.6. Also, the second harmonic was present on almost all figures for angle of attack of 6°, 8° while at 10°, the only frequency peak visible is the one corresponding to the second harmonic.

Finally, the 4:1 prism with square edges shows a narrow-band peak at 80 Hz to 100 Hz in smooth flow with f_s decreasing with increasing angle of attack, while turbulent flow mitigates the vortex-shedding phenomenon. There is again a second harmonic that is present for angles of attack of 6° and 8° while at 10°, only the second harmonic was present. In turbulent flow, there was no more vortex-shedding phenomenon visible on Figure 5.7.

Regarding results for small chamfer and large chamfer, the turbulence did not mitigate the vortex shedding as it did for the square edges. There is still narrow-band peak frequency

on Figures 5.8 and 5.9. Again, vortex-shedding frequency f_s decreases with increasing angle of attack α.

In summary, turbulence tends to mitigate the vortex-shedding phenomenon for square edges prism regardless of the fineness ratio. Vortex-shedding frequency decreases with increasing angle of attack α consistent with an increase in C_D and a second harmonic was shown for angle of attack of 6°, 8° and 10° while most of the time only the second harmonic was present for 10° case.

6.3 Reynolds number and turbulence effects on bluff-body shapes with sharp edges

Bluff bodies with sharp edges are affected by Reynolds number variation as well as by the turbulence characteristics of the oncoming flow. The aerodynamic coefficients presented in this study have also shown to be affected by other parameters such as fineness ratio, and edge treatment.

6.3.1 Effects on the lift coefficient C_L

Defining the aerodynamic stability of a rectangular prism by a positive lift coefficient with a positive angle of attack of the prism, the stability condition of the prism can be reached by:

- Adding chamfers at the corners;
- increasing the fineness ratio;
- adding turbulence in the flow;
- increasing *Re* especially for a 2:1 prism with large chamfer.

As presented on Figure 6.3, *Re* variation has a significant effect on the lift slope at 0° for a 2:1 prism with large chamfer. This is the most important variation notice for the nine bluff body shapes tested, changing its aerodynamics from a potential for aerodynamic instability with a negative slope at 0° for *Re* of 0.4×10^6 to a positive slope for higher *Re*. However, it is believed that the *Re* has still a considerable impact on the other shapes investigated depending on the fineness ratio, the edge treatment and the angle of attack.

From Table 6.2, it is clear that the variation of *Re* in smooth flow varies with edge configuration, fineness ratio and angle of attack of the prism. For the *Re* range covered in this study, it seems that a 2:1 prism, regardless of the edge treatment is more affected than the other fineness ratios. There could be a range of *Re* for which a given fineness ratio is more affected.

As it can be observed in Table 6.2, the effect of *Re* is reduced in turbulent flow. There is still a significant ΔC_L for a 2:1 prism with square edges and large chamfer and 3:1 prisms with square edges for angles of attack of $-2°, 0°, 2°, 4°$ and $6°$ but for the other fineness ratios and edge configurations, the effect of *Re* is reduced at ΔC_L value under 10% in turbulent flow.

However, by comparison with the effect of turbulence on a 2:1 prism with square edges at *Re* around 10^4 [11], it can be observed on Figure 6.4 that an intensity of turbulence of 5% gives a C_L value around -0.4 at $6°$ while at high *Re*, the C_L is -0.2 at $6°$ (Figure 3.1).

This suggests that the level of intensity of turbulence requires to reduce the potential for aerodynamic instability is higher at 10^4 than at high *Re* (10^6) based on the results obtained in this study. A summary of the conditions where *Re* effects were observed is presented on Figure 6.5.

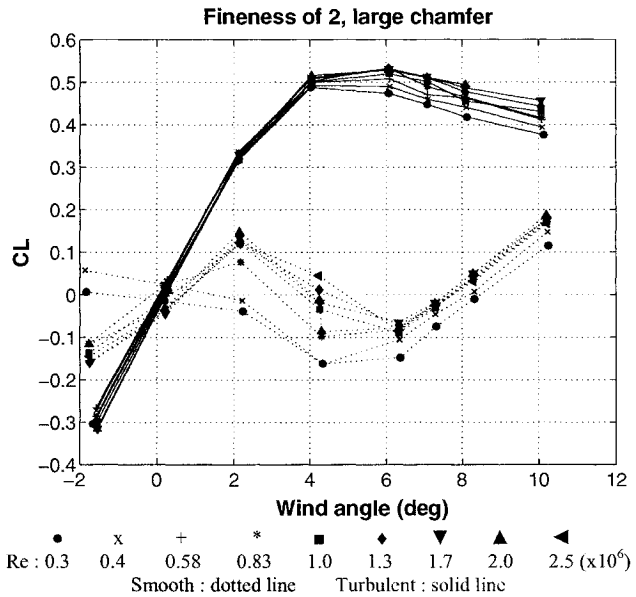

Figure 6.3: Lift coefficient versus wind angle for a prism with fineness of 2, large chamfer, for nine Reynolds numbers in smooth and turbulent flow.

C_L		*Re* effect in smooth flow					*Re* effect in turbulent flow				
		-2^0	0^0	2^0	4^0	6^0	-2^0	0^0	2^0	4^0	6^0
2 :1	**Square edges**	20	-	12	15	2	10	-	20	19	17
	Small chamfer	120	-	66	28	52	-	-	-	-	-
	Large chamfer	200	-	200	200	115	18	-	6	5	13
3 :1	**Square edges**	10	-	21	44	40	22	-	19	20	16
	Small chamfer	52	-	28	86	26	3	-	6	7	12
	Large chamfer	8	-	6	3	10	6	-	6	3	3
4 :1	**Square edges**	10	-	5	25	20	7	-	2	2	4
	Small chamfer	2	-	3	3	4	3	-	4	5	3
	Large chamfer	5	-	1	1	6	4	-	8	4	3

Table 6.2: Summary of the percent variation of the lift coefficient normalised by the smallest C_L with Reynolds number from $Re : 0.3 \times 10^6$ to 2.0×10^6 for different angles of attack of the prism.

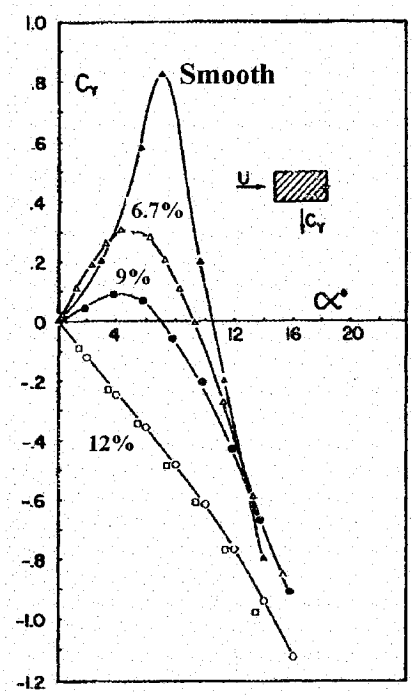

Figure 6.4: Lift coefficient (positive downward) as function of the angle of attack of the prism α for Re of $10^3 - 10^4$ at four levels of turbulence intensity (after Laneville, Gartshore and Parkinson, 1971).

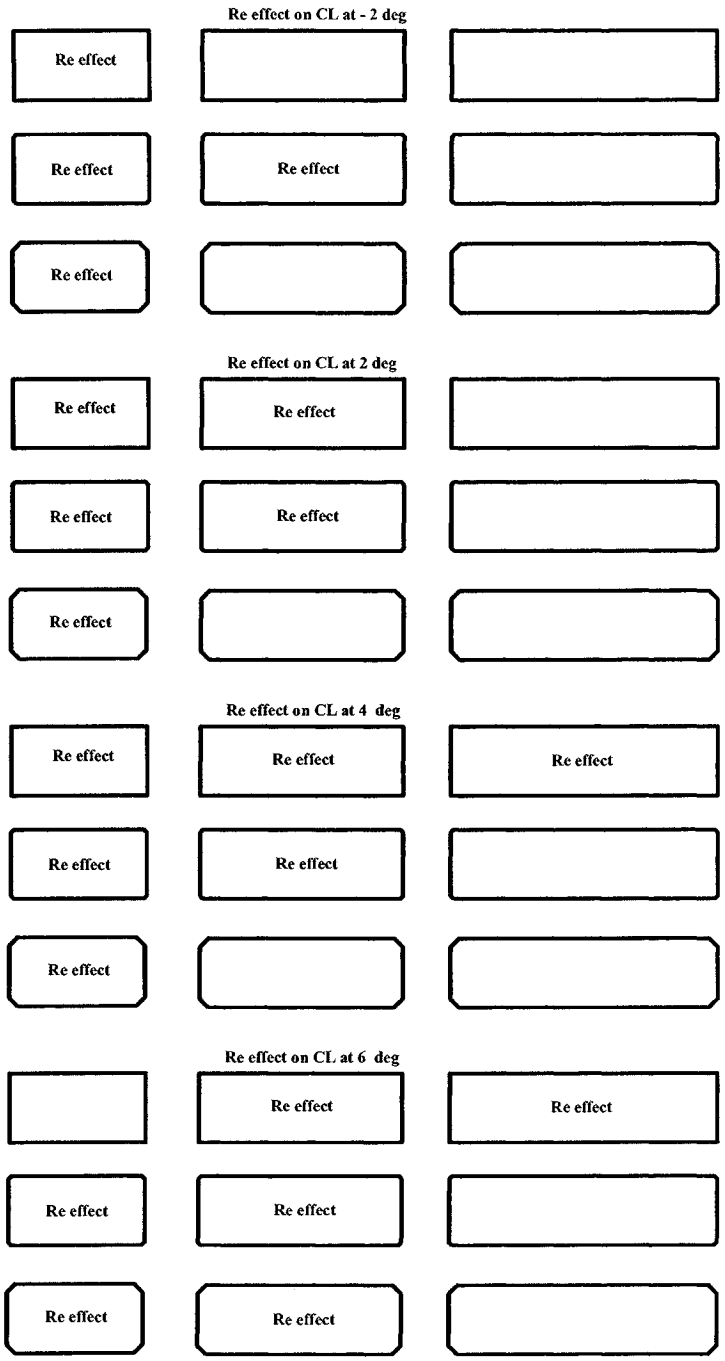

Figure 6.5: Reynolds number effect over 10% on the lift coefficient value C_L for different angles of attack of the prism, in smooth flow.

6.3.2 Effects on the drag coefficient C_D

Defining the stability of the drag coefficient as a positive parabola at 0°, the drag coefficient as shown to decrease its magnitude by:

- Adding chamfers at the corners;
- increasing the fineness ratio;
- reducing the turbulence in the flow with the exception of a 2:1 prism with square edges at $-2°$, 0° and 2°, and for small chamfer at $-2°$ to 6°;

The drag coefficient has shown clearly less variation with *Re* compared to the lift coefficient C_L for the Reynolds number range covered. From Table 6.3, the largest difference appears to be in smooth flow. There is no clear pattern of *Re* effect on C_D regarding the angle of attack parameter.

Adding chamfer or increasing the fineness ratio appeared to reduce the suction for the second half of the width of the prism and this was translated in a smaller width of the wake behind the prism corresponding to a lower drag coefficient.

The state of the boundary layer could also be the reason for variation of the drag coefficient C_D with *Re*. The development of the boundary layer at the surface of the prism is affected by the presence of the chamfer that could trip the flow and changes the state of the boundary layer from laminar to turbulent. This will allow the flow to stay attached longer to the body before separation, or at least, causing a variation of the relative speed of the flow near the surface of the prism at the separation point defined by sharp edges.

However, the drag coefficient is affected by the turbulence intensity of the oncoming flow, the turbulence having the effect to increase the drag magnitude for all the prisms tested with the exception of a 2:1 prism at $-2°$, $0°$ and $2°$ for square edges and for a 2:1 with small chamfer at all angles of attack tested.

Since the drag force at $0°$ angle of attack is the summation of the forces acting at the leading edge with the forces from negative pressures acting at the trailing edge, it would have been expected that the drag would decrease with turbulence knowing that the suction close to the trailing edge of the prism tends to reduce with turbulence, suggesting a smaller wake and higher base pressure.

However, the presence of the chamfer modifies the contribution of the leading and trailing edges drag pressure by taking into account the along-wind component of the C_P that develops on the chamfer. It was observed on Figures 4.1, 4.2 and 4.3 that the suction on the chamfers is larger in turbulent flow than in smooth flow which could be a reason for the increase of C_D with turbulence.

On the other hand, it appears that by increasing the fineness ratio and adding turbulence, the drag coefficient also increases at Re of 10^6 while at lower Re the opposite situation occurs. This could be interpreted as a Re effect, for a range of 10^4 to 10^6, on the effect of turbulence on rectangular prisms with sharp edges, i.e. the way the turbulence affects the aerodynamics of rectangular prisms is affected by Reynolds number.

The 2:1 prisms with square edges and small chamfer are the only prism configurations that have shown a negative parabola at 0°. When adding turbulence, this parabola becomes positive and the value of C_D at 0° is smaller in turbulent flow than in smooth flow as observed by Courchesne and Laneville [12] at lower Re (10^4).

C_D		***Re* effect in smooth flow**					***Re* effect in turbulent flow**				
		-2^0	**0^0**	**2^0**	**4^0**	**6^0**	**-2^0**	**0^0**	**2^0**	**4^0**	**6^0**
2 :1	**Square edges**	11	11	11	11	11	6	4	4	5	6
	Small chamfer	10	17	10	7	10	-	-	-	-	-
	Large chamfer	6	4	4	5	4	9	10	9	9	7
3 :1	**Square edges**	8	12	10	10	11	7	8	6	4	5
	Small chamfer	6	8	6	7	9	5	2	2	3	2
	Large chamfer	11	11	11	11	6	7	7	7	7	4
4 :1	**Square edges**	10	11	10	11	10	6	6	5	5	5
	Small chamfer	9	15	11	10	8	6	5	4	4	3
	Large chamfer	8	10	8	7	5	7	8	7	4	4

Table 6.3: Summary of the percent variation of the drag coefficient normalised by the smallest C_D with Reynolds number from $Re : 0.3 \times 10^6$ to 2.0×10^6 for different angles of attack of the prism.

6.3.3 Effects on the pitching moment coefficient C_M

Defining a positive slope of the pitching moment coefficient as a positive C_M for positive angle of attack of the prism α, the slopes of the pitching moment coefficient have shown to increase with:

- Adding chamfers at the corners (very important effect);
- increasing the fineness ratio;
- adding turbulence to the flow.

6.3.4 Effects on the steady surface pressure coefficient C_P

The distributions of the mean pressure coefficient C_P on a chord-wise strip at the centreline of the prisms and for an angle of attack of 0° have shown:

- to have the same shape for the different fineness ratios for the same corresponding width but more suction was present for the lower fineness ratio;
- to have a reduced suction for the second half of the prism width when chamfers are added to the prisms;
- to have a reduced suction for the second half of the prism width while increasing the suction for the first half by adding turbulence to the flow ;
- to have a reduced suction for the second half of the prism width by increasing Reynolds number from 0.4×10^6 to 2.0×10^6 especially for a 2:1 prism in smooth flow with small and large chamfer and for a 3:1 prism with small chamfer in smooth flow;
- to be different when turbulence is added to the flow compared to when only Re is increased.

The pressure distribution along the centreline of the prisms have the same shape for the three fineness ratios investigated. However, there are two major differences. First, the pressure distribution continue to develop on the top and bottom surfaces for a longer width of the prism as the fineness ratio is increased and secondly, the pressure distribution at the top and bottom of the cross-section have the same magnitude at 0° for the first 2/3 width of the 3:1 prism and the first half of the 4:1 prism (Figure 6.6). However, for the pressure

distribution at 6°, it was clearly observed that the pressure distribution was modified by the fineness ratio. The suction at the top surface of the prism increases with increasing fineness ratio while the suction at the bottom of the prism is reduced with the fineness ratio up to a point where there is positive pressure for the 4:1 prism (Figure 6.7). This means that the flow is affected by the fineness ratio and adjustment of the mean pressure coefficient levels occurs as a function of the after-body length.

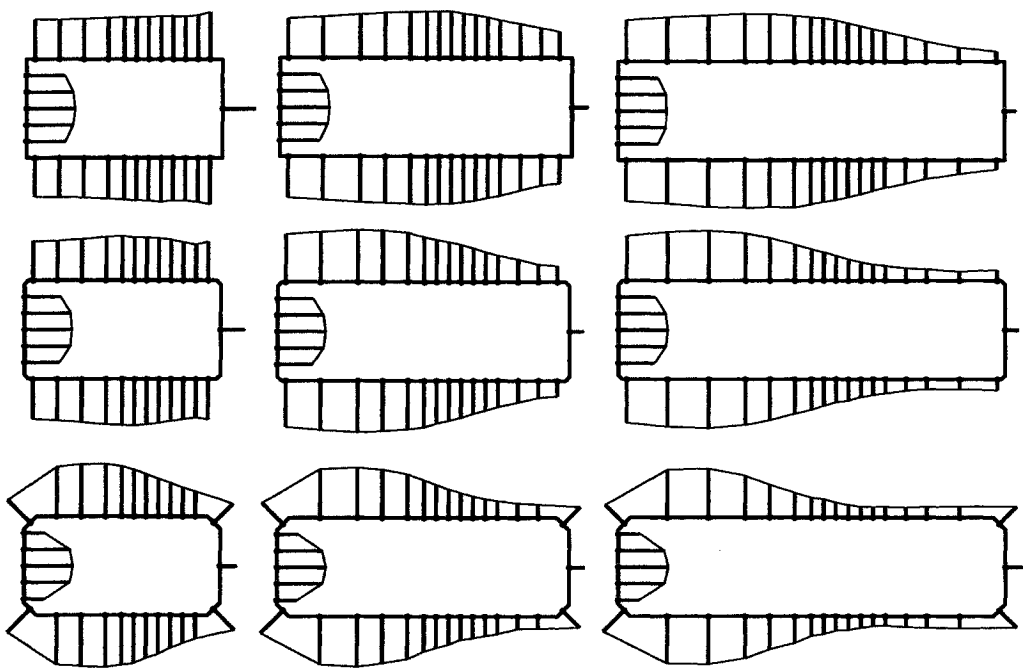

Figure 6.6: Effect of the fineness ratio on the distribution of mean pressure C_P for rectangular prisms at 0°, in smooth flow.

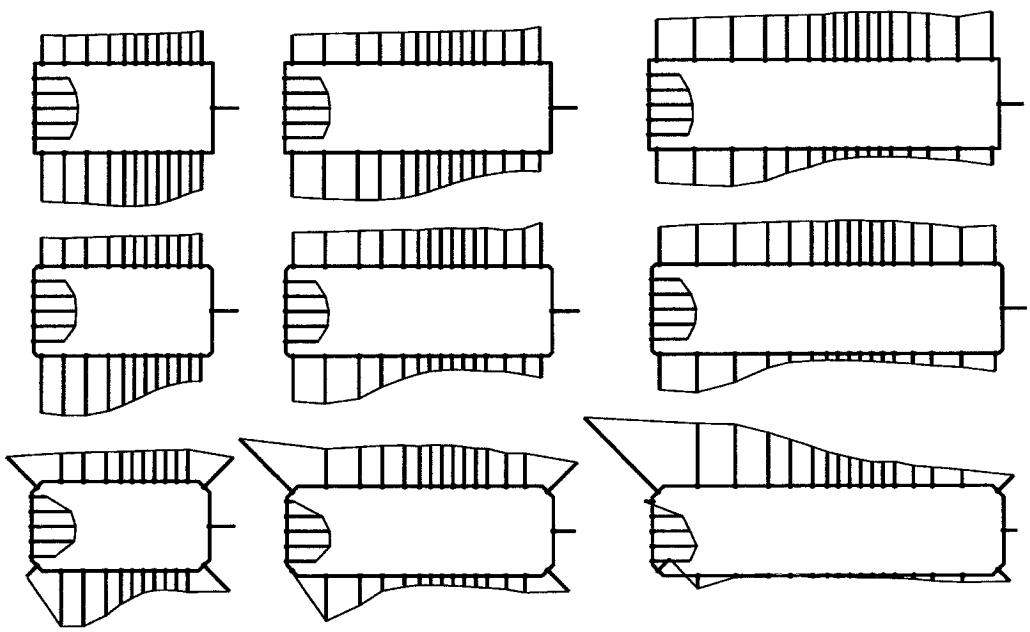

Figure 6.7: Effect of the fineness ratio on the distribution of mean pressure C_P for rectangular prisms at 6°, in smooth flow.

When chamfers are added to the edges of the prisms, the suction reduced for the second half of the width of the prisms while the first half did not show a C_P variation (Figure 6.6). This is directly related to the separated shear layer that is formed at the chamfer location and that is affected by the position of the two sharp edges instead of only one for square edges. The shear layer might have separated earlier for prisms with chamfers and also the separation might have occurred from a turbulent boundary layer state instead of a laminar state, giving more energy to the flow and allowing more possibility for reattachment or at least for a reduction of the suction for the second half of the prism top and bottom surfaces.

Turbulence in the oncoming flow presents approximatively the same trend for the pressure distribution than adding chamfers to the prisms. However, as the suction at the second half of the width of the prism is reduced, the first part of the separated shear layer sees an increase in negative pressure (suction) and is acting on a smaller distance than in smooth flow (Figure 6.8). Thus, the first part of the separated shear layer is characterised by strong suction and by a possible reattachment point at the surfaces of the prism.

Finally, the effect of increasing *Re* on the mean surface pressure distribution on chordwise strip of the prisms has an impact comparable to increasing turbulence or adding chamfer. This can be observed especially for prisms with 2:1 fineness ratio with small and large chamfer (Figure 4.1) and for 3:1 fineness ratio with small chamfer at 0° angle of attack (Figure 4.2). The pressure distribution of Figure 6.9 suggests that the length for which higher suction took place is reduced with increasing *Re* from 0.4×10^6 to 2.0×10^6.

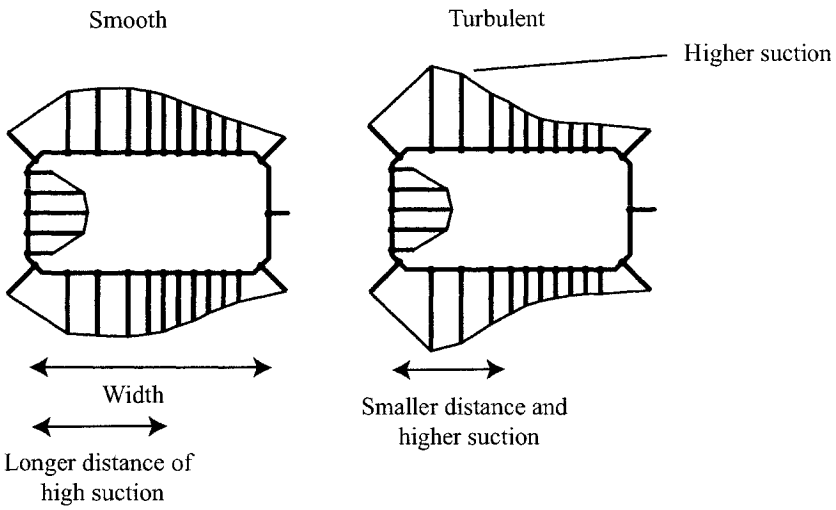

Figure 6.8: Effect of the turbulence on rectangular prisms in smooth and turbulent flow.

However, it was observed that an increase in *Re* was not equivalent to an increase of turbulence up to 5% since the pressure distribution were not the same. There is higher suction in turbulent flow and the distance for which higher suction took place appears to be considerably reduced in turbulent flow when compared to high *Re* case. This suggests that increasing the turbulence intensity at *Re* of 10^6 does not have the same effect on the pressure distribution than increasing the *Re* from 0.4×10^6 to 2.0×10^6. Thus, the aerodynamic forces will be affected differently depending on *Re* regime and the level of turbulence intensity.

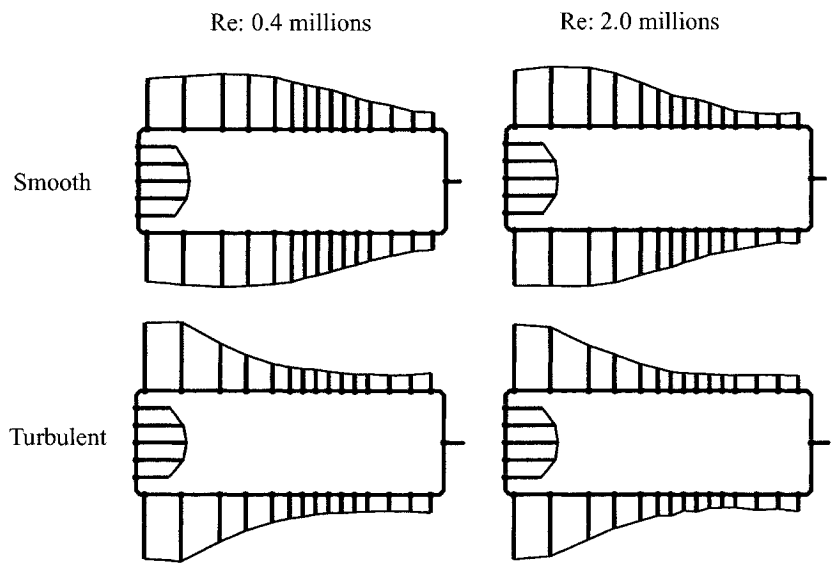

Figure 6.9: Effect of the turbulence and Reynolds number on rectangular prisms.

6.3.5 Discussion

In light of the above, it can be concluded that, for wind-tunnel tests done at *Re* of 10^4 on rectangular prisms with sharp edges, results will be different than those obtained from tests done at *Re* of 10^6. In fact, doing tests at lower *Re* in smooth flow gave different results for both C_L and C_D for 2:1 and 3:1 fineness ratio prisms regardless of the edge configuration and for the 4:1 prism with square edges.

However, by performing wind-tunnel tests in turbulent flow at *Re* of 10^4, the lift coefficient will be different than the one obtained at high *Re* for the 2:1 prism regardless of the edge configuration and for the 3:1 prism with square edges. On the other hand, the effect of *Re* on the turbulence will give different result for the drag coefficient for the 2:1 prism with large chamfer and for the 3:1 and 4:1 prisms regardless of their edge configurations (Figure 6.10).

Combining the effect of *Re* on C_L for particular rectangular prisms with the effect of the *Re* on the turbulence effect on the C_D for other rectangular shapes, tests should be done when possible at higher *Re* (as close as the one in real life) to obtain significant results for structure having rectangular shapes with sharp edges. If this is not possible to achieve, a safety factor should be applied to results obtained at lower *Re* based on the results obtained in this study at high *Re*.

As described by Davenport [21], wind has an effect on structures but this effect varies with different parameters. The concept of wind loading chain provides a reliable framework

to evaluate the final wind force acting on a structure after considering a safety coefficient for each parameter involved in the wind loading chain. One of these parameters is the modelling uncertainty [21]. Performing tests in wind tunnel at low *Re* when the structure in real life will face high *Re* is one example that could be classified in this category. Results obtained at high *Re* in this study will help to evaluate with higher confidence level a safety factor to apply in the wind loading chain when considering test done at low *Re* on rectangular prisms with sharp edges.

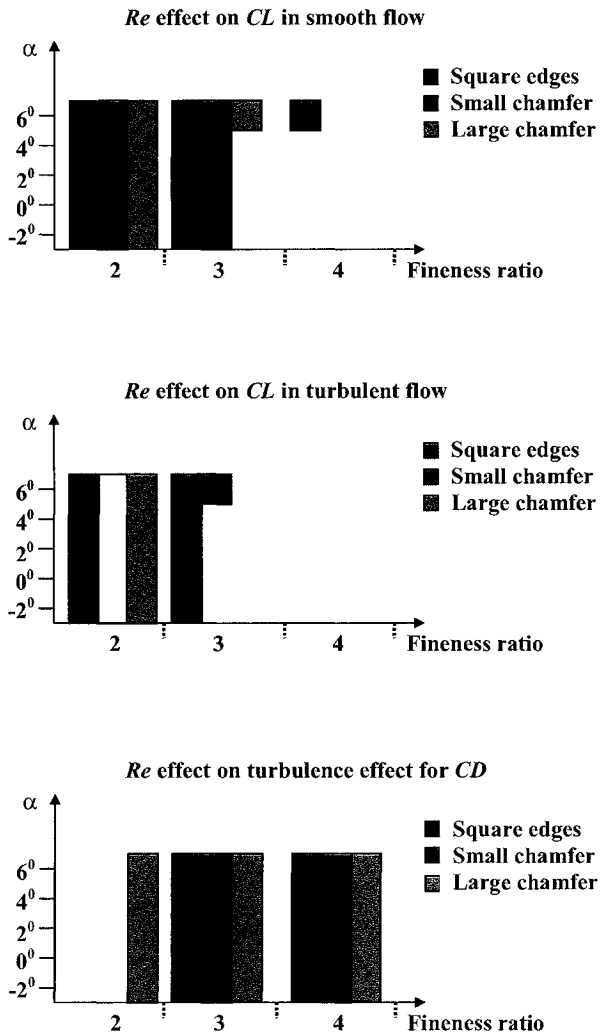

Figure 6.10: *Re* effect on the lift coefficient C_L, depending on fineness ratio, edge configuration and angle of attack, in smooth and turbulent flow.

Conclusion

The main objective of this research was to investigate the Reynolds number effect on the aerodynamic coefficients for rectangular prisms with sharp edges, for fineness ratios of 2, 3 and 4 and, for a range of Re from 0.3×10^6 to 2.0×10^6. The following conclusions and recommendations can be pointed out from this study.

Lift coefficient

The lift coefficient was found to be affected differently by a variation of Re depending on the edge configuration, fineness ratio, angle of attack and flow turbulence.

In smooth flow, the main findings are:

- The 2:1 prisms were the most affected by Re variation for most of the angles of attack from $-2°$ to $6°$. Increasing chamfers gave the largest variation of C_L with Re. At angles of attack of $-2°$, $2°$ and $8°$, C_L changed sign(+/-) for large chamfer with increasing Re.
- The 3:1 prisms were affected by Re variation for all the angles of attack investigated for square edges and small chamfer while for large chamfer, the Re effect was shifted to higher angles of attack.
- The 4:1 prisms were affected by Re variation only for square edges at higher α while the small and large chamfer configurations did not show significant variation with Re for angle of attack from $-2°$ to $6°$.

- Potential for aerodynamic instability was reduced by increasing the fineness ratio and/or by adding chamfers.
- *Re* effects were shifted to higher angle of attack by increasing fineness ratio and/or by adding chamfers.

In turbulent flow (I_u: 5%), the main findings are:

- The 2:1 prisms were affected by *Re* for square edges and large chamfer. At angle of attack of 10°, C_L changed sign(+/-) for square edges.
- The 3:1 prisms were affected by *Re* for the square edge configuration for angles of attack from $-2°$ to 10°.
- The effects of *Re* were less important in turbulent flow for a 4:1 prism regardless of the edge configuration tested.

Drag coefficient

The drag coefficient was affected by *Re*. However, the magnitude of this effect was less important than what was observed for C_L.

In smooth flow, the main findings are:

- The drag coefficient have shown a variation with *Re*, with an increase from *Re* of 0.3×10^6 to 1.0×10^6 and a plateau thereafter for the 2:1 prisms.

In turbulent flow (I_u: 5%), the main findings are:

- The drag coefficient increased with turbulence for the 2:1 prism with large chamfer and for the 3:1 and 4:1 prisms regardless of the edge

configuration, for angles of attack from $-2°$ to $6°$. This suggests that performing tests in smooth flow at high *Re* can underestimate the aerodynamic drag force experienced by a bluff-body with sharp edges.

- The drag coefficient decreased with turbulence for the 2:1 prism with square edges for angle of attack of $-2°$, $0°$ and $2°$ and small chamfer for $-2°$ to $6°$.
- Reynolds number had an effect on the effect of turbulence on the rectangular prisms of this study.

Surface pressure coefficient

The surface pressure coefficient C_P has shown different pressure field distribution for a chord-wise strip at the centreline of the prism depending on steady or unsteady measurements.

For steady surface pressure measurements, the main findings are:

- Adding turbulence intensity or increasing *Re* helps to curve the separated shear layer towards the body and increases its tendency to reattach.
- Turbulence intensity involves more suction for the first part of the separated shear layer in comparison with smooth flow and in comparison with increasing *Re* from 0.4×10^6 to 2.0×10^6.
- The surface pressure distribution was not clearly affected by a variation of *Re* in turbulent flow at $0°$.
- Reattachment was observed only for 4:1 fineness ratio prisms, at high angle of attack and for prisms with chamfers.

For unsteady surface pressure measurements, the main findings are:

- Fluctuating reattachment was observed for 2:1 fineness ratio prisms.

- Frequency of fluctuating reattachment was higher for larger fineness ratio prisms.
- Flapping shear layer combined with high frequency surface pressure fluctuations travelling across the prism towards the trailing edge are responsible for fluctuating reattachment.

General conclusions

- The results from this study represent, to the author's knowledge, the only data available for rectangular prisms at high Reynolds number, in turbulent flow and for incompressible flow regime.
- With regards to potential aerodynamic instability such as galloping, turbulence increases the aerodynamic stability of rectangular prisms and the level of turbulence required to reach a stable state is less at high *Re* (10^6) than at low *Re* (10^4).
- Conducting wind tunnel tests at low Reynolds number in turbulent flow overestimate the lift coefficient and its variation with angle of wind incidence and can underestimate the drag coefficient of the rectangular prisms tested, except for the drag of a 2:1 prism with square edges.
- For a given turbulence intensity in a wind tunnel that is representative of the higher frequencies of a wind spectrum in real life (natural wind), the pressure field distribution that develops around the bluff body is different than the one obtained by increasing the *Re* from 0.4×10^6 to 2.0×10^6.
- State of the boundary layer before and during separation process is believed to have an influence on flow development around the prisms and ultimately on the aerodynamic coefficients.
- Relaxing the *Re* might be the cause of systematic errors for wind-tunnel experiments on bluff bodies with sharp edges.

Recommendations

- Results obtained for the *Re* of this study (0.3×10^6 to 2.0×10^6) should be compared to results for the same geometry at lower *Re* to see if there are a *Re* effects between 10^3-10^5 and the results at 10^6. It is believed that all rectangular prisms will be affected by *Re* variation but for different range of *Re* and this range could be shifted to lower value for larger fineness ratio prisms.
- Tests should be done at different turbulence intensities for the same range of *Re* investigated in this study to see the effect of the turbulence at high *Re* and be compared to results at lower *Re* of 10^3-10^5.
- A comparison of the results obtained at *Ma*:0.15 in this study should be done with results at *Ma* of 0.075 and *Ma* of 0.3 measured during this research to see if there are compressible effects below *Ma*:0.3.
- Since the lift coefficient is affected by *Re* variation and the drag coefficient is affected by *Re* effect on the turbulence effect on rectangular prisms in an additional way, tests in wind tunnel on bluff bodies should be done at a *Re* at least of 10^6 and in turbulent flow, especially for 2:1 prisms which have shown the highest *Re* effect. If this is not possible to achieve, a safety factor should be applied to results obtained at lower *Re* based on the results presented here at *Re* of 10^6.

Appendix A

Comparison of methods of evaluation of transfer functions for tubing frequency response

In order to measure surface pressure on a model, small holes (pressure taps) typically with a diameter of 1.5-2.0 mm, are drilled through the model skin or walls, and metallic inserts are fitted into the holes and vinyl tubes are used to link these inserts to a pressure transducer. A tubing system becomes a necessity when an electronic pressure scanner (*EPS*) is used permitting the pressure taps to reach the scanner directly within the model (Figure A.1). Another option could be to use an individual high frequency response pressure transducer (e.g. Kulite) at each pressure tap location but, this technique would be expensive since many transducers would be needed and their fragility along with the glue used to fix them to the surface of the model would make it hard to reuse it for other tests.

Thus, tubing systems are part of all major tests involving surface pressure measurement since they represent an excellent compromise between accuracy and cost. However, reducing the cost of the experiments can introduce a distortion in the pressure signal due to tubing frequency response itself if long tubes are used. Consequently, the signal read by the

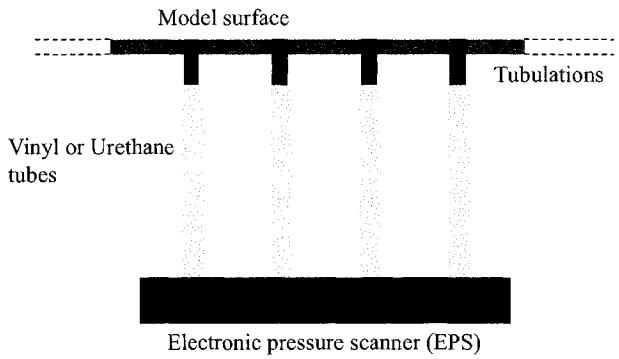

Figure A.1: General view of typical model surface with pressure tap system (Tubulations, tubes and EPS).

electronic pressure scanners (e.g. ZOC, Scanivalve Inc.) need to be corrected to remove the distortion of the tube and to obtain the real pressure signal acting at the model surface.

To correct for the undesirable effect, the transfer function of the tubes used for the test can be measured by sending a known signal to a given tube and also to a reference high frequency response pressure transducer (e.g. Kulite). The ratio of the two response signals in the frequency domain, normalized by the value at 0 Hz gives the transfer function that represents the signal amplification due to the tube.

Usually, the input signal is a white noise for which all frequencies are excited at the same time. This signal is created by an electronic signal sent to a horn driver system. The drum inside the horn driver is excited by the electronic signal and starts to vibrate and to create at the same time a pressure gradient inside the horn driver that can be read by the reference pressure transducer and by the tube connected to its pressure transducer installed on the horn driver cap (Figures A.2 and A.3).

The signal read by the reference pressure transducer and the EPS pressure transducer at the end of the tube are send to a spectrum analyzer. The latter takes data during a short period of time that depends on the frequency range and repeated it 100 times to compute the ratio of the two signals that represents the transfer function of the tube in frequency domain.

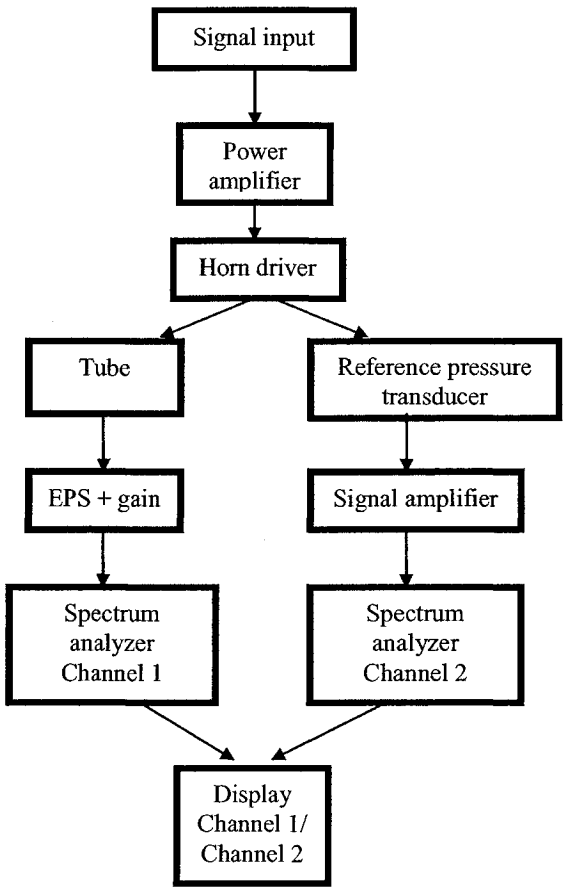

Figure A.2: Schema of the transfer function system measurement.

However, it is not guaranteed that each frequency of the white noise is excited during the same amount of time while the spectrum analyzer takes data. If not, it could affect the transfer function since some frequencies may need time to be sufficiently excited to reach

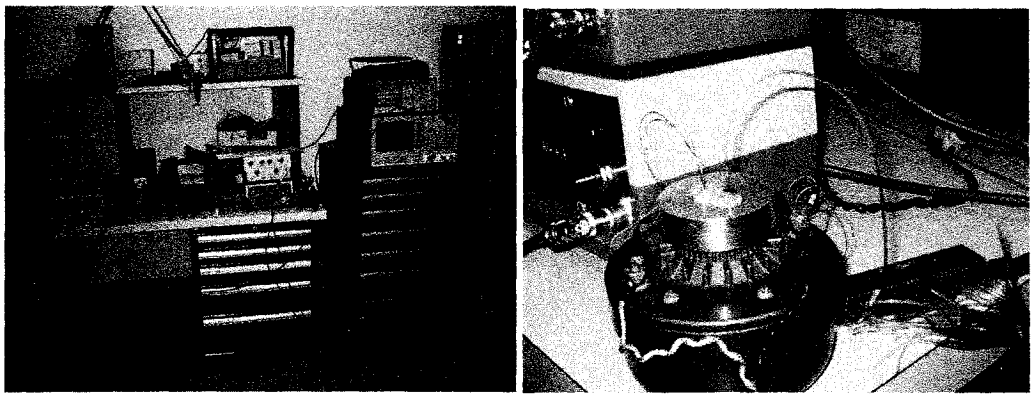

Figure A.3: Picture of the set-up instruments to measure the tubing transfer function.

a stationary state with a maximum amplitude response.

Thus, a verification of this technique was done by using another input signal: a swept sine function, that excites each frequency for a given number of cycles that permits to reach a stable signal. It follows that the lowest frequency will be excited longer than the highest one. A spectrum analyzer with a swept sine function was used to generate a sine wave as signal input. The transfer function was directly computed by the spectrum analyzer from the output of the two signals of the reference transducer and the tube with the EPS. This input sine wave signal has been compared to the white noise signal by looking at resulting transfer functions.

It appears that when a minimum of cycles around 10 were computed and a maximum amplitude voltage of 0.5 Volts for the electronic input signal was sent to the horn driver, the transfer function computed by the spectrum analyzer was similar to the one obtained from a white noise input signal. Under 10 cycles, the trend of the signal was the same but there were spurious peaks for some frequencies that required more cycles to process an accurate

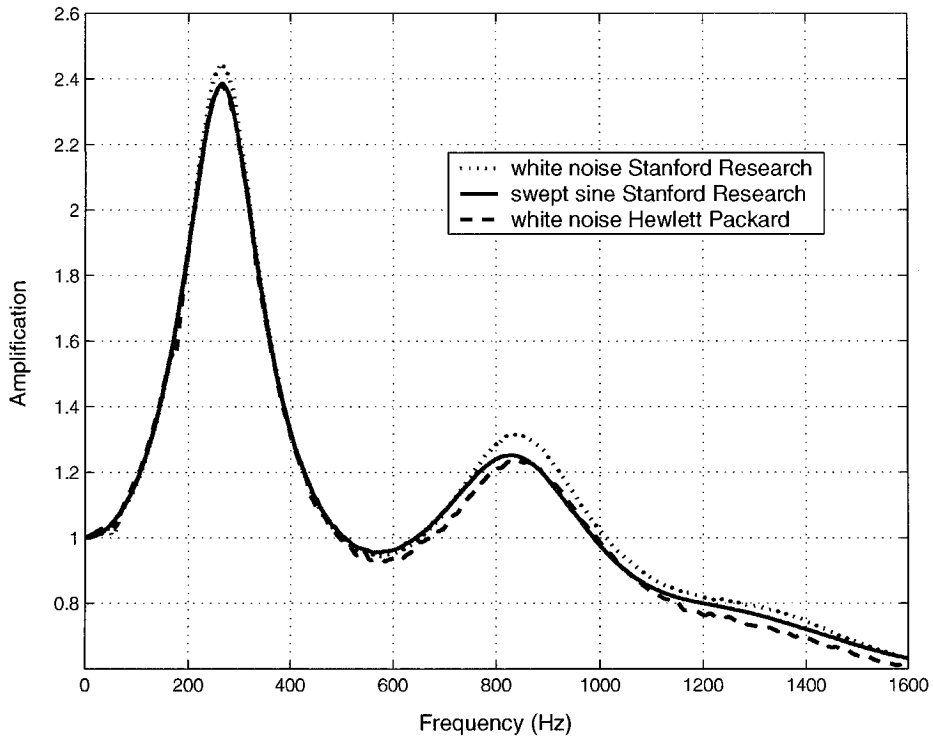

Figure A.4: Comparison of the transfer functions for different input excitation signals.

value for a given frequency. On the other hand, the maximum voltage is a characteristic that is limited by the reference transducer and pressure transducer reading capacities. Figure A.4 shows the two normalized transfer functions obtained from a Stanford Research Spectrum spectral analyzer and a transfer function of a white noise input signal performed with a Hewlett-Packard spectrum analyzer.

The most important point is that for the same spectrum analyzer to which two different input signals are compared with a reference pressure transducer (Kulite), both give transfer functions for the tubing frequency response that are comparable. A minor difference is observed at position where tubing amplification took place. However, for this study, it represented only 2.8% for the first amplification at 265 Hz and 5.6% at 840 Hz as shown

on Figure A.4. These discrepancies could be attributed to the different precision of the two spectrum analyzers and constitutes an indication of the error margin of this experimental technique.

Thus, this experiment proved that a white noise signal, for which all frequencies are excited at the same time, gives enough energy at each frequency to reach its maximum amplitude as a swept sine does by exciting each frequency separately, one at a time.

Appendix B

Evaluation of the bi-dimensionality of the flow

In this study, it was assumed that the cross-sectional aerodynamic forces and moments measured on the prisms of finite length were representative of the cross-sectional forces and moments on prism of infinite length. This assumption is true when the presence of the model in the test section will induced mean flow fluctuations in the along wind and vertical directions and negligible variations in the lateral direction. If this is the case, the flow field can be described as bi-dimensional (2D). If there are significant variations of the flow field in the lateral direction, the flow conditions are described as being tri-dimensional (3D).

2D flow conditions were ensure during the tests of this study by mean of a suction system integrated in the side walls of the test section at both extremities of the prism. The system permitted to do a suction of the boundary layer that develops on the walls and that affects the direction of the streamlines at the prism location. The suction system allowed a reduction of the normal velocity U_{normal} (Figure B.1). For this study, the suction ratio of the normal velocity U_{normal} to the mean velocity U was set to 0.0084 based on previous

tests carried out on bluff bodies in the 2D insert of the 1.5m x 1.5m Trisonic Blowdown Wind Tunnel. With a suction of 0.0084, the streamlines were parallel to each other at 0°.

This appendix presents an evaluation of the level of bi-dimensionality of the flow for the experiments of this study.

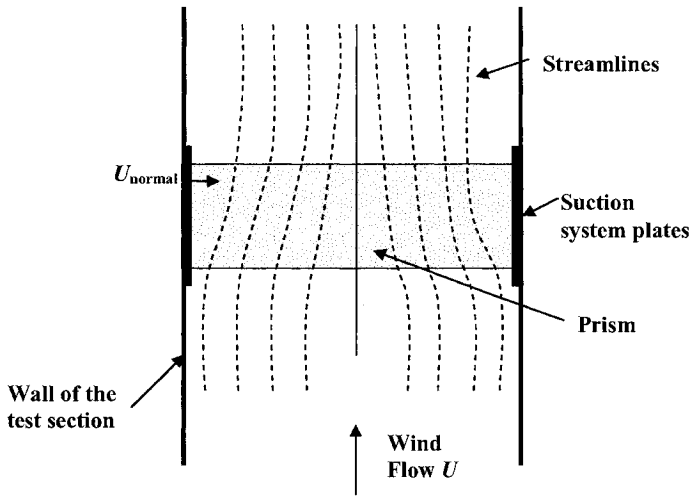

Figure B.1: Top view of the test section with streamlines, mean velocity U and normal velocity U_{normal} for definition of the suction ratio.

B.1 Base pressure measurements

To verify the 2D flow configuration during the tests, a second chord-wise strip of surface pressure could have been used at another spanwise location of the prism and be compared with the surface pressure distribution at the centre, but it was decided that two pressure taps at the trailing edge of the prism for two other locations than the centre will give enough information regarding the similarity of the cross-flow on the prism. Thus, base pressure measurements were done at the trailing edge of the prism. There were one pressure tap at the centre and at mid-depth and two equally spaced taps from the centre called south base

pressure tap and north base pressure tap referencing to the north and south wall of the test section (Figure B.2).

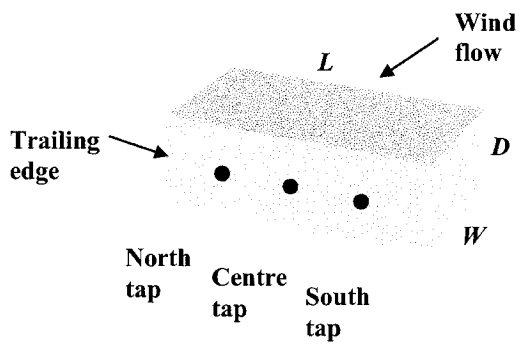

Figure B.2: View of the trailing edge of a rectangular prism with the centre, north and south base pressures.

A difference in the base pressure measurements along the model span could indicate a reduction of the 2D flow condition. Assuming the centre pressure tap as the reference, percent variation of the north and south pressure taps were calculated and results are presented in the Figures B.3 to B.14 in function of the angle of attack of the prism and for different *Re*. A negative percent variation means that the north or south pressure tap had more suction than the base pressure tap at the centre of the trailing edge and inversely, a positive percent variation means a lower suction for the north or south base pressures compared to the one at the centre.

It can be observed from these figures that the percent variation is comprised between -20% to 20%. Regardless of the prism shape, there was a strong similarity of the percent variation for the north and south base pressures. This agreement can correspond to a flow

symmetry on each side of the centreline of the prism.

In general, low percent variation for angle of attack up to 6° was observed when turbulence was added to the flow. It was also observed that the percent variation had a tendency to increase for higher angles of attack as showed on Figures B.3 to B.8.

Increasing the fineness ratio from 2 to 4 in smooth flow brought the percent variation from positive to negative values for angles of attack up to 6° and did not affect significantly the percent variation for higher angles of attack. However, in turbulent flow, increasing the fineness ratio did not affect the percent variation of the north and south base pressures.

Fineness of 2, smooth flow

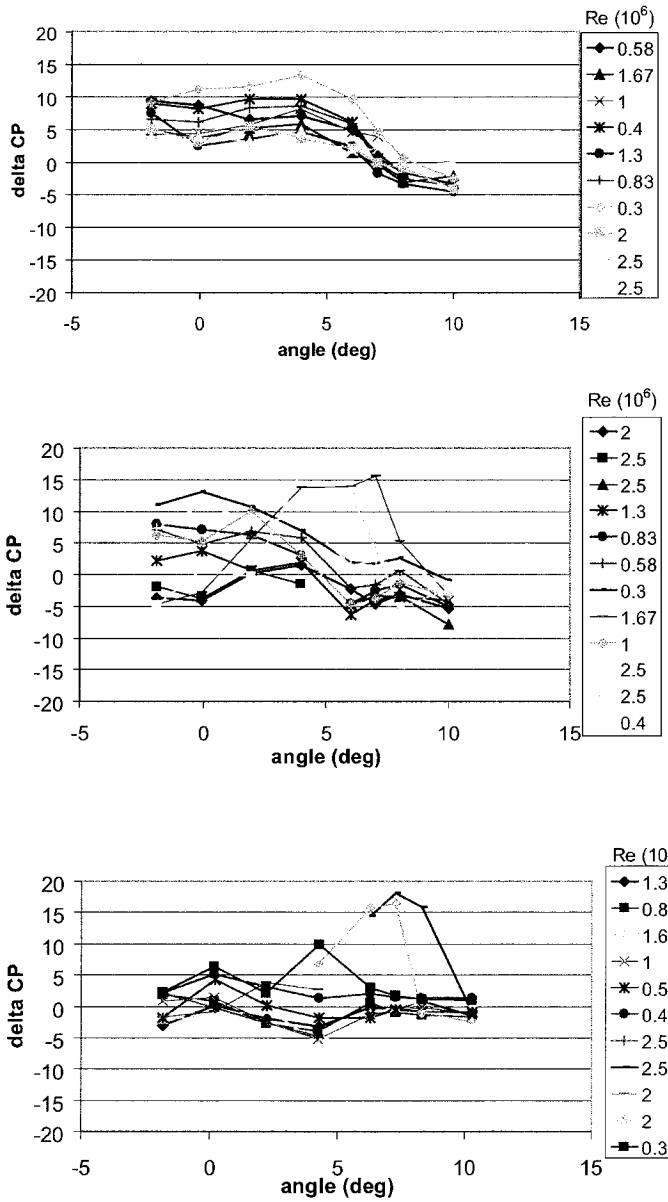

Figure B.3: Percent variation of the south base pressure with the centre base pressure versus angle of attack for a 2:1 prism in smooth flow, for 3 edge configurations and for different Reynolds number.

Fineness of 2, turbulent flow

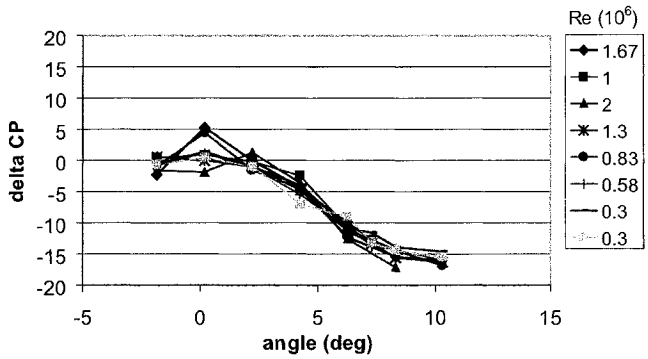

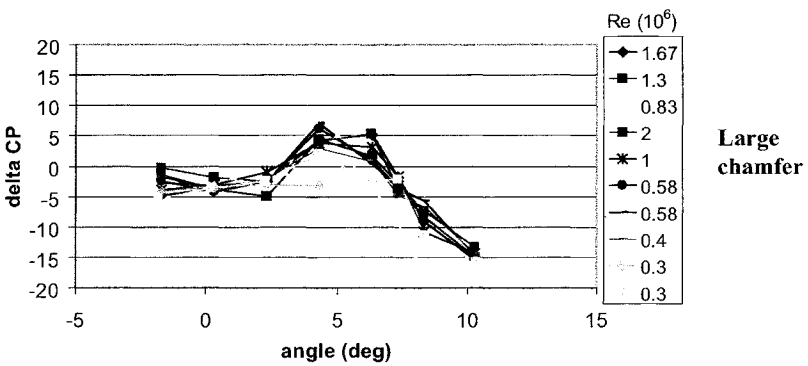

Figure B.4: Percent variation of the south base pressure with the centre base pressure versus angle of attack for a 2:1 prism in turbulent flow, for 2 edge configurations and for different Reynolds number.

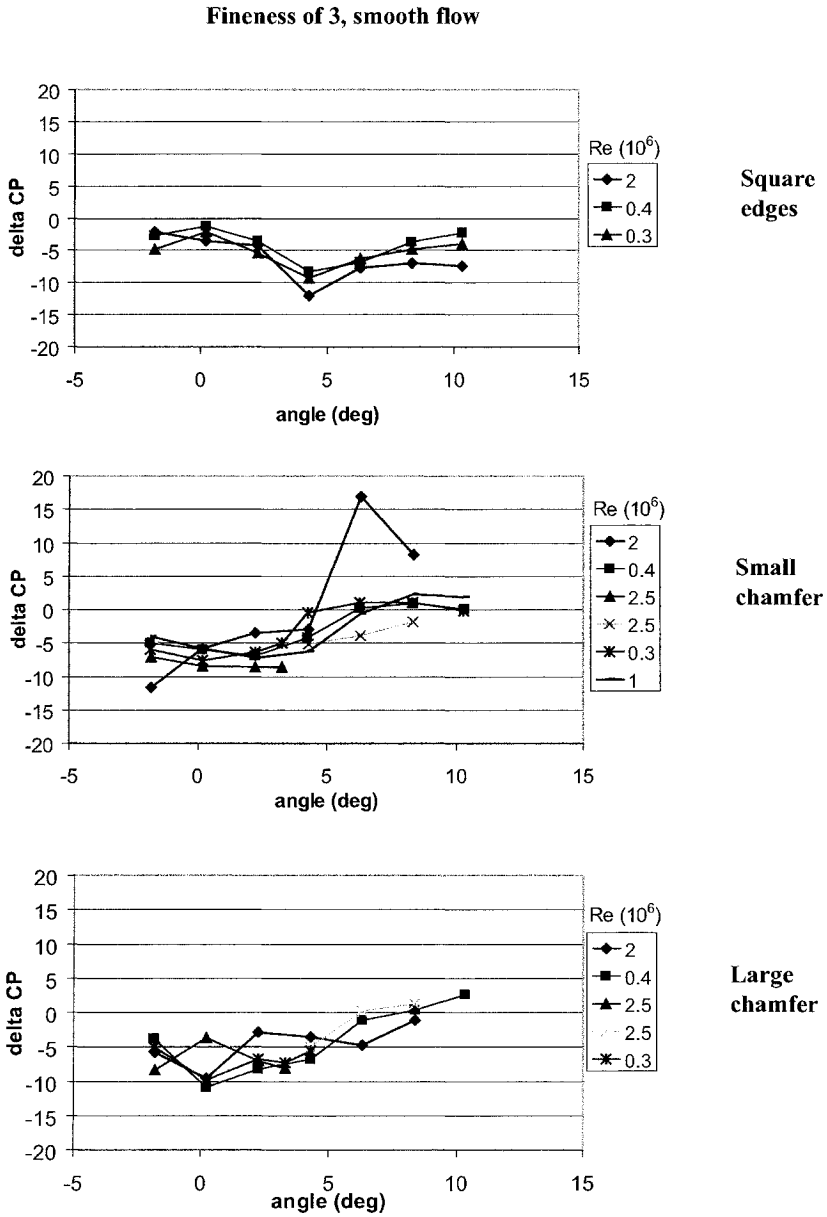

Figure B.5: Percent variation of the south base pressure with the centre base pressure versus angle of attack for a 3:1 prism in smooth flow, for 3 edge configurations and for different Reynolds number.

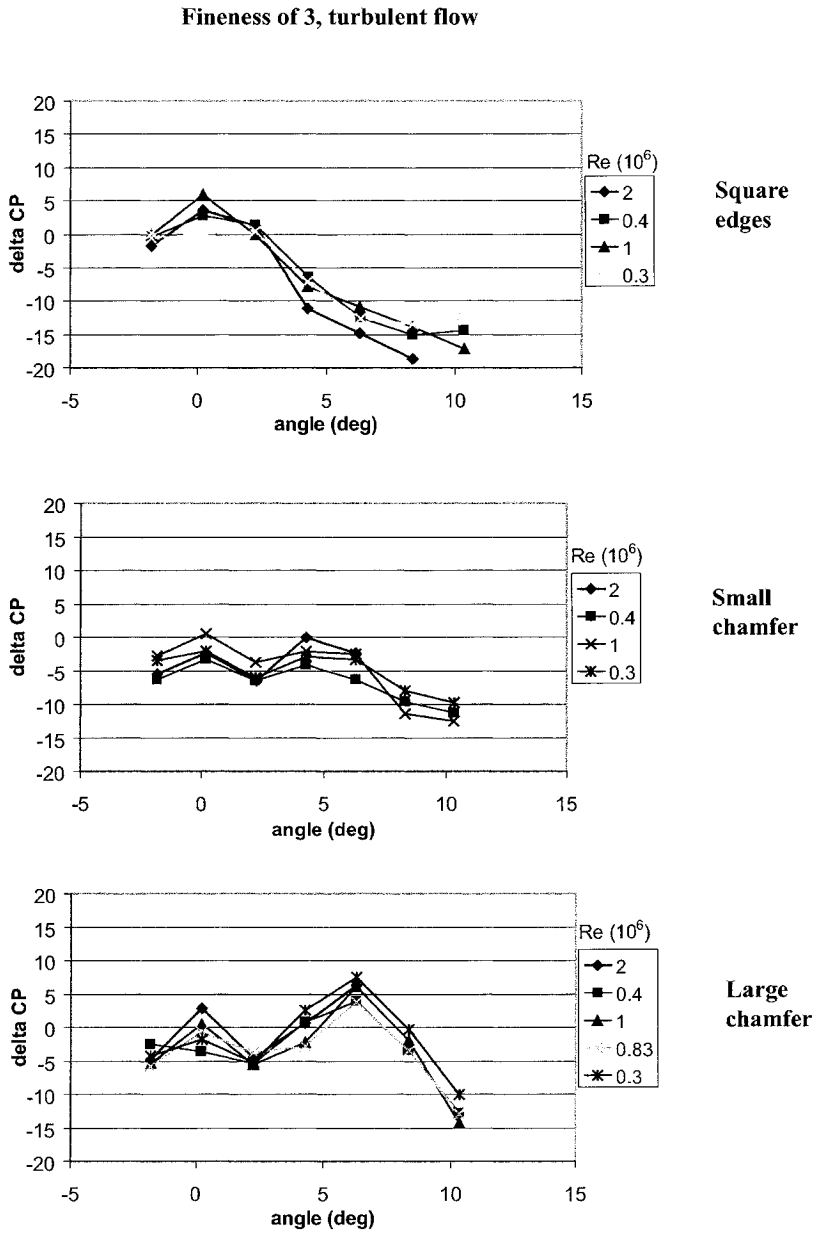

Figure B.6: Percent variation of the south base pressure with the centre base pressure versus angle of attack for a 3:1 prism in turbulent flow, for 3 edge configurations and for different Reynolds number.

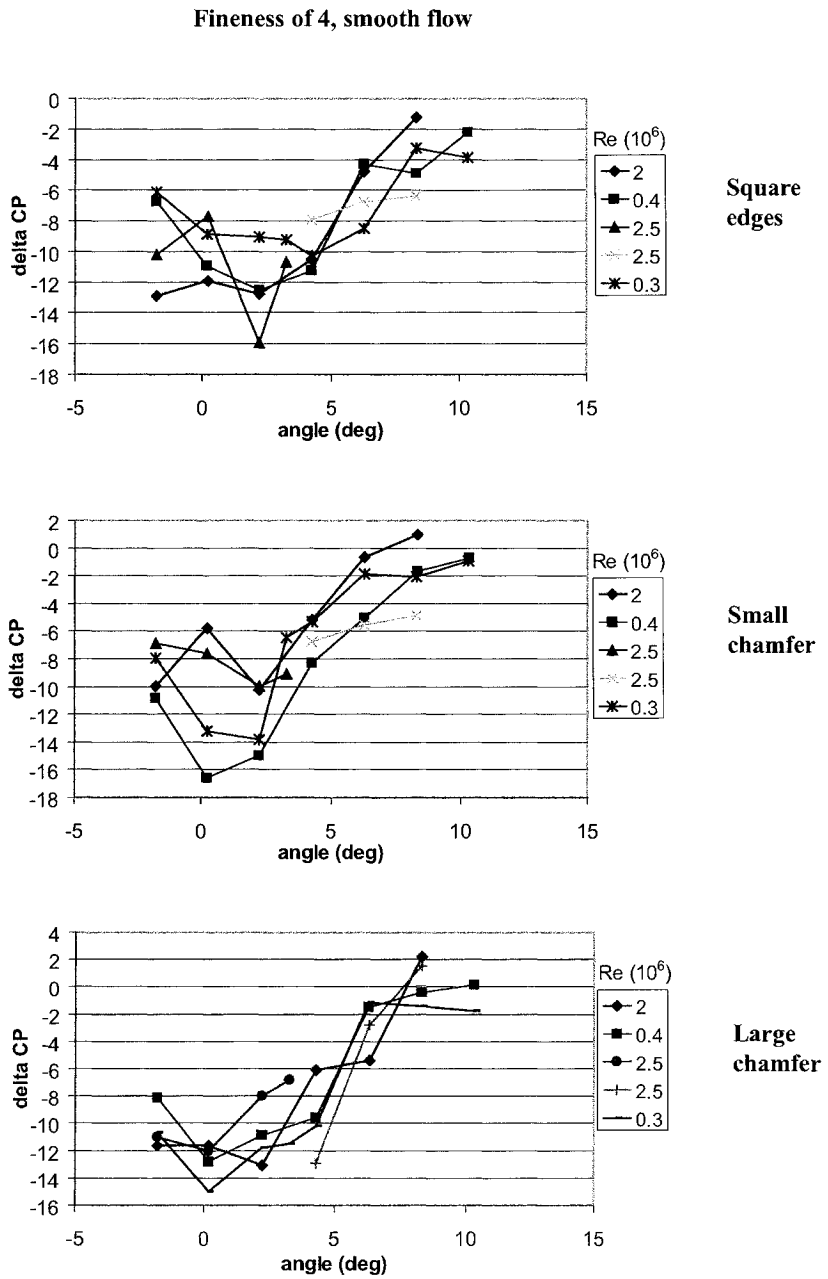

Figure B.7: Percent variation of the south base pressure with the centre base pressure versus angle of attack for a 4:1 prism in smooth flow, for 3 edge configurations and for different Reynolds number.

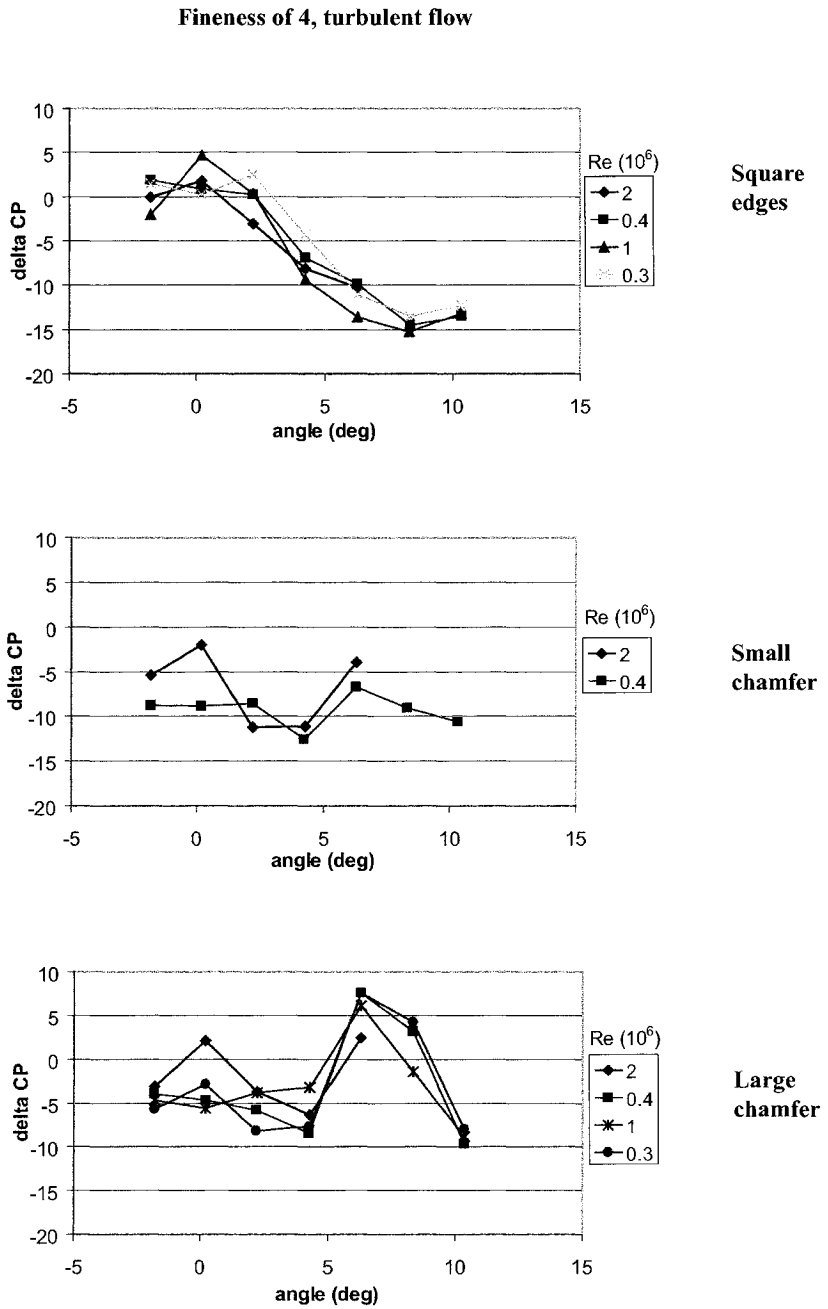

Figure B.8: Percent variation of the south base pressure with the centre base pressure versus angle of attack for a 4:1 prism in turbulent flow, for 3 edge configurations and for different Reynolds number.

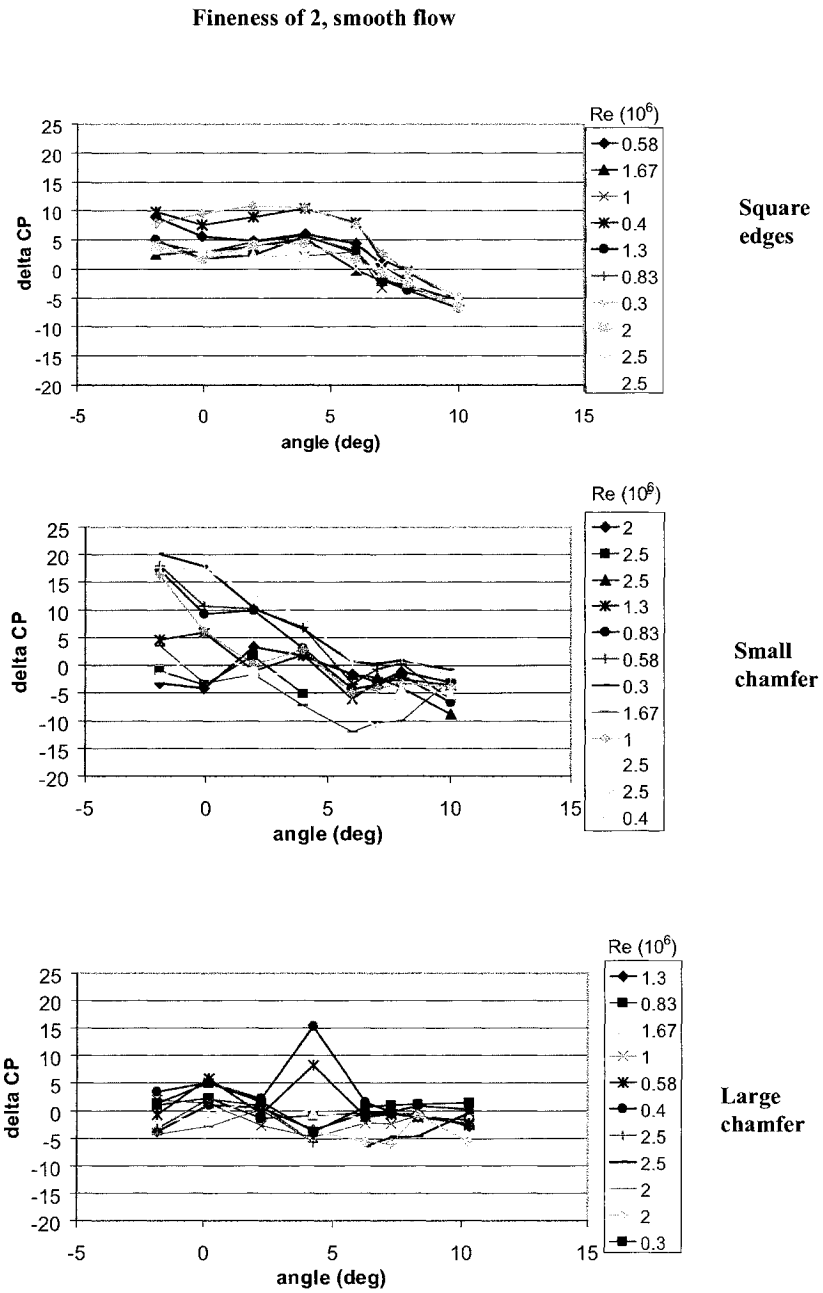

Figure B.9: Percent variation of the north base pressure with the centre base pressure versus angle of attack for a 2:1 prism in smooth flow, for 3 edge configurations and for different Reynolds number.

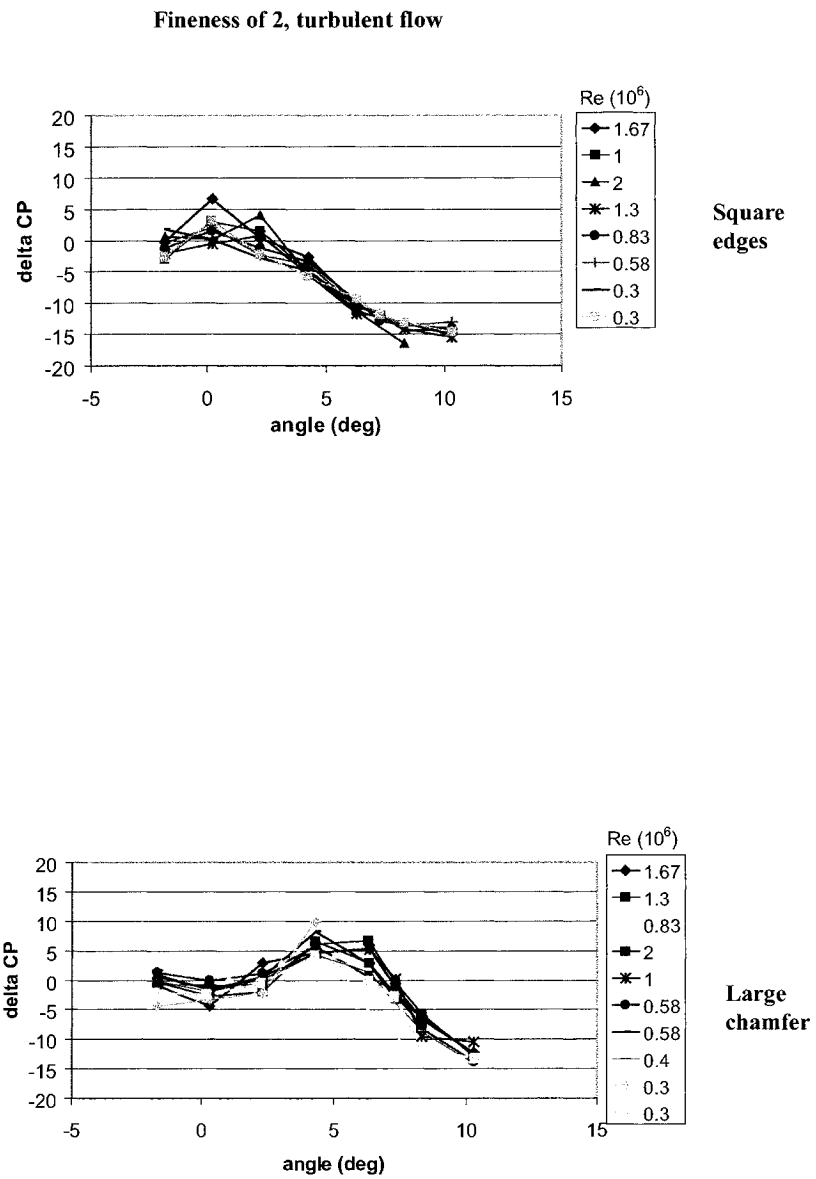

Figure B.10: Percent variation of the north base pressure with the centre base pressure versus angle of attack for a 2:1 prism in turbulent flow, for 2 edge configurations and for different Reynolds number.

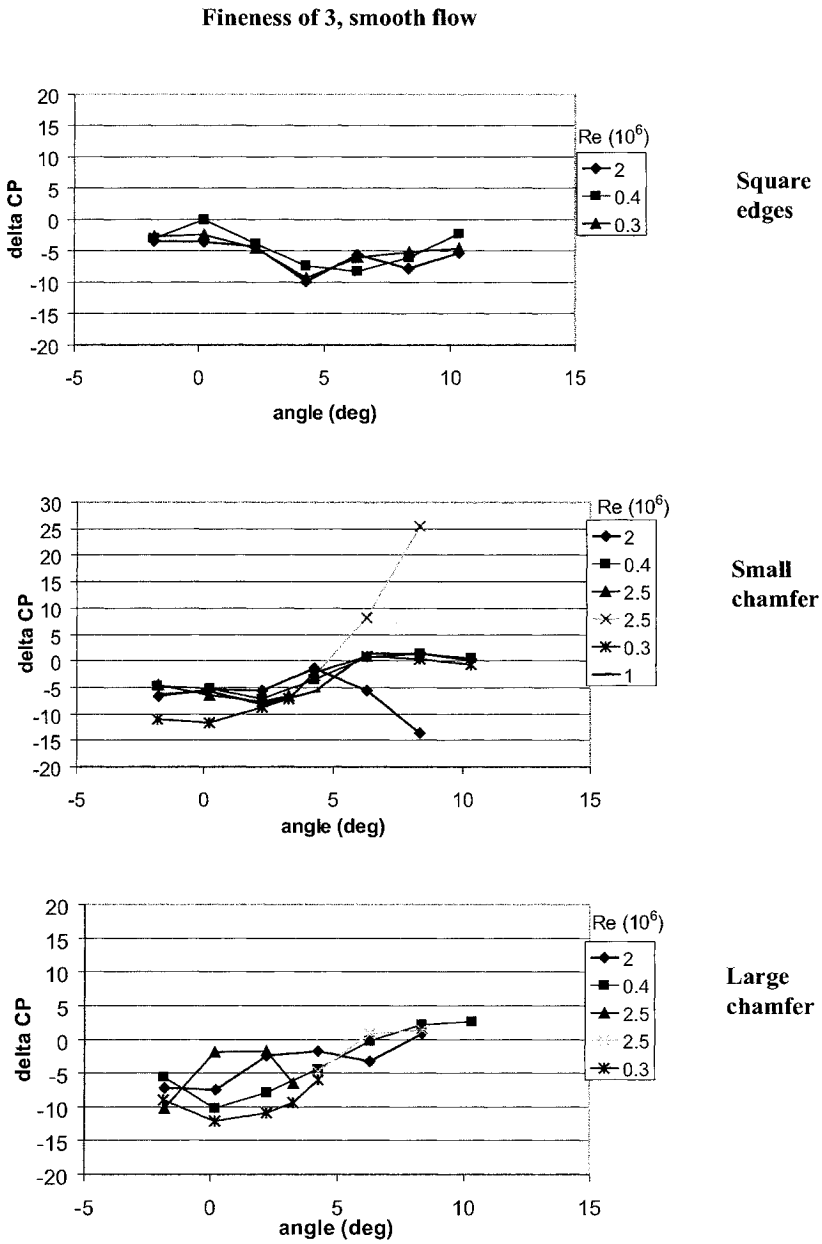

Figure B.11: Percent variation of the north base pressure with the centre base pressure versus angle of attack for a 3:1 prism in smooth flow, for 3 edge configurations and for different Reynolds number.

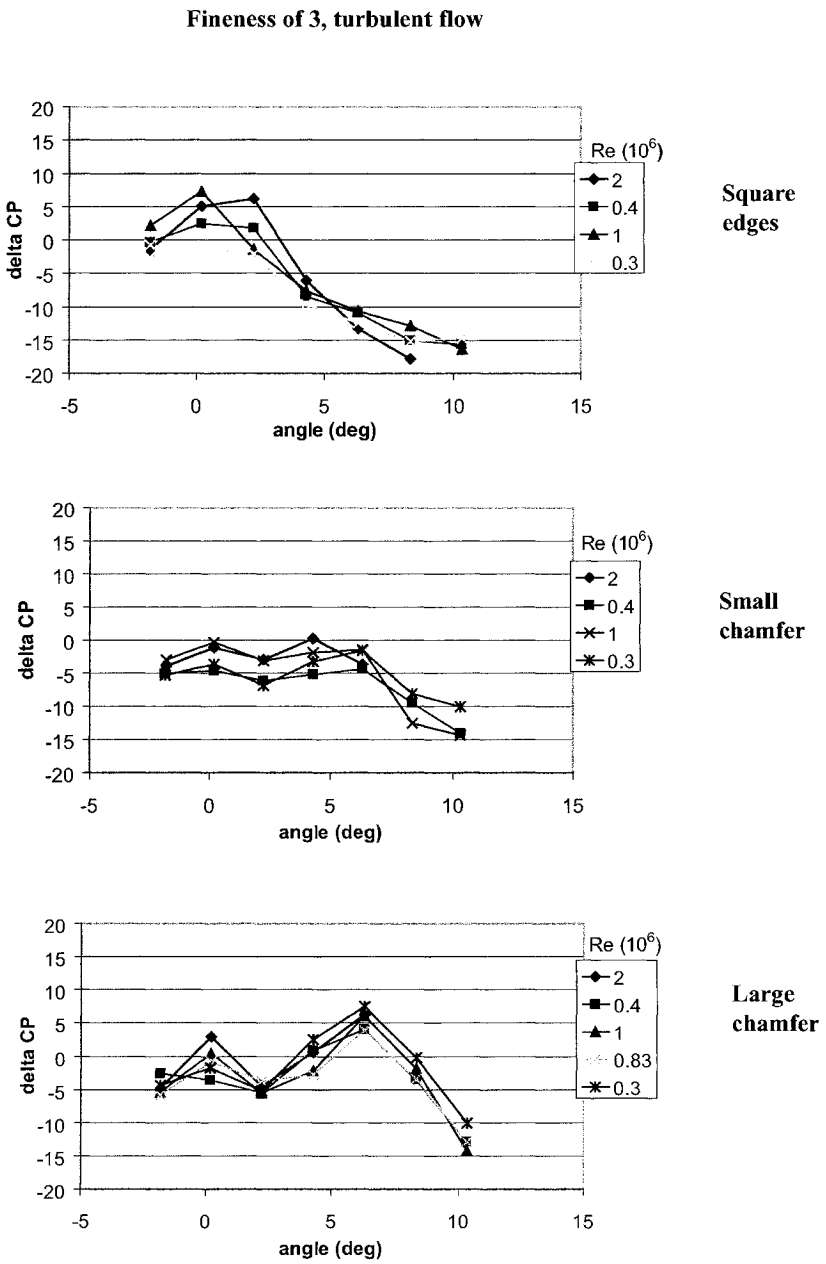

Figure B.12: Percent variation of the north base pressure with the centre base pressure versus angle of attack for a 3:1 prism in turbulent flow, for 3 edge configurations and for different Reynolds number.

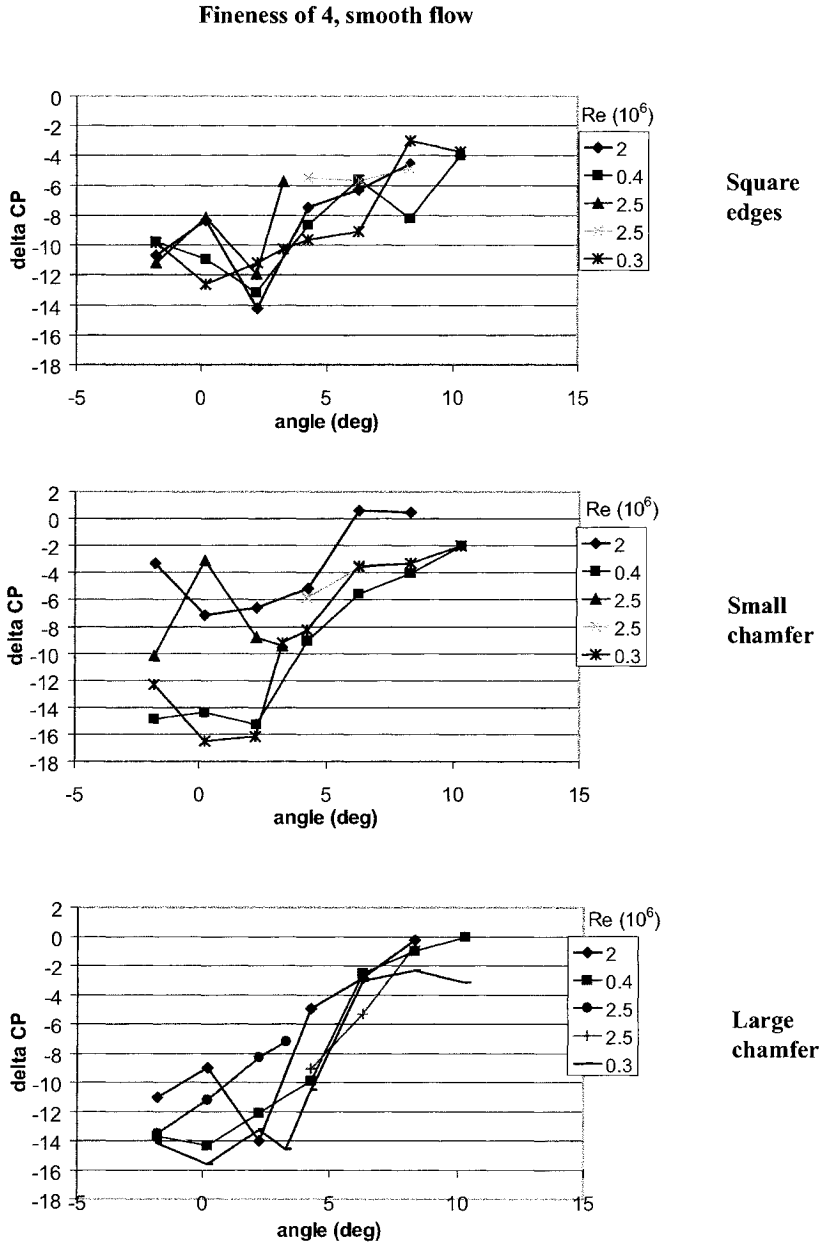

Figure B.13: Percent variation of the north base pressure with the centre base pressure versus angle of attack for a 4:1 prism in smooth flow, for 3 edge configurations and for different Reynolds number.

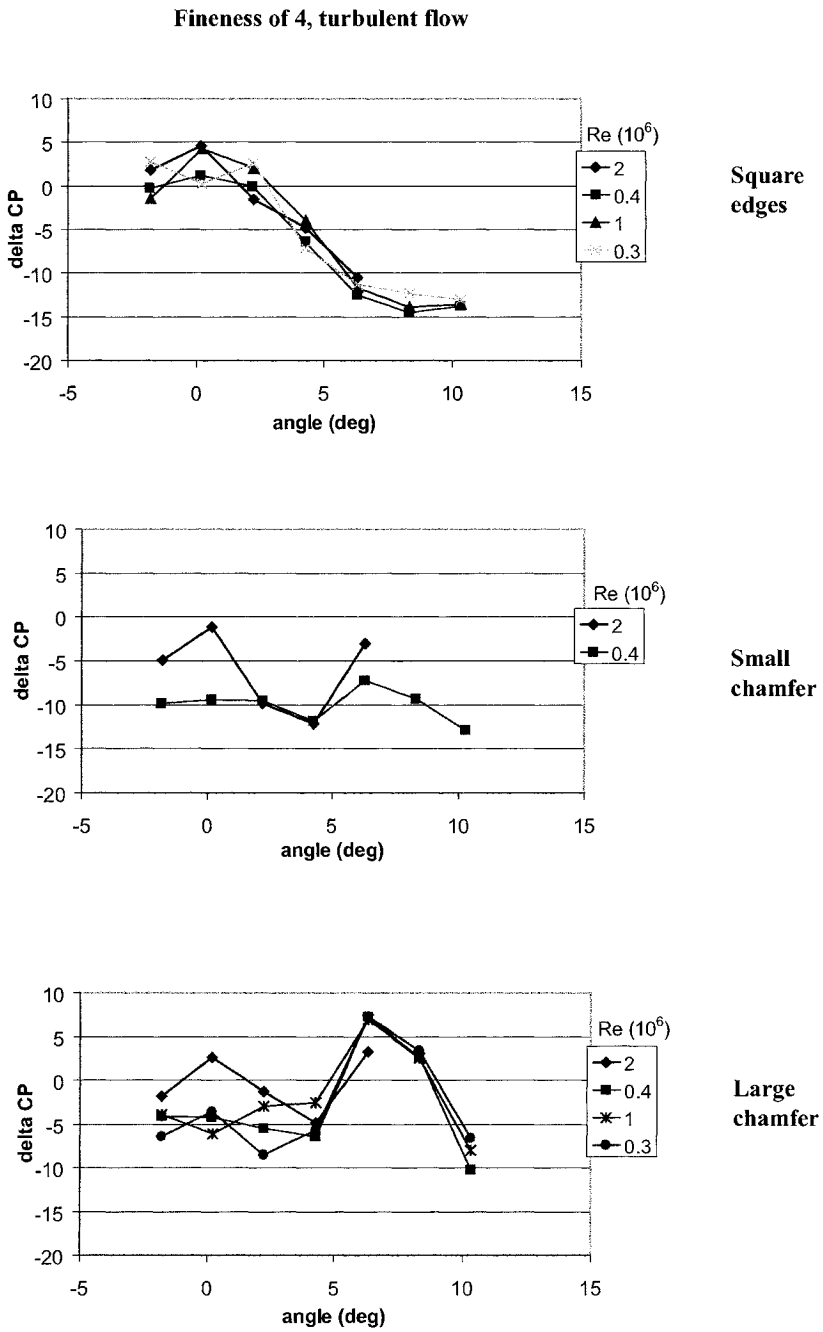

Figure B.14: Percent variation of the north base pressure with the centre base pressure versus angle of attack for a 4:1 prism in turbulent flow, for 3 edge configurations and for different Reynolds number.

B.2 Surface pressure integration

Since a pressure is defined as a ratio of the force by unit of area, an addition of all local forces from the product of the pressure taps of the chord-wise centreline strip with the corresponding surface area will give the total force acting on the prism. The surface area is formed by the length over which each pressure is acting on the chord-wise strip and multiplied by the constant length of the prism of 381 mm. If the bi-dimensionality of the flow is respected, the pressure distribution on the centreline chord-wise strip should be the same at any cross-flow location on the prism.

To verify the 2D flow condition, the aerodynamic coefficients computed from the forces measured by the external balance could be compared to surface pressure integration for one chordwise strip. Thus, the drag force coefficient from balance measurement was compared to the drag force coefficient from surface pressure integration. It is expected that the drag force measured by the external balance will be higher than the surface pressure integration since the drag from the balance is the summation of the pressure drag and the friction drag while the surface pressure integration only considered the contribution of the pressure to the total drag. However, for a rectangular prism for which most of the flow is separated, the pressure drag will dominate the friction drag.

For a positive percent of variation of the drag coefficient from the surface pressure integration with the balance drag force coefficient, it means that the balance drag force coefficient had a higher value than the one from integration of surface pressure. Inversely, a

negative percent variation means that the drag force coefficient from the balance measurement was lower than the integration of the surface pressure. There could be two explanations for the latter case. First, the flow could be more than likely 3D and not anymore 2D, leading to different cross-flow surface pressure distribution along the chord of the prism or, the surface pressure integration could be overestimated by assuming the same surface pressure for the total depth of the prism at the trailing edge while there could be a pressure profile that will have reduced the drag force generated at the trailing edge.

All results of the percent of variation between the drag force coefficient from the integration of surface pressure with the drag force coefficient from the balance are presented on Figures B.15 to B.20.

It can be observed from these figures that the percent variation was comprised between -40% to 35%. In general, the turbulence had a strong effect on prism with square edges regardless of the fineness ratio. In fact, the turbulence gave positive percent of variation for high angles of attack of the prism while in smooth flow, prisms with square edges presented negative percent of the drag coefficient variation.

Increasing the fineness ratio from 2 to 4 in smooth flow brought the percent variation from positive to negative values for angles of attack up to 6° and did not affect significantly the percent variation for higher angles of attack. However, in turbulent flow, increasing the fineness ratio did not affect the percent variation. This is consistent with the results obtained from the base pressure measurements.

In general, the percent variation was higher for larger *Re* particularly in smooth flow regardless of the prism shape and the percent variation between two *Re* was smaller in turbulent flow than in smooth flow with curves closer to each others.

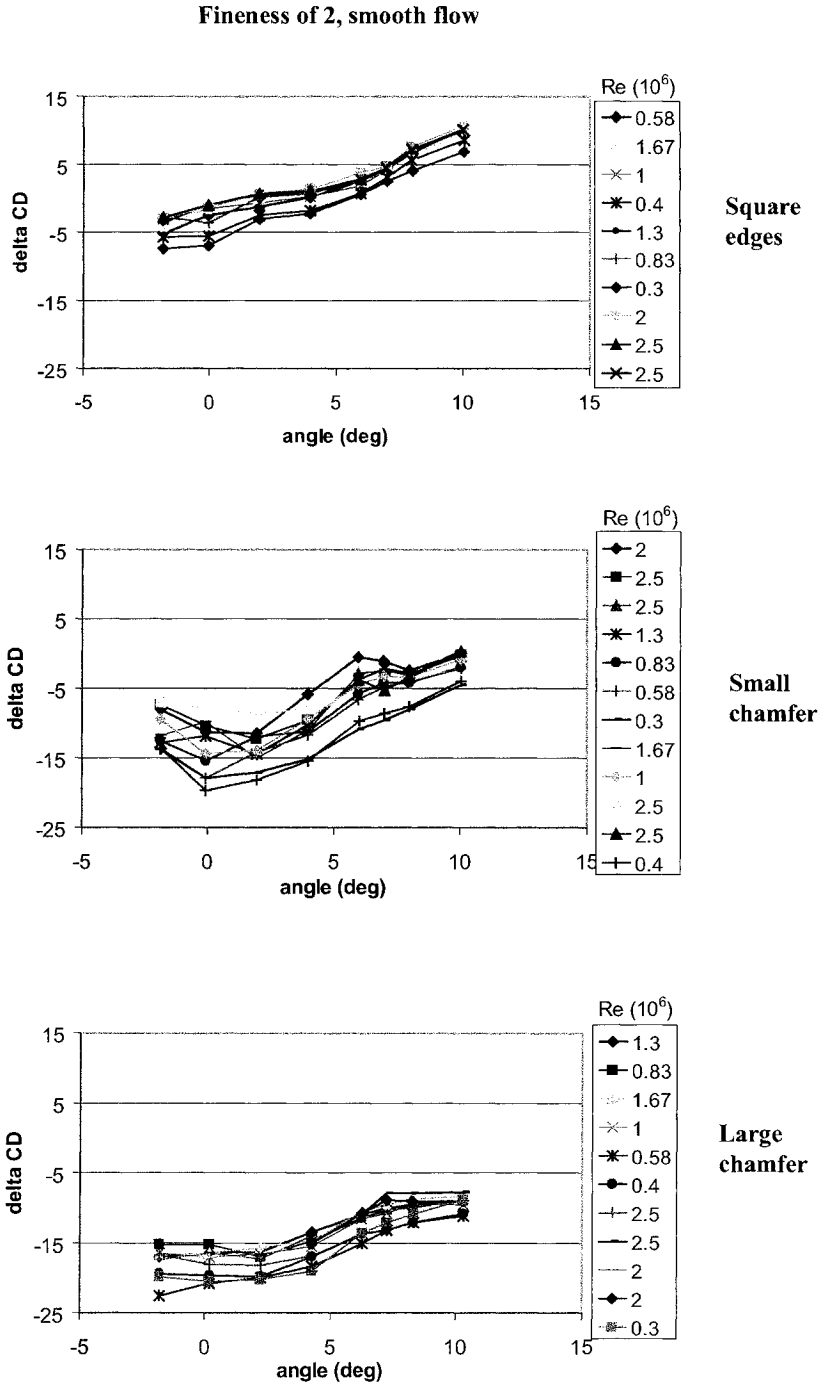

Figure B.15: Percent variation of the drag force coefficient of the surface pressure integration with the force balance measurement versus angle of attack for a 2:1 prism in smooth flow, for 3 edge configurations and for different Reynolds number.

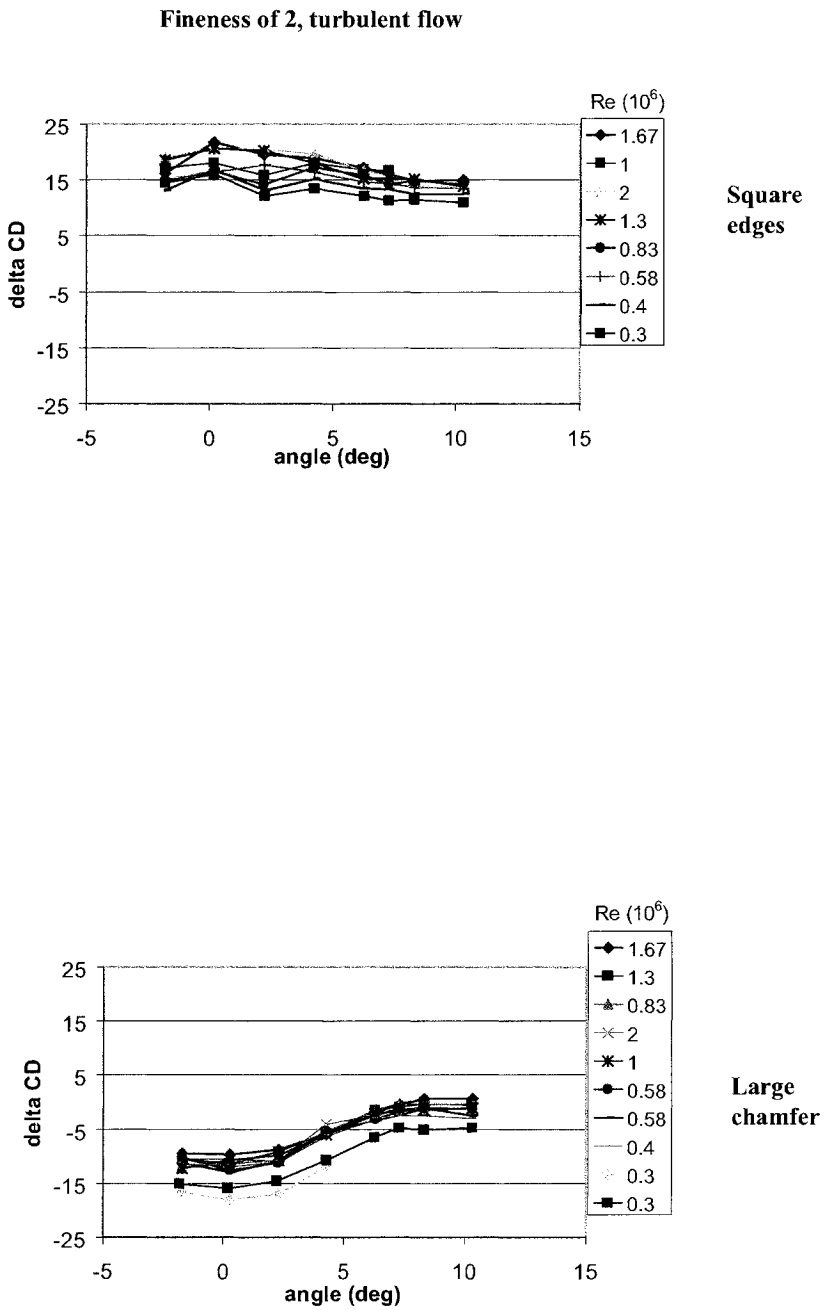

Figure B.16: Percent variation of the drag force coefficient of the surface pressure integration with the force balance measurement versus angle of attack for a 2:1 prism in turbulent flow, for 2 edge configurations and for different Reynolds number.

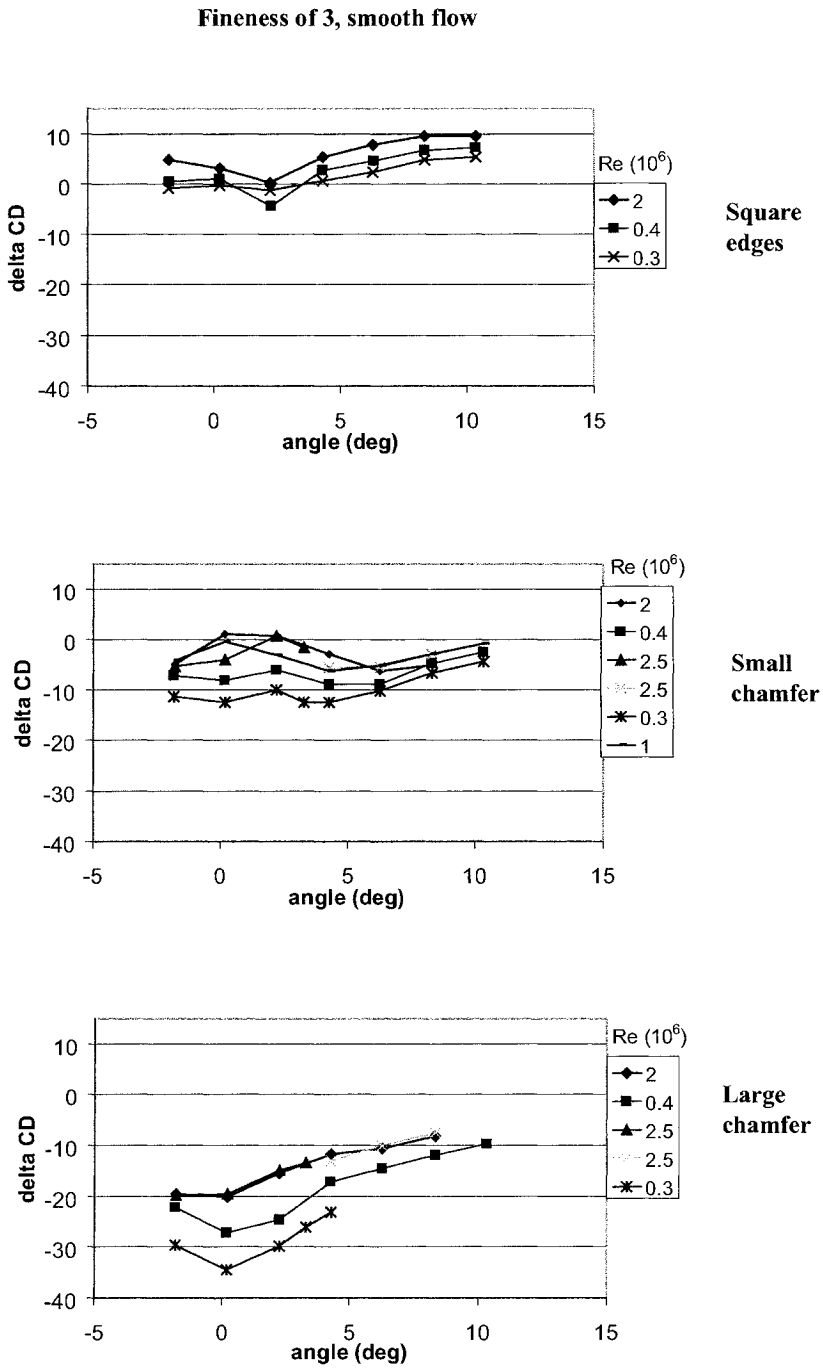

Figure B.17: Percent variation of the drag force coefficient of the surface pressure integration with the force balance measurement versus angle of attack for a 3:1 prism in smooth flow, for 3 edge configurations and for different Reynolds number.

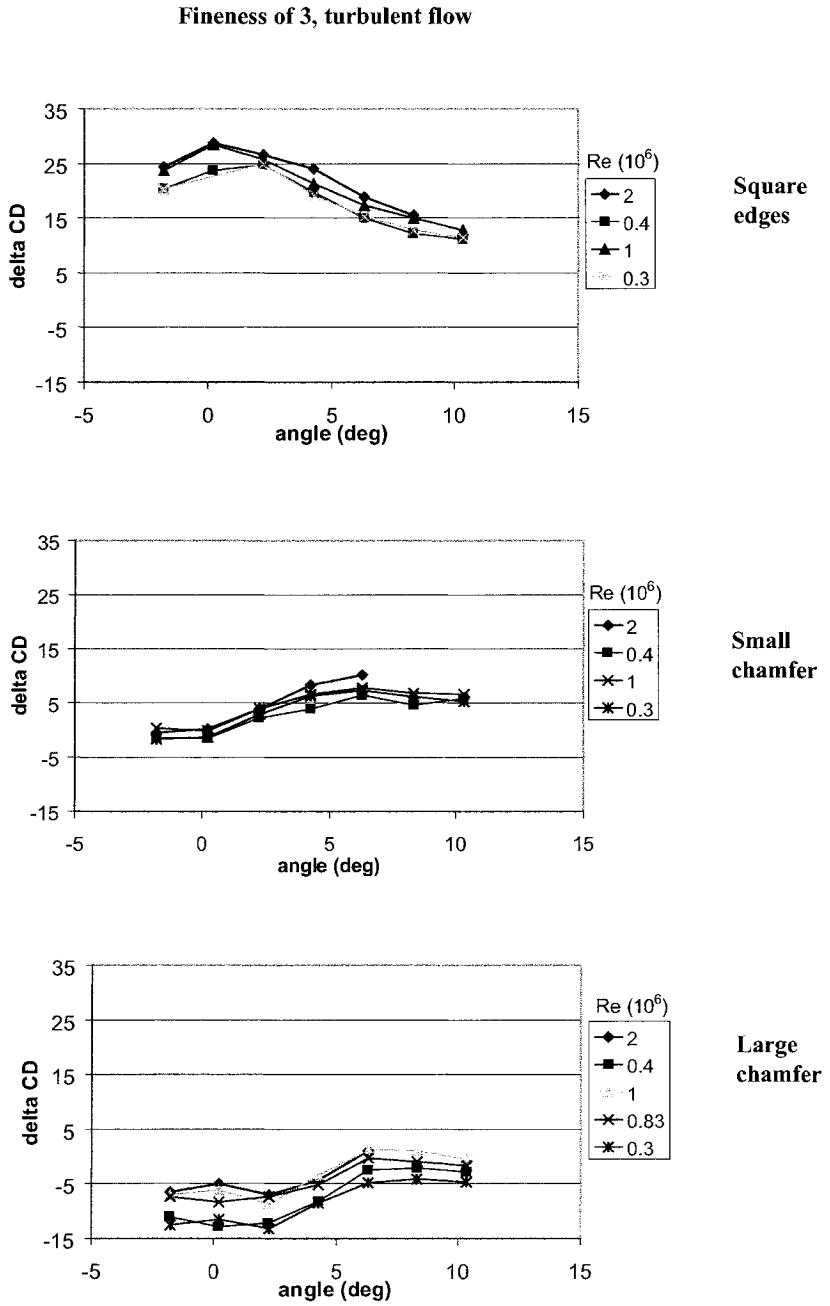

Figure B.18: Percent variation of the drag force coefficient of the surface pressure integration with the force balance measurement versus angle of attack for a 3:1 prism in turbulent flow, for 3 edge configurations and for different Reynolds number.

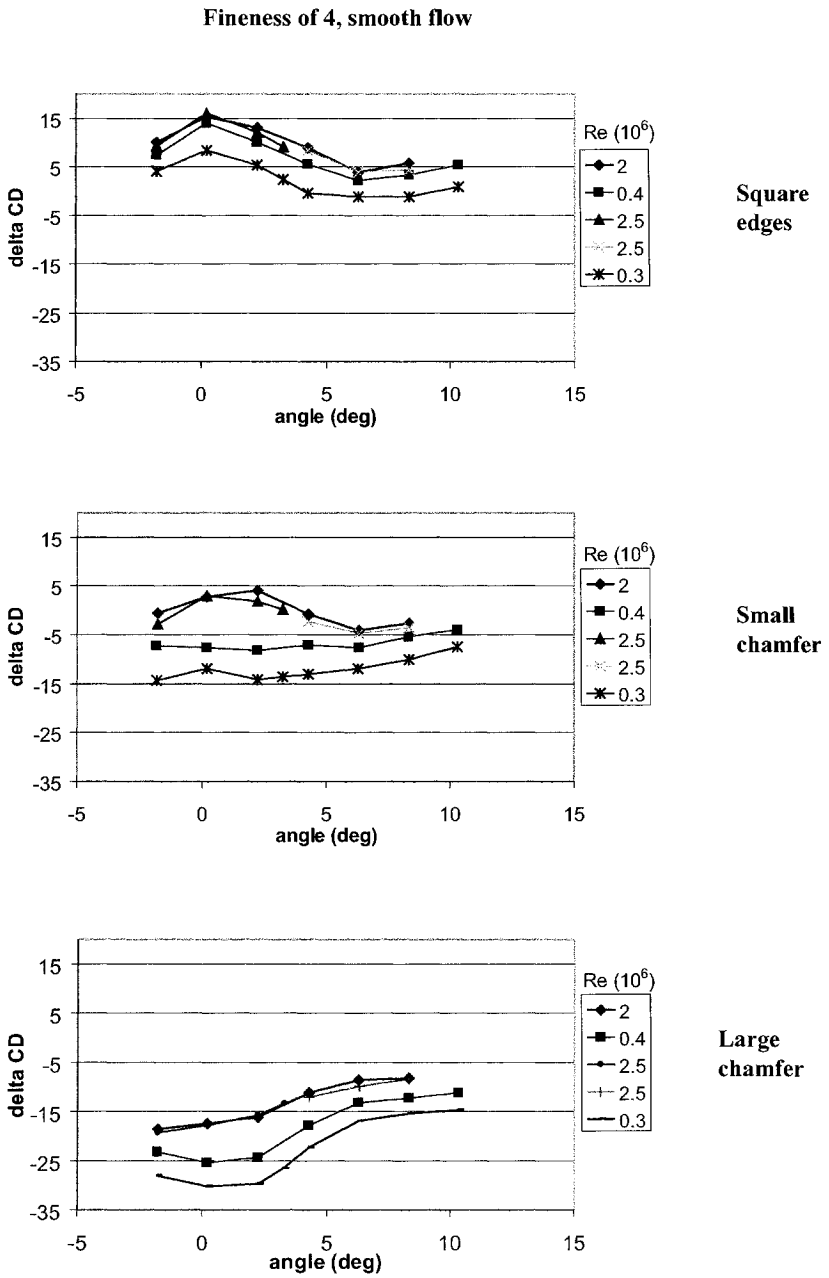

Figure B.19: Percent variation of the drag force coefficient of the surface pressure integration with the force balance measurement versus angle of attack for a 4:1 prism in smooth flow, for 3 edge configurations and for different Reynolds number.

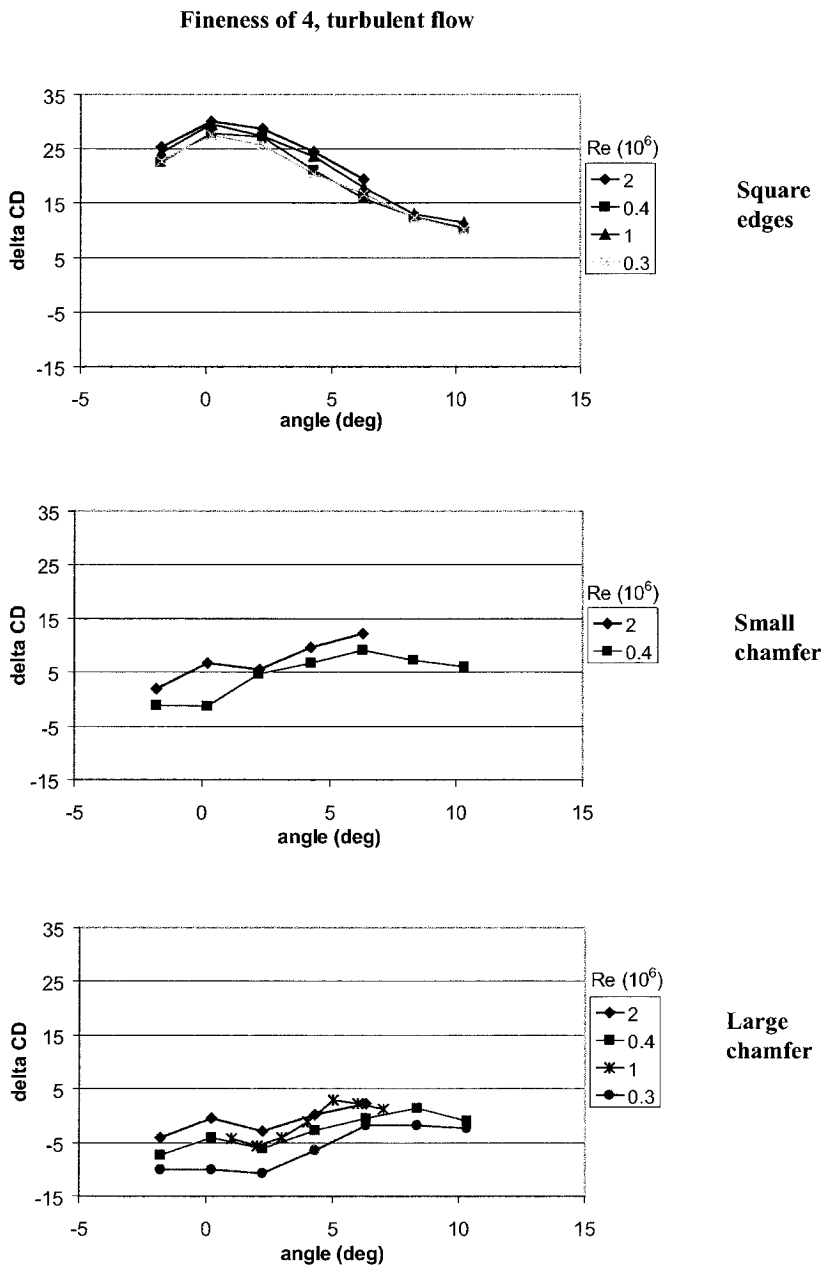

Figure B.20: Percent variation of the drag force coefficient of the surface pressure integration with the force balance measurement versus angle of attack for a 4:1 prism in turbulent flow, for 3 edge configurations and for different Reynolds number.

B.3 Flow visualisation

To verify the bi-dimensionality of the mean flow , flow visualisation was carried out using fluorescent oil application on the prism. This allowed to see the streamlines and/or the flow pattern that developed at the surface of the prism for a given flow condition. It is assumed that for a location on the prism where there is no circulation or recirculation flow, the oil will be essentially maintain as dot points. However, for regions over the body where flow circulation is active, streamlines will be drawn.

Flow visualisation was done for 2 prism configurations. The first one was for a 2:1 fineness ratio prism with large chamfer in turbulent flow at 4° and Re of 1.0×10^6 as presented on Figure B.21. The second flow visualisation was performed on a 2:1 prism with square edges in turbulent flow at 4° and Re of 0.58×10^6 (Figure B.22).

It can be observed on these figures that the prism with large chamfer showed more streamline patterns than the one with square edges for the top part of the prism. This means that at 4°, square edges had a separated flow at the top of the prism while with large chamfer, the flapping shear layer at the top had a tendency to reattach to the body giving possibility for streamlines to appear. The trailing edge of both prisms presented only oil dots without any visible streamline consistent with a separated flow area where suction is predominant. Finally, a streamline pattern is observed at the bottom of both prisms where a clear line divided two streamline regions, one region where the separated bubble is predominant and another region where the freestream flow has more impact on the streamline patterns. These two regions are separated by a reattachment point represented more than likely by the dark line where no circulating flow is acting.

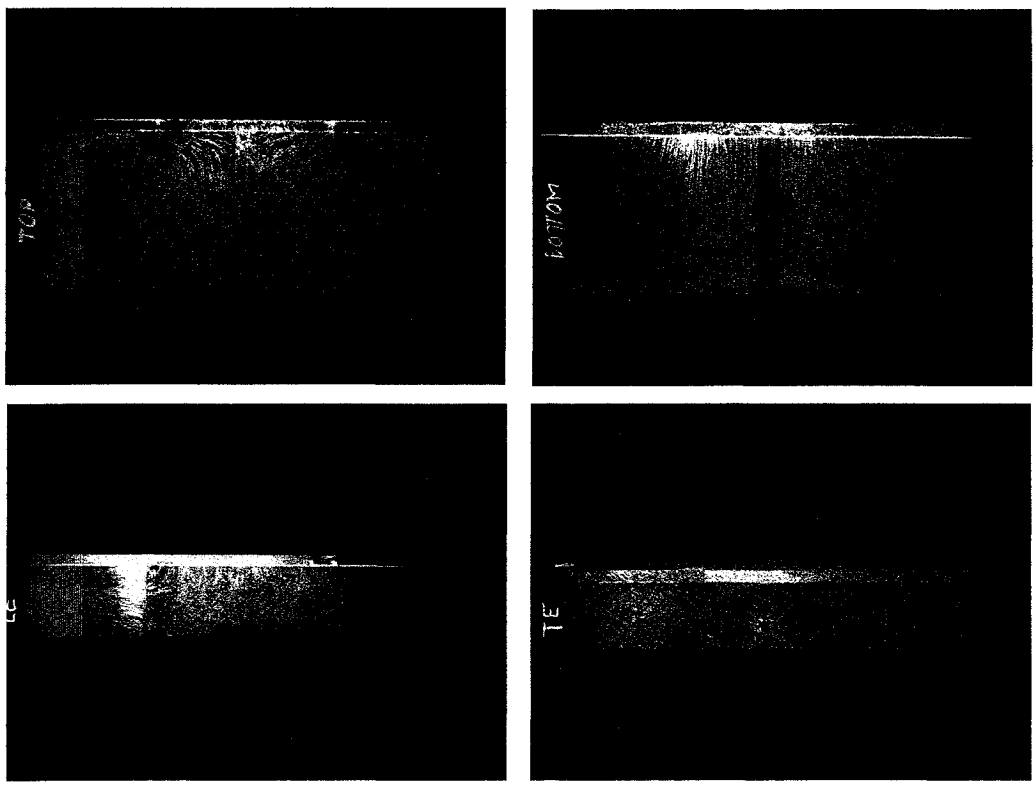

Figure B.21: Oil flow visualisation at the top (top-left), bottom (top-right), leading edge (bottom-left) and trailing edge (bottom-right) of a 2:1 fineness ratio prism with large chamfer, at angle of attack of 4° and in turbulent flow, $Re : 1.0 \times 10^6$.

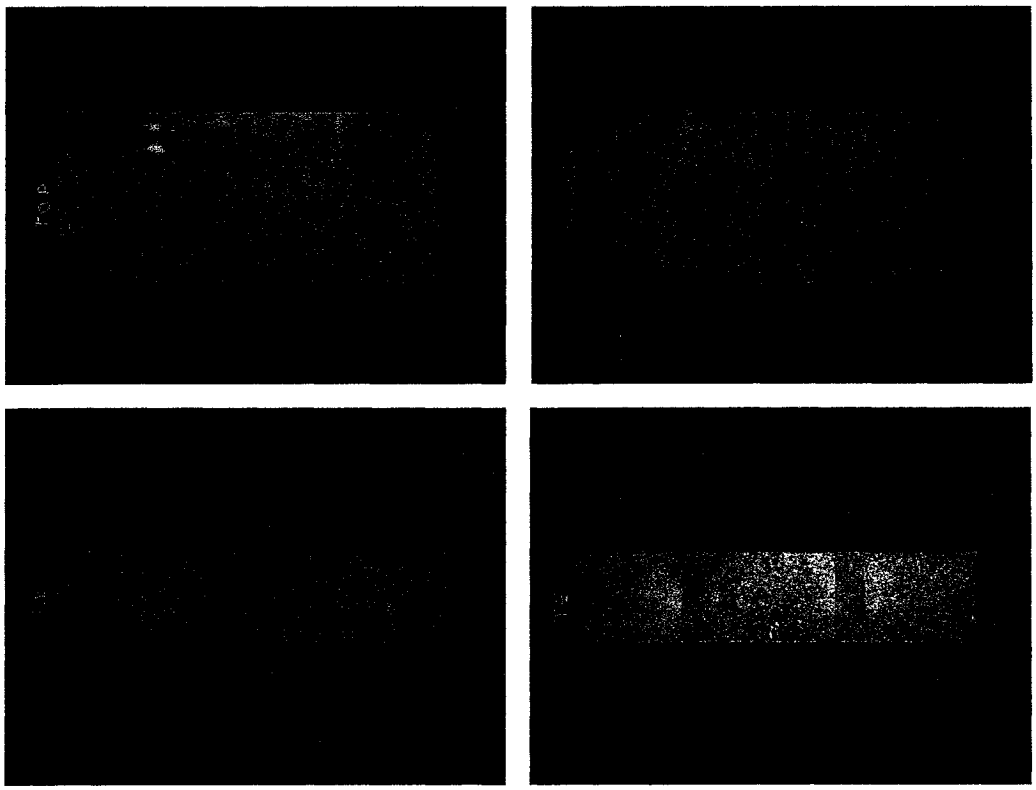

Figure B.22: Oil flow visualisation at the top (top-left), bottom (top-right), leading edge (bottom-left) and trailing edge (bottom-right) of a 2:1 fineness ratio prism with square edges, at angle of attack of 4° and in turbulent flow, $Re : 0.58 \times 10^6$.

B.4 Discussion

In light of the base pressure measurements, the comparison of the drag coefficient from surface pressure integration and from external force balance measurements and, the flow visualisation, the bi-dimensionality of the flow during the study was not constant. While in smooth flow, tests on prisms with larger fineness ratio presented higher bi-dimensionality flow characteristics, the opposite situation was observed for tests in turbulent flow.

On the other hand, tests done in smooth flow presented higher 2D conditions for square edge prisms compared to tests on prisms with chamfers and the opposite situation was observed in turbulent flow.

Considering a rectangular prism to be more streamlined when its fineness ratio is larger and/or when chamfers are added, higher bi-dimensionality of the flow was observed for streamlined body in smooth flow when increasing the fineness ratio while, in turbulent flow higher bi-dimensionality of the flow was observed for streamlined body when adding chamfers.

Thus, a rectangular prism with a relatively higher streamlined cross-section characteristics will not necessarily have better 2D flow conditions. Turbulence in the flow, fineness ratio and edge treatment are other parameters to consider when the issue of bi-dimensionality of the flow field on rectangular prisms is raised.

Bibliography

[1] B. R. Munson, D. F. Young, and T.H. Okiishi. *Fundamentals of fluid mechanics*. John Wiley & Sons, Inc., New-York, 1998.

[2] L. Prandtl and O. G. Tietjens. *Applied hydro and aeromechanics*. McGraw-Hill, New York, 1934.

[3] G. L. Larose and A. D'Auteuil. On the Reynolds number sensitivity of the aerodynamics of bluff bodies with sharp edges. *Proc. of the Convegno internazionale di ingegneria del vento, Reggio Calabria*, pages 21–29, 2004.

[4] E. Simiu and R. H. Scanlan. *Wind effect on structures, 3rd edition*. John Wiley & Sons, Inc., New-York, 1996.

[5] R.D. Galway. The IAR high Reynolds number two-dimensional test facility-description of equipment and procedures common to most 2D airfoil tests. *National Research Council Canada Technical Report, IAR-AN-66*, pages 1–44, 1990.

[6] G. L. Larose and A. D'Auteuil. Experiments on 2-D rectangular prisms at high Reynolds number in a pressurised wind tunnel. *Proc. of the Fifth International Colloquium on Bluff Body Aerodynamics and Applications, Ottawa, Canada*, pages 177–181, 2004.

[7] K. Shimada and T. Ishihara. Prediction of aeroelastic vibration of rectangualr cylinders by $k-\varepsilon$ model. *Journal of Aerospace engineering*, pages 122–135, 1999.

[8] J. M. Robertson, J. E. Cermak, and S. K. Nayak. A Reynolds-number effect in flow past prismatic bodies. *Mechanics Research Communications*, pages 279–282, 1975.

[9] ESDU. Fluid forces on non-streamline bodies-background notes and description of the flow phenomena. 1971.

[10] P. W. Bearman and T. Morel. Effect of free stream turbulence on the flow around bluff bodies. *Progress in aerospace sciences*, pages 97–123, 1984.

[11] A. Laneville, I. S. Gartshore, and G. V. Parkinson. An explanation of some effects of turbulence on bluff bodies. *Trans. Amer. Math. Soc.*, pages 975–995, 1971.

[12] J. Courchesne and A. Laneville. An experimental evaluation of drag coefficient for rectangular cylinders exposed to grid turbulence. *Fluids Engineering*, pages 523–527, 1982.

[13] J. A. Robertson, C. Y. Lin, G. S. Rutherford, and M. D. Stine. Turbulence effects on drag of sharp-edged bodies. *Hydraulics Division*, pages 1187–1201, 1972.

[14] N. K. Delany and N. E. Sorenson. Low-speed drag of cylinders of various shapes. *National Advisory Committee for Aeronautics, Technical notes 3038*, pages 1–22, 1953.

[15] G. Schewe. Reynolds-number effects in flow around more-or-less bluff bodies. *Wind Engineering and Industrial Aerodynamics*, pages 1267–1289, 2001.

[16] V.D. Nguyen and G.L. Larose. *Test Specification for the wind tunnel investigation of the 2D bluff body models in the IAR High Reynolds number 2D Test facility*. National Research Council Canada Technical Memorandum, LM-AL-2002-0060, 2002.

[17] S.J. Zan and K. Matsuda. Steady and unsteady loading on roughened circular cylinder at Reynolds number up to 900 000. *Journal of Wind Engineering and Industrial Applications*, pages 567–581, 2002.

[18] L. Ohman and M. Mokry. Application of the Fast-Fourier Transform to two-dimensional wind tunnel wall interference. *Journal of Aircraft*, pages 402–408, 1980.

[19] J.B. Barlow, W.H. Rae, and A. Pope. *Low-speed wind tunnel testing*. John Wiley and Sons, New York, 3rd edition, 1999.

[20] H.P.A.H. Irwin and K.R. Cooper. *Correction of distorsion in fluctuating pressure measurements*. National Research Council Canada Technical Report, LTR-LA-222, 1980.

[21] A. G. Davenport. The missing links. *Wind Engineering into the 21st Century, Larsen, Larose and Livesey (eds), Balkema, Rotterdam*, pages 3–13, 1999.

Curriculum Vitae

Education

2003-2005	University of Ottawa Ottawa (Ontario)	**M.A.Sc.** Civil engineering: *Wind engineering*
1999-2003	Laval University Ste-Foy (Quebec)	**B.Eng.** Engineering Physics: *Aerodynamics*

Professional Experience

2004-...	Teaching Assistant University of Ottawa	• Mechanics of Materials • Engineering Mechanics • Introduction to Fluid Mechanics
2003-2005	Guest Worker National Research Council Bluff Body Aerodynamics	• Master research • Stonecutters Bridge • Burj Dubai tower • Speed skating, Skeleton and Luge National teams
2002-2003	Student Researcher National Research Council 9m x 9m Wind Tunnel	• Flow behind race car wheel • Tacoma Narrows Bridge • Stonecutters Bridge

Publications

Journals:

- G.L. Larose, A. D'Auteuil. On the Reynolds number sensitivity of the aerodynamics of bluff bodies with sharp edges, *accepted for publication in Journal of Wind Engineering and Industrial Aerodynamics*, 2005.

Conference Proceedings:

- G.L. Larose, A. D'Auteuil. Experiments on 2-D rectangular prisms at high Reynolds numbers in a pressurised wind tunnel, *Proc. of the Fifth International Colloquium on Bluff Body Aerodynamics and Applications*, Ottawa, Canada, 2004, pp. 177-181.
- G.L. Larose, A. D'Auteuil. On the Reynolds number sensitivity of the aerodynamics of bluff bodies with sharp edges, *Proc. of the Convegno internazionale di ingegneria del vento, Reggio Calabria*, Italy, 2004, pp. 21-29.
- A. D'Auteuil, G.L. Larose. Aerodynamic behaviour of bluff bodies with sharp edges at high Reynolds number, *Proc. of the Canadian Aeronautic and Space Institute Conference*, Toronto, April 2005.
- A. D'Auteuil, G.L. Larose. Wind turbulence effects for 2-D rectangular prisms at high Reynolds number, *Proc. of the Sixth European Conference on Structural Dynamics*, Paris, Sept. 2005, pp. 355-359.

Technical reports:

- G.L. Larose, A. D'Auteuil. Wind Tunnel Experiments on Full Bridge Aeroelastic Models of the Tacoma Narrows Bridges, Washington State, USA, *LTR-AL-2003-0055, CNRC, IAR*, July 2003.
- M.G. Savage, A. D'Auteuil and A. Lafreniere. Forced Motion Sectional Model Experiments at High Reynolds Number on the Stonecutters Bridge, Hong Kong, *LTR-AL-2003-79, CNRC, IAR*, January 2004.

Honours and Awards

- Research bursary for master's degree at University of Ottawa
- Graduate Studies Scholarship Supplement from National Research Council
- NRC Outstanding Achievement Award 2003 for contribution to Tacoma Narrows Bridge Project
- Personality 2002 in Engineering Physics, Laval University
- Athlete *Sports and Study* 98-99 at Levis-Lauzon College (soccer)
- Exceptional athlete twice for female soccer team at College Levis-Lauzon
- Personality of the year 96-97 for final grade at high school
- Outstanding achievement award for high school mathematics